

Università degli studi di Napoli Federico II



FACOLTÀ DI INGEGNERIA

Dipartimento di Ingegneria industriale

DOTTORATO DI RICERCA

IN

INGEGNERIA DEI SISTEMI MECCANICI

(XXVII CICLO)

Characterization of air/fuel mixture and combustion processes in a DISI engine through advanced optical and X-ray based diagnostics

COORDINATORE DEL DOTTORATO:

Ch.mo Prof. Ing. Fabio Bozza

Relatore

Ch.mo Prof. Ing. Fabio Bozza

Candidato

Luca Marchitto

Correlatori

Dott. Luigi Allocca

Dott.ssa Simona Silvia Merola

Dott. Ing. Gerardo Valentino

Preface

Concerns about climate change, urban air pollution and dependence on unstable and expensive supplies of foreign oil have led policy-makers and researchers to investigate alternatives and concurrently to elaborate technological solutions for the optimization of conventional petroleum-fuelled internal-combustion-engine vehicles.

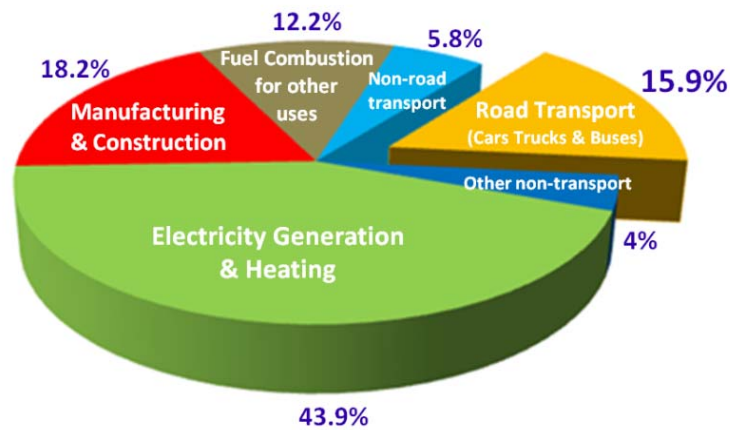


Figure 1 – CO₂ emissions from [1]

As shown in Figure 1, road transport is the second main responsible for CO₂ emissions (about 16% of man-made), after the energy production. Because vehicles that get some or all of their power from an electric drivetrain can have low or even zero emissions of greenhouse gases (GHGs) and urban air pollutants, and can consume little or no petroleum, there is considerable interest in developing and evaluating advanced electric vehicles (EVs), including pure battery-electric vehicles, plug-in hybrid electric vehicles and hydrogen fuel-cell electric vehicles. On the other hand, more work is still necessary to assess and optimise the infrastructure needed for their development. For a medium

term solution International Organization of Motor Vehicle Manufacturers has developed an integrated approach for reducing vehicles CO₂ emissions based on five key factors:

- Technology improvement for fuel consumption reduction.
- Use of alternative fuels for replacing the fossil oil
- Driver education for diffusing techniques to reduce fuel consumption [2]
- Infrastructure network improvement

Even if alternative fuels, such as alcohols for spark ignition[3-5] engines and methyl esters for compression ignition engines [6-7] , are widely used in transportation as blend or fossil fuel replacement, the most effective and immediate solution for fuel saving is the technology improvement of the engines. Specifically, for Spark-Ignition (SI) engines the Direct-Injection (DI) combined with downsizing, variable valve timing and turbocharging promises a strong reduction of fuel consumption [8-12]. The advantages of Direct-Injection over Port fuel Injection (PFI) have been widely demonstrated in terms of fuel economy, transient response, air-fuel ratio control and reduced emissions [13-17]. The DISI engines can run with high Air-to-Fuel ratio (AFR) at low load, with evident benefits for fuel consumption. On the other hand, the use of direct injection prevents the correct working of three way catalyst which requires close to stoichiometric mixture condition for efficiently operating. As a result, GDI engines provide the same critical issues of Diesel engine, concerning NO_x and PM emissions so that a specific standard regulates the exhaust emissions of GDI engines.

For this reason, the control of fuel spray and air-fuel mixture formation is fundamental for fully taking advantages of Direct Injection in SI engines.

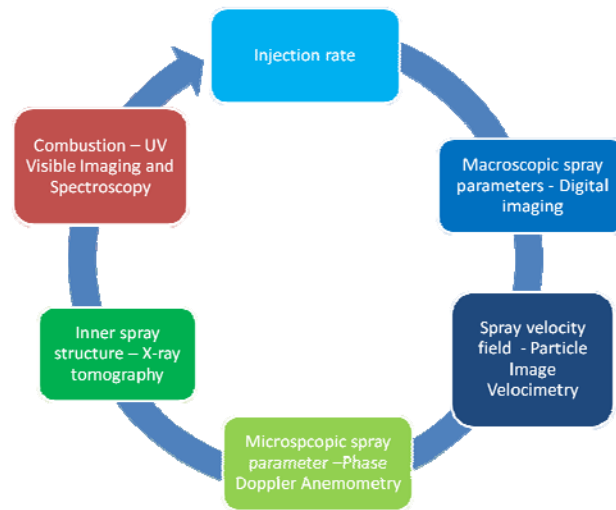


Figure 2 – Research activity flow chart

This work aims to investigate the influence of injection parameters on air/fuel mixture and combustion processes in a DISI engine, through advanced non-intrusive diagnostics. The present dissertation is the result of three years of research activities developed through a synergic and effective collaboration between the “Dipartimento di Ingegneria Industriale - Università degli studi di Napoli Federico II” (DII) under the supervision of Prof. Fabio Bozza and Istituto Motori-CNR in Naples. The work can be ideally divided in three parts (figure 2): the first, concerning the investigation of macroscopic parameters of fuel spray, the second, concerning the microscopic parameters and the latter, regarding the effect of injection timing on the engine combustion process. Firstly, the injection rate of a GDI system has been characterized with particular care to evaluate the effects of injection pressure on the fuel mass flow. The experiments have been conducted in the Spray Laboratory at Istituto Motori under

supervision of Dr. Luigi Allocca. An Injection rate meter based on the Bosch Tube method has allowed to perform time resolved measurements of the fuel mass delivered during each single injection event.

Successively, the main geometric spray characteristics have been estimated through 2D digital imaging while Particle Image Velocimetry has allowed to characterize the fuel droplets velocity field. For a deeper understanding of the break-up phenomena involving the fuel spray, Phase Doppler Anemometry technique has been applied for single point measurements of droplets size and velocity. This part of activity has been achieved under the supervision of Dr. Eng. Gerardo Valentino. Even if the PDA is the only effective technique for the direct measurement of spray droplets size, it is strongly limited in the spray region immediately downstream of the nozzle. This issue has been addressed and solved through the collaboration between Istituto Motori and X-Lab of INFN – LNF. Under the guide of Prof. Sultan Dabagov and Dr. Luigi Allocca, a desktop facility for spray X-ray tomography has been designed allowing to investigate the inner structure of the fuel spray. The technique exploits the low radiation absorption of gasoline allowing to look into the spray. After a calibration procedure, quantitative measurements of fuel mass distribution inside each single jet have been provided, in the region immediately out of the nozzle hole. The spray development analysis has been useful for setting the injection strategies characteristics of wide open throttle operative conditions for an optically accessible SI engine at different AFR.

Finally, the effect of the injection duration and phasing on the combustion process and pollutant emissions formation have been studied. Experiments have been conducted in a GDI optically accessible engine, through UV-visible imaging and spectroscopy, in the SI engine test bed facility under the supervision of Dr. Simona Silvia Merola. Both

stoichiometric and lean mixture conditions have been investigated. UV-Visible imaging has allowed to follow the overall combustion process, from the first evidence of the flame kernel until the opening of exhaust valves. Moreover, the start of injection has been changed in order to investigate the influence of the injection timing on the soot and NO_x formation. UV-visible emission spectroscopy has been applied for the detection of the chemical markers of the combustion process. Chemiluminescence signal due to OH has been detected and correlated to NO_x emission at the engine exhaust. The soot spectral feature in the visible wavelength range has been linked to soot engine out emissions.

The present work has allowed to investigate the relationships among the wall-guided fuel injection strategy, the spray development and the combustion process.

REFERENCES

- [1] International Organization of Motor Vehicle Manufacturers
<http://www.oica.net/category/climate-change-and-co2/>
- [2] <http://www.ecodrive.org/>
- [3] Merola, S. S., Valentino, G., Tornatore, C., & Marchitto, L. (2013). In-cylinder spectroscopic measurements of knocking combustion in a SI engine fuelled with butanol–gasoline blend. *Energy*, 62, 150-161. DOI 10.1016/j.energy.2013.05.056
- [4] Marchitto, L., Valentino, G., Merola, S., & Tornatore, C. (2015). Characterization of Alcohol Sprays From Multi-Hole Injector for DISI Engines Through PIV Technique (No. 2015-01-0927). SAE Technical Paper. DOI 10.4271/2015-01-0927.
- [5] Cairns, A., Zhao, H., Todd, A., & Aleiferis, P. (2013). A study of mechanical variable valve operation with gasoline–alcohol fuels in a spark ignition engine. *Fuel*, 106, 802-813. DOI 10.1016/j.fuel.2012.10.041.
- [6] Valentino, G., Allocca, L., Iannuzzi, S., & Montanaro, A. (2011). Biodiesel/mineral diesel fuel mixtures: spray evolution and engine performance and emissions characterization. *Energy*, 36(6), 3924-3932. DOI 10.1016/j.energy.2010.10.052
- [7] Hassaneen, A., Munack, A., Ruschel, Y., Schroeder, O., & Krahl, J. (2012). Fuel economy and emission characteristics of Gas-to-Liquid (GTL) and Rapeseed Methyl Ester (RME) as alternative fuels for diesel engines. *Fuel*, 97, 125-130. DOI 10.1016/j.fuel.2012.01.077
- [8] Lake, T., Stokes, J., Murphy, R., Osborne, R. et al., "Turbocharging Concepts for Downsized DI Gasoline Engines," SAE Technical Paper 2004-01-0036, 2004, DOI 10.4271/2004-01-0036.

- [9] Bandel, W., Fraidl, G., Kapus, P., Sikinger, H. et al., "The Turbocharged GDI Engine: Boosted Synergies for High Fuel Economy Plus Ultra-low Emission," SAE Technical Paper 2006-01-1266, 2006, DOI 10.4271/2006-01-1266.
- [10] Jiang, L., Vanier, J., Yilmaz, H., and Stefanopoulou, A., "Parameterization and Simulation for a Turbocharged Spark Ignition Direct Injection Engine with Variable Valve Timing," SAE Technical Paper 2009-01-0680, 2009, DOI 10.4271/2009-01-0680.
- [11] Fraser, N., Blaxill, H., Lumsden, G., and Bassett, M., "Challenges for Increased Efficiency through Gasoline Engine Downsizing," SAE Int. J. Engines 2(1): 991-1008, 2009, DOI 10.4271/2009-01-1053.
- [12] Boretti, A., "Use of Variable Valve Actuation to Control the Load in a Direct Injection, Turbocharged, Spark-Ignition Engine," SAE Technical Paper 2010-01-2225, 2010, DOI 10.4271/2010-01-2225.
- [13] Kume, T., Iwamoto, Y., Iida, K., Murakami, M. et al., "Combustion Control Technologies for Direct Injection SI Engine," SAE Technical Paper 960600, 1996, DOI 10.4271/960600.
- [14] Takagi, Y. (1998, December). A new era in spark-ignition engines featuring high-pressure direct injection. In Symposium (International) on Combustion (Vol. 27, No. 2, pp. 2055-2068). Elsevier. DOI 10.1016/S0082-0784(98)80052-0.
- [15] Zhao F., Lai M.-C., Harrington D.L. (1999) Automotive spark-ignited direct-injection gasoline engines, Progress in Energy and Combustion Science, 25(5), 437-562.

[16] Han, Z., Reitz, R., Yang, J., and Anderson, R., "Effects of Injection Timing on Air-Fuel Mixing in a Direct-Injection Spark-Ignition Engine," SAE Technical Paper 970625, 1997, DOI 10.4271/970625.

[17] Alkidas, A. C. (2007). Combustion advancements in gasoline engines. *Energy Conversion and Management*, 48(11), 2751-2761. DOI 10.1016/j.enconman.2007.07.027.

Contents

Introduction		I
Chapter 1	The air-fuel mixing in Direct Injection Spark Ignition Engines	1
1.1	The air-fuel mixing in the spark ignition engines	3
1.2	The air-fuel mixing in Direct Injection Spark Ignition Engines	6
1.2.1	Wall guided system	7
1.2.2	Air guided system	8
1.2.3	Spray guided system	9
1.3	Charge formation mechanisms at different load conditions	10
1.4	Beyond the state of art	13
	References	17
Chapter 2	Fuel spray morphology and atomization process	26
2.1	Injection fluid dynamic conditions	27
2.2	The atomization process	27
2.2.1	Primary break-up	30
2.2.2	Secondary break-up	32
2.2.3	Particle collision	33
2.3	Main spray characteristics	36
2.3.1	Liquid properties	37
2.3.2	Macroscopic parameters	38
2.3.3	Microscopic parameters	41
	References	43

Chapter 3	Fuel injection rate measurements	45
3.1	Experimental set-up	46
3.1.1	The injection system	46
3.1.2	The Bosch tube	48
3.2	Operative conditions and results	51
	References	55
Chapter 4	High Speed Visualization and Particle Image Velocimetry	57
4.1	Experimental set-up	58
4.1.1	Synchronization system	59
4.1.2	PIV system	60
4.1.2.1	CCD Camera	61
4.1.2.2	Nd:YAG Laser	62
4.2	PIV principle and methodologies	65
4.3	Operative conditions and results	72
4.3.1	High Speed Visualization	73
4.3.2	Particle Image Velocimetry	77
	References	91
Chapter 5	Phase Doppler Anemometry	94
5.1	Experimental set-up	95
5.1.1	Synchronization system	96
5.1.2	PDA System	97
5.1.2.1	Laser	98
5.1.2.2	Transmitting probe	99
5.1.2.3	Receiving probe	99
5.1.2.4	BSA Processor	101
5.1.2.5	Data acquisition software	101
5.2	PDA principle and methodologies	103
5.2.1	LDV and PDA principle	103
5.2.2	Experimental methodologies	112
5.3	Operative conditions and results	115
	References	126

Chapter 6	X-ray tomography for GDI injection characterization	128
6.1	Experimental set-up	130
6.1.1	Polycapillary lens	131
6.1.2	High pressure rotating system	133
6.2	Data acquisition and post-processing	135
6.3	Results	139
	References	144
Chapter 7	GDI engine: combustion process investigation	147
7.1	Experimental set-up	148
7.1.1	Optically accessible engine	148
7.1.2	Optical diagnostics set-up	151
7.1.3	Image acquisition and post-processing	154
7.2	Operative conditions and results	156
7.2.1	In-cylinder pressure and exhaust emission analysis	156
7.2.2	UV-Visible imaging and spectroscopy	160
	References	171
	Conclusion	179
	Acknowledgment	184

Chapter 1

Air-fuel mixing in

Direct Injection Spark Ignition

Engines

The internal combustion engine technologies for automotive applications have been continuously improved in the last years for reducing fuel consumption, in order to mitigate the effect of global warming and the risk of depleting fossil fuels [1].

However, the increasingly stringent environmental regulations impose further developments for fuel efficiency improvement and pollutant emission reduction without penalty of brake power.

An accurate control of fuel/air charge is fundamental in order to optimize the combustion process. Gasoline direct injection (GDI) for spark ignition engine plays a key role for achieving this purpose.

At first, GDI systems were introduced with the aim to improve thermal efficiency and power output [2-5]. Direct injection allows a more accurate control of the fuel injection rate with a strong reduction of combustion cycle-to-cycle variation. The high injection

pressure induces a better atomization than port fuel injection (PFI) systems with a consequent improvement of the vaporization rate.

Moreover, fuel injection directly into the combustion chamber implies a higher fuel economy and a potential reduction of unburned hydrocarbons at transient stage, especially in cold start conditions [6]. In fact with PFI, part of fuel impacts directly against the wall of the intake port and on the valves, thus a higher fuel amount is necessary for combustion. On the other hand, the reduced mixing time left to fuel and air in DI engines, induces an increase in particulate matter and unburned hydrocarbon production due to combustion chamber wall impingement.

To overcome these troubles, research and development activities on direct injection spark ignition (DISI) engines have been focused on the possibility to operate on lean combustion to provide significant fuel economy benefits over conventional port fuel injection (PFI) engines [4, 7-8].

Lean combustion with high air fuel ratio (AFR) could be achieved through stratified charge combustion in which locally rich mixture is obtained close to the spark plug and a leaner one fills the remaining combustion chamber volume. However, if the air-fuel mixture is too lean, the high amount of air dilution reduces the combustion stability, lowering the flame speed and inducing partial burning events.

It should be noted that the direct fuel injection inside the combustion chamber allows to fully take advantages of turbocharging, exhaust gas recirculation and variable controls of valves lift, achieving engine downsizing and downspeeding with a significant reduction in fuel consumption, and thus a reduction in CO₂ emissions [9-11].

1.1 Air-fuel mixing in the spark ignition engines

Spark Ignition (SI) engines can be firstly classified by fuel injection system as Port-fuel Injection (PFI) SI engines and Direct Injection SI engines (DISI). PFI is the most widespread feeding system for spark-ignition engines of passenger cars in the world. PFI differs from DI in air-fuel mixing strategy as schematically shown figure 1.1.

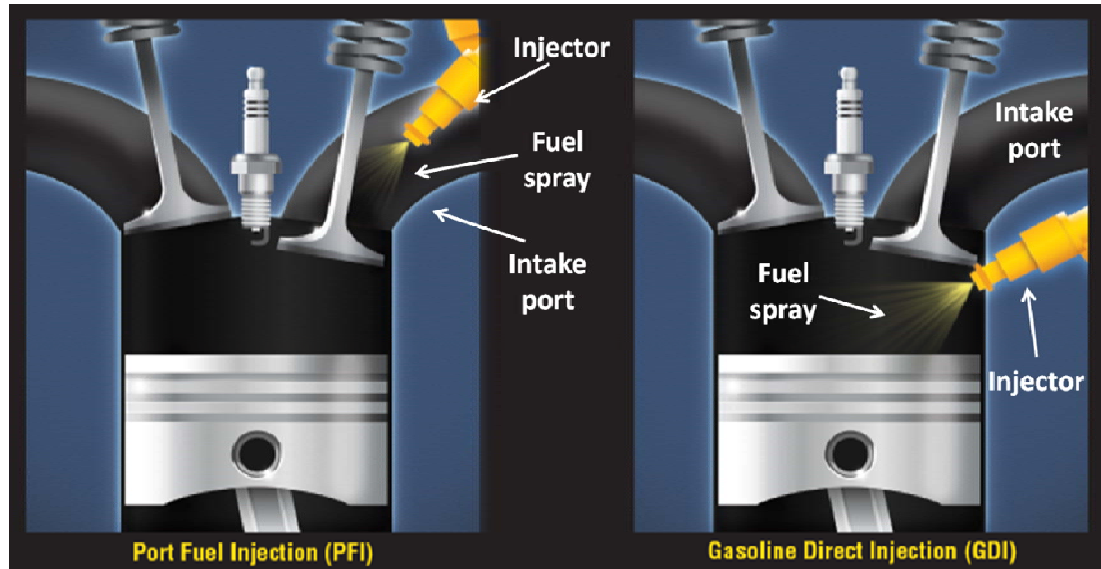


Figure 1.1 - The air-fuel mixing in the spark ignition engines [12].

The PFI system delivers fuel into the intake port of each cylinder, when the inlet valves are closed, leaving a certain time interval before the access of air-fuel mixture in the combustion chamber. The fuel is injected at low pressure (~ 0.3 MPa) on the back of the intake valves heads before their opening. As a consequence, a fuel film is deposited on the valves and in the intake manifold, delaying the fuel evaporation. This phenomenon is more significant during the cold start, requiring the injection of larger amounts of fuel than the necessary quantity for ideal stoichiometric combustion [13-14]. Moreover, some other limitations are significant for the improvement of the fuel efficiency and a solution is far to be found. The most critical issues regarding the PFI concern: the

throttle load control, providing significant pumping losses at partial load condition; the knock tendency at low speed and high load conditions, limiting the compression ratio; the necessity to always work at close to stoichiometric condition with consequent increase in CO₂ emission and fuel consumption at low load condition; the high unburned hydrocarbon (HC); the high NO_x emission at low load, due to the increase in in-cylinder temperatures for stoichiometric mixture condition.

The DISI engine represents a valid solution for overcoming most of the PFI engines limits, particularly because it allows to perform lean combustion, under highly diluted, unthrottled operation [9, 10, 15].

As first, direct injecting fuel in the combustion chamber provides a precise control of the fuel injected mass for each engine cycle, with a reduction of the cycle-to-cycle variation and removes the issues related to the fuel wall wetting in the port.

Part of the fuel deposited on the intake port of a PFI engine cannot reach the combustion chamber; as a consequence even if the injector sprays the exact amount of fuel for stoichiometric mixture, the indicating AFR results higher than the required [16-17]. As severe effect, in cold start conditions PFI engine could not fire on the first few cycles; successively the steady fuel film penetrates in the intake port gap and it induces the creation of local rich fuel regions. The interaction between the spark ignited flame front and the fuel deposits around the intake valves determines the formation of unburned HC and carbonaceous structures [14, 18-20]. Since in this operative condition the engine temperature is not high enough to activate the catalyst, high concentration of UHC are measured at the exhaust. Directly injecting the gasoline into the cylinder removes the troubles concerning fuel film in the intake port and hence drastically

reduces the cold start issues with a significant reduction in unburned HC peaks during load transients [4].

The high injection pressure of the GDI system, considerably improves the atomization, and hence the fuel vaporization rate. The mean droplets size is typically 10-15 μm [21-23], one order of magnitude lower than PFI [24-25]. On the other hand, direct injection can create fuel deposits on the piston surface; in fact, the limited time and space available for spray propagation coupled with the high injection pressure can induce the wetting of piston crowns or cylinder walls, determining wall film formation. Then, the fuel deposits evaporation is strongly related to the thermal and fluid-dynamic conditions [26-28].

Another strong limit of the PFI system is the use of throttling for load control involving a significant thermodynamic loss with a consequent reduction in thermal efficiency at low engine load. With a GDI system is theoretically possible to work unthrottled when changing the engine load [29-31].

Summarizing, gasoline direct injection systems allow to improve fuel economy because pumping and heat losses are reduced, to increase the volumetric efficiency and to work with higher compression ratios as the charge is cooled by the direct injection. Moreover GDI provides faster transient stage response, a more accurate AFR control and a reduction in HC and CO₂ emissions.

Although GDI engine provides several advantages over PFI, some issues should be addressed and completely solved [32]. Specifically, due to the limited time for air-fuel mixture formation, it is quite difficult to control the stratified charge combustion; the formation of injector deposits and/ or ignition fouling at the transient stages, the relatively high unburned HC emissions at low load; the increase in NO_x emission at

both high and partial load when stratified charge strategy is performed, locally increasing the combustion temperature peaks; increase in soot formation at high load.

In spite of several issues mainly related to the charge stratification, GDI appears as the primary technological solution for reducing fuel consumption, and hence CO₂ emission, allowing to meet stringent emission standards. Fundamental research studies represent an essential and powerful tool for a better understanding of phenomena related to the gasoline direct injection to optimize the fuel injection strategies and combustion process in SI engines.

1.2 Mixture formation in Direct Injection Spark Ignition Engines

GDI engines can be classified by the relative position of the injector with respect to the spark plug and by the mechanism which dominates the mixture formation: air-guided, wall-guided and spray-guided [4, 15, 33-34] (figure 1.2).

In air-guided and wall-guided combustion systems the injector is placed far from the spark plug, and the fuel spray is directed towards the spark plug through the in-cylinder air motion or through the interaction between spray and piston head.

In the spray-guided combustion system, the mixture formation depends on spray features and dynamics; the nozzle is close to the spark plug providing a strong coupling between fuel preparation and ignition [15].

The development of the first generation of DISI engines has been mainly focused on the wall-guided combustion system [35-36], while the second generation of DISI is oriented on the spray-guided system due to the prospective of a higher fuel economy, wider stratified combustion operation, and improved engine-out emissions [37-38].

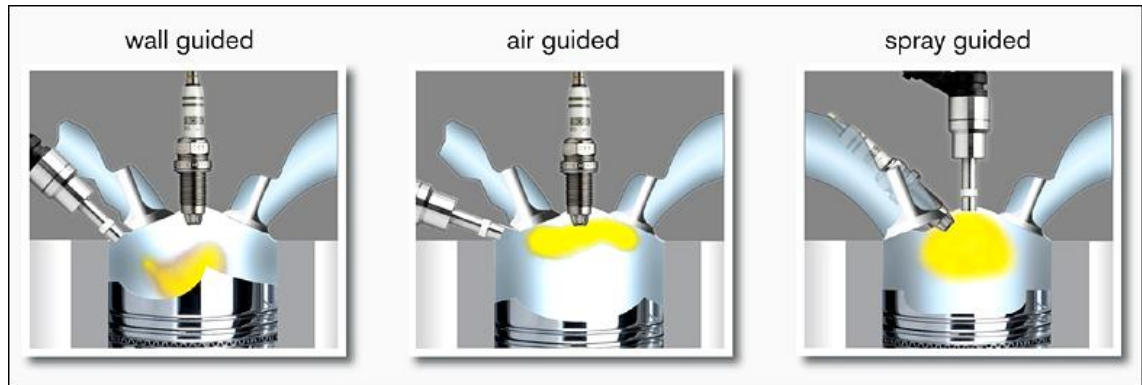


Figure 1.2 – Mixture formation modes [39].

1.2.1 Wall-guided system

The wall guided (WG) injection system is based mostly on the interaction between the fuel spray and a specially shaped surface on the piston head [35]. The spark plug is placed centrally in the combustion chamber while the injector is arranged on the side. The fuel is carried to the spark plug through the piston surface. This configuration induces an increase in unburned HC and CO emissions since the fuel is injected on the piston surface and it cannot completely evaporate [40]. The mixture formation is influenced by the swirl motion (rotational motion of charge around the cylinder axis) and the tumble motion (rotational motion in the parallel plane to the cylinder axis) [41]. Some issues related to WG GDI system are due to the difficulties in the synchronization of injection with ignition advance angle in a wide operative range of the engine. Moreover the impact of the spray on the piston surface induces the formation of liquid fuel films on the cylinder walls and piston surface, both in transient and steady operation, that cause the increment of HC and ultrafine particle at the exhaust.

1.2.2 Air-guided system

The air-guided (AG) system takes advantage of the in-cylinder flow for obtaining the air-fuel mixing [33, 42-43]. The nozzle is side mounted in the engine combustion chamber, far from the spark plug. The in-cylinder air motion is used to mix air and fuel and move the compact spray near the spark plug. Ideally, the impingement of the fuel against the piston head is prevented by the air flow, hence the unburned HC emission is reduced with respect to the wall-guided configuration. A special shape of the inlet port and piston surface are designed for inducing in-cylinder airflow and favoring the mixture motion towards the spark plug at the ignition time. However, the geometry of the combustion chamber increases the knock tendency imposing a compression ratio decrease.

A typical example of air-guided GDI system is the Volkswagen FSI (Fuel Stratified Injection) GDI Engine [44-45] (figure 1.3).

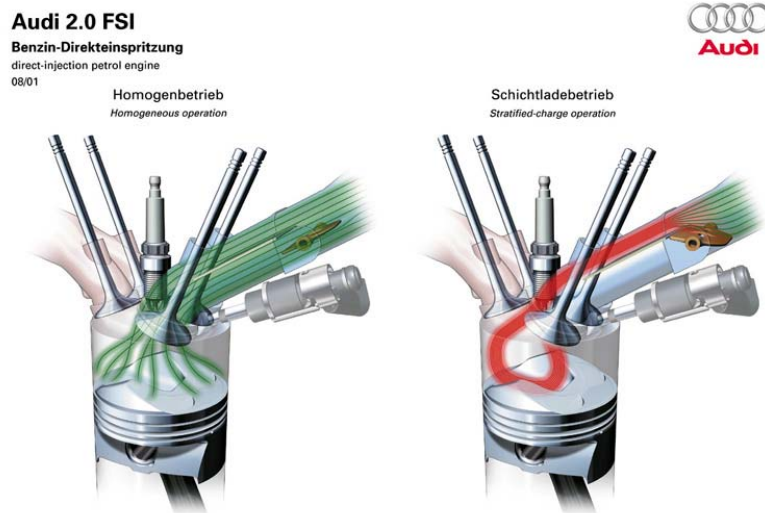


Figure 1.3 – Volkswagen FSI engine with air-wall guided combustion system [45].

The intake manifold is equipped with a flap change-over mechanism and the flow recess produces tumble air motion inside the cylinder. The tumble motion of the air is increased by the special shape of the piston crown. The piston has two bowls: one for the fuel, on the intake side, and other for the air, on the exhaust side. The fuel is guided to spark plug by the airflow and the piston shape.

1.2.3 Spray-guided system

The spray-guided (SG) system exploits the spray momentum to form directly the charge [46-47]. The injector is centrally located in the combustion chamber, while the spark plug is side placed, close to the nozzle exit (figure 1.4).



Figure 1.4 – F10 M5 spray-guided GDI combustion system.

The spray is transported to the spark plug through its kinetic energy; special shape of combustion chamber or piston and in-cylinder airflow are not necessary.

The SG GDI engines offer some specific advantages with respect to WG and AG GDI engines:

- reduced wall wetting and thus HC emissions;

- lower heat losses and pumping losses, because the fuel does not wet walls and a strong airflow is not required;
- lower sensitivity to cyclic variations of airflow;
- lower sensitivity to cylinder to cylinder variation;
- higher fuel economy.

However, there are also some disadvantages, especially concerning the reproducibility of spray profile for all operating points. In fact, the combustion process in these systems depends on the spray characteristics determined by the injection system. A small displacement of optical spray shape can cause misfiring or liquid fuel deposits on the spark plug. As a consequence, the ignition system suffers thermal shock and carbonaceous particles and soot may be produced. Moreover, the spray characteristics (shape, penetration, cone angle) are influenced by changes of in-cylinder pressure, causing troubles concerning the ignition stability at different load points [48].

1.3 Charge formation mechanisms at different load conditions

The GDI engine mainly works using two different charge formation mechanisms, depending on the load and the engine speed: the homogeneous charge operating with stoichiometric mixtures, and the stratified charge with an overall lean AFR composition at low load and up to medium speed operation [49-50]. Figure 1.5 shows the different mechanisms of mixture formation in homogeneous and stratified charge mode.

Combining these two different charge formation mechanisms it is possible to take the maximum advantage in terms of fuel-economy. Figure 1.6 shows a diagram of the optimal charge formation mechanism as function of the engine load and speed: the DISI

engine runs with a stratified charge and with lean mixtures during low load/speed operation, and runs with a “homogeneous” charge at higher load/speed points.

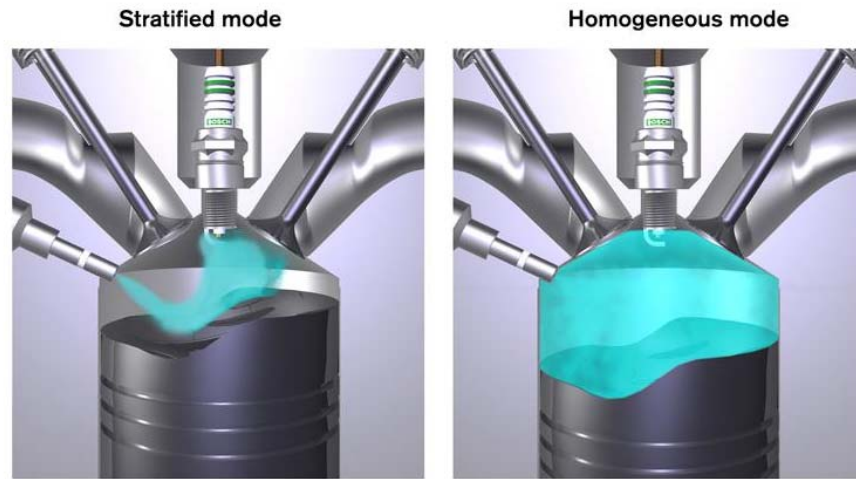


Figure 1.5 – Homogeneous and stratified charge mode [51].

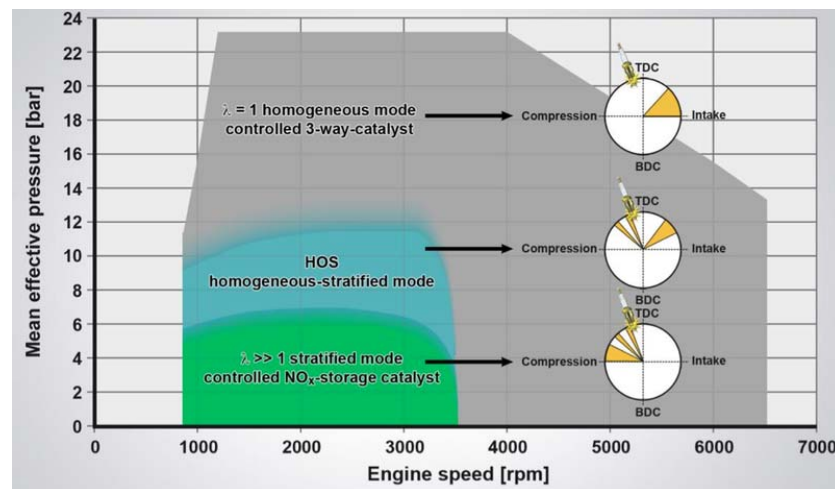


Figure 1.6 – GDI operating modes depending on load and speed [52].

In spite of the several advantages involving the use of the stratified charge at low load/speed, some issues related to the combustion stability should be further addressed. As an example, the use of spray-guided and wall guided combustion systems imposes to advance the spark timing to reach the optimal phasing [7, 53-54]. Figure 1.7 shows a

comparison of rate of heat release curves for different combustion systems. For both stratified charge systems the ignition is advanced with respect to the homogeneous condition. As consequence, the stratified charge induces an increase in the negative work, corresponding to an engine efficiency loss.

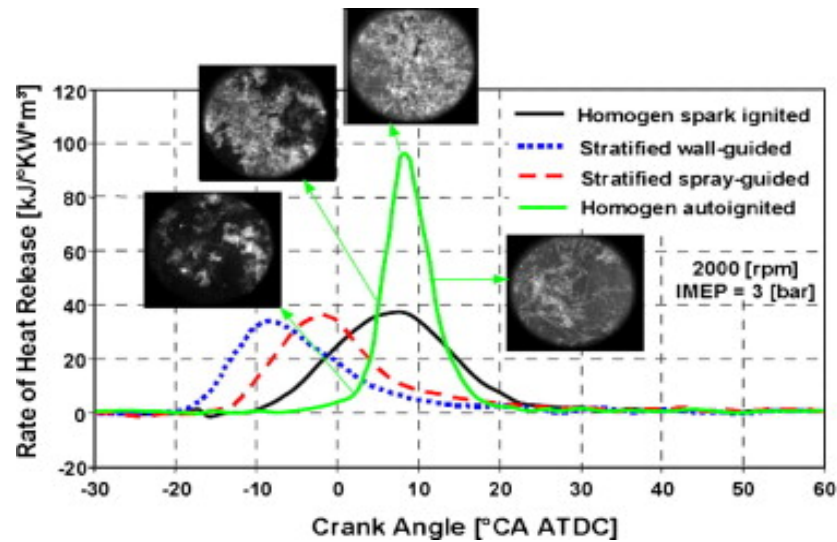


Figure 1.7 – Rate of Heat Release for stratified and homogeneous charge combustion systems [55].

On the other hand, the stratified charge allows to work with lean air-fuel mixtures, reducing the engine load without throttle valve with advantages typical of diesel engines. In fact, besides lower pumping losses, lower combustion temperatures and lower thermal exchanges are achieved, due to the high air excess. In this operative condition, exhaust gas recirculation (EGR) is necessary for keeping NO_x under acceptable values due to the air excess and the local increase in temperature [47, 56]. At high load, the overall AFR is stoichiometric, hence the stratified charge, can provide fuel rich regions that induce local diffusion flame inception and determine carbonaceous structures and ultrafine particle formation. Therefore, at high speed and full load, the engine preferably runs in homogeneous mode to obtain lower emissions and higher

torque than in stratified condition [57]. In fact, the fuel injection during the intake stroke ensures the time for the mixture formation with homogeneous charge at stoichiometric, or slightly rich, air/fuel ratio. The load control is achieved by managing the throttle valve. The NO_x emissions decrease as the engine operates with stoichiometric mixture. In this condition the main parameter conditioning the engine torque and fuel consumption is the spark advance.

When increasing the load, the engine can operate in homogeneous split mode, which involves two stage injection. A larger amount of fuel is early injected during the intake stroke in order to form a lean mixture distributed uniformly in the combustion chamber. The remaining fuel is injected during the compression stroke forming a rich zone around the spark plug [58]. Double injection allows to reduce soot formation and decrease fuel consumption in the transition area at low engine speed. When the load increases, combustion temperature becomes high and homogeneous split mode can prevent the knock [37].

1.4 Beyond the state of art

To fully exploit the distinctive features of GDI engines for the reduction of CO₂ emission and fuel consumption, several issues have to be addressed and solved for fitting the stringent anti-pollution standards (Table 1.1) with specific target on the reduction of PM and soot particle emission at the exhaust.

An additional challenge is the realization of lean engine mode with stratified charge in a wide load range, which allows to fully take advantages of the direct injection, achieving a significant reduction of fuel consumption [59]. To this aim, Mercedes-Benz has developed a new injection system based on piezo-injector technology coupled with a spray-guided combustion system [60]. The piezoelectric effect enhances the response to

nozzle opening and closing operations. The piezo-injectors are four-five times faster than conventional injectors; they can inject fuel up to ten times during a combustion cycle and allow more accurate fuel mass delivery.

Table 1.1 – Euro 5-6 spark ignition emission limits [61].

EURO 5-6 SPARK IGNITION EMISSION LIMITS

Emissions	Unit	PC M ¹⁾ , LDT N1 CL 1			
		Euro 5a	Euro 5b/b+	Euro 6b	Euro 6c
THC	mg/km	100	100	100	100
NMHC		68	68	68	68
NOx		60	60	60	60
CO		1.000	1.000	1.000	1.000
PM ²⁾³⁾		5,0	4,5	4,5 ²⁾	4,5 ²⁾
PN # ³⁾		Nb/km	-	-	6,0 * E11 ⁴⁾
Emissions	Unit	LDT N1 CL 2			
		Euro 5a	Euro 5b/b+	Euro 6b	Euro 6c
THC	mg/km	130	130	130	130
NMHC		90	90	90	90
NOx		75	75	75	75
CO		1.810	1.810	1.810	1.810
PM ²⁾³⁾		5,0	4,5	4,5	4,5
PN # ³⁾		Nb/km	-	-	6,0 * E11 ⁴⁾
Emissions	Unit	LDT N1 CL 3, N2			
		Euro 5a	Euro 5b/b+	Euro 6b	Euro 6c
THC	mg/km	160	160	160	160
NMHC		108	108	108	108
NOx		82	82	82	82
CO		2.270	2.270	2.270	2.270
PM ²⁾³⁾		5,0	4,5	4,5	4,5
PN # ³⁾		Nb/km	-	-	6,0 * E11 ⁴⁾

¹⁾ No exemption for gasoline Passenger Car

²⁾ Applicable to gasoline DI engines only

³⁾ Test procedure defined in UN Reg 83 Suppl 7

⁴⁾ Until 3 years after dates for type approval/1st registration particle emission limit of 6,0 x E12 may be applied to Euro 6 spark ignition DI vehicles upon request of manufacturer

The option of multiple injections permits to extend lean-burn operating mode to higher speed and wider load range.

Regarding carbonaceous structures and particles in the combustion chamber due to wall wetting, piezoelectric injectors reduce the phenomenon thanks to a spray with a smaller penetration depth than conventional multi-hole injectors. As in Figure 1.8, outward-opening piezo-injector nozzle (left) shows a completely de-throttled operating point if

compared with the standard multi-hole valves (right) with 20 MPa injection pressure for the piezo injector versus 13 MPa for the multi-hole valve.

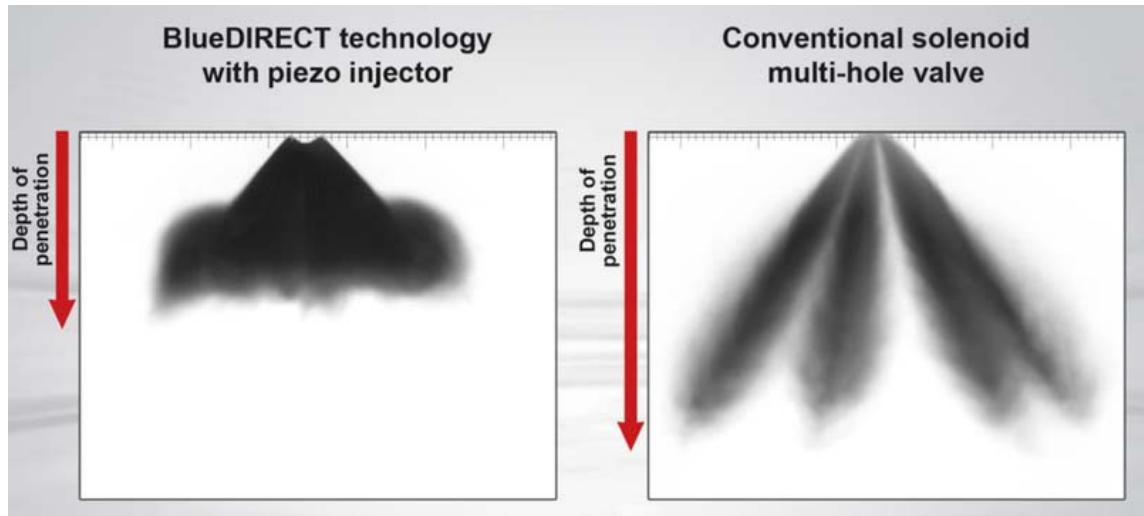


Figure 1.8 – Comparison of the spray penetration depths of Mercedes piezo-injector and multi-holes injectors [59].

Magneti Marelli considers two main injection strategies in order to control mixture formation and reduce particulate emissions [62]: multiple injections or split injection.

Multiple injections aims to reduce the wall impingement and improve the mixture homogeneity. Current Magneti Marelli systems allow to inject up to five times per cycle with high precision and low time interval between two consecutive injections.

Multiple injections take place during the intake stroke in order to obtain a more homogeneous mixture. The fuel evaporates more rapidly and thus the penetration depth in the combustion chamber is low. In this way the wall wetting is reduced and thus the soot emissions decrease.

The split injection is performed during the intake and compression stroke to locally obtain a homogeneous lean charge with a rich region only close to the spark plug through the second injection event for taking the same advantages of mixture

stratification. The aim is the improvement of the combustion stability during catalyst heating operation and the reduction of the knock tendency at high loads. The minimum injected quantity is the factor which permits to achieve the optimal injection pattern because, during the compression stroke, the injected mass can be small enough. Split or multiple injections require a more accurate and hard control of injection [62]

An important improvement in the GDI engine fuel economy is achieved using lean operation; the problem related to poor mixing are NO_x emissions. A solution should be an increase of the injection pressure, also over 400 bar [63], and apply the multiple injections strategy.

The higher fuel pressure, coupled with high turbulence levels, provides a better spray atomization and thus a reduction of the penetration depth. Moreover the increase in the injection pressure reduces the time for injecting the fuel mass with a higher time available for air-fuel mixing. The results are faster and more efficient combustion, increase in combustion stability and decrease of soot concentration. The advantages are achieved at different operating modes. In stratified condition, the charge stratification is improved; in homogeneous condition the faster evaporation and better air-fuel mixing lead to a reduction of soot concentration. In the catalyst heating phase, a late injection around spark timing in addition to higher pressure, involves an increase in combustion stability and reduces soot emissions [64].

REFERENCES

- [1] Park, C. W., Oh, H. C., Kim, S. D., Kim, H. S., Lee, S. Y., & Bae, C. S. (2014). Evaluation and visualization of stratified ultra-lean combustion characteristics in a spray-guided type gasoline direct-injection engine. *International Journal of Automotive Technology*, 15(4), 525-533. DOI 10.1007/s12239-014-0055-1.
- [2] Park, C., Kim, S., Kim, H., & Moriyoshi, Y. (2012). Stratified lean combustion characteristics of a spray-guided combustion system in a gasoline direct injection engine. *Energy*, 41(1), 401-407. DOI 10.1016/j.energy.2012.02.060.
- [3] Najjar, Y. S. (2011). Comparison of performance of a greener direct-injection stratified-charge (DISC) engine with a spark-ignition engine using a simplified model. *Energy*, 36(7), 4136-4143. DOI 10.1016/j.energy.2011.04.031.
- [4] Zhao, F., Lai, M. C., & Harrington, D. L. (1999). Automotive spark-ignited direct-injection gasoline engines. *Progress in energy and combustion science*, 25(5), 437-562. DOI 10.1016/S0360-1285(99)00004-0.
- [5] Marchitto, L., Hampai, D., Dabagov, S. B., Allocca, L., Alfuso, S., Polese, C., & Liedl, A. (2015). GDI spray structure analysis by polycapillary X-ray μ -tomography. *International Journal of Multiphase Flow*, 70, 15-21. DOI 10.1016/j.ijmultiphaseflow.2014.11.015.
- [6] Peckham, M. S., Finch, A., & Campbell, B. (2011). Analysis of transient HC, CO, NO_x and CO₂ emissions from a GDI engine using fast response gas analyzers (No. 2011-01-1227). SAE Technical Paper. DOI 10.4271/2011-01-1227.
- [7] Alkidas, A. and El Tahry, S. (2003). Contributors to the Fuel Economy Advantage of DISI Engines Over PFI Engines. SAE Technical Paper 2003-01-3101. DOI 10.4271/2003-01-3101.

- [8] Chitsaz, I., Saidi, M. H., Mozafari, A. A., & Hajjalimohammadi, A. (2013). Experimental and numerical investigation on the jet characteristics of spark ignition direct injection gaseous injector. *Applied Energy*, 105, 8-16. DOI 10.1016/j.apenergy.2012.11.023.
- [9] Leduc, P., Dubar, B., Ranini, A., & Monnier, G. (2003). Downsizing of gasoline engine: an efficient way to reduce CO₂ emissions. *Oil & gas science and technology*, 58(1), 115-127. DOI 10.2516/ogst:2003008.
- [10] Lecointe, B., & Monnier, G. (2003). Downsizing a gasoline engine using turbocharging with direct injection (No. 2003-01-0542). SAE Technical Paper. DOI 10.4271/2003-01-0542.
- [11] Lemazurier, L., Shidore, N., Kim, N., Moawad, A., Rousseau, A., Bonkoski, P., & Delhom, J. (2015). Impact of advanced engine and powertrain technologies on engine operation and fuel economy for future vehicles (No. 2015-01-0978). SAE Technical Paper. DOI 10.4271/2015-01-0978.
- [12] <https://www.bgprod.com/blog/gdi-stands-for-opportunity/>
- [13] Hentschel, W. (2000). Optical diagnostics for combustion process development of direct-injection gasoline engines. *Proceedings of the combustion institute*, 28(1), 1119-1135. DOI 10.1016/S0082-0784(00)80322-7.
- [14] Merola, S. S., Sementa, P., Tornatore, C., & Vaglieco, B. M. (2008). Effect of injection phasing on valves and chamber fuel deposition burning in a PFI boosted spark-ignition engine (No. 2008-01-0428). SAE Technical Paper. DOI 10.4271/2008-01-0428
- [15] Alkidas, A. C. (2007). Combustion advancements in gasoline engines. *En. Convers. and Manag.*, 48(11), 2751-2761. DOI 10.1016/j.enconman.2007.07.027.

- [16] Zhao, F. Q., Lai, M. C., & Harrington, D. L. (1995). The spray characteristics of automotive port fuel injection-a critical reviews (No. 950506). SAE Technical Paper. DOI 10.4271/950506.
- [17] Kim, H., Yoon, S., Xie, X. B., Lai, M. C., Quelhas, S., Boyd, R., & Moran, C. (2005). Effects of injection timings and intake port flow control on the in-cylinder wetted fuel footprints during PFI engine startup process (No. 2005-01-2082). SAE Technical Paper. DOI 10.4271/2005-01-2082.
- [18] Yang, J., Kaiser, E. W., Siegl, W. O., & Anderson, R. W. (1993). Effects of port-injection timing and fuel droplet size on total and speciated exhaust hydrocarbon emissions (No. 930711). SAE Technical Paper. DOI 10.4271/930711.
- [19] Witze, P. O., & Green, R. M. (1997). LIF and flame-emission imaging of liquid fuel films and pool fires in an SI engine during a simulated cold start (No. 970866). SAE Technical Paper. DOI 10.4271/970866.
- [20] Curtis, E. W., Aquino, C. F., Trumpy, D. K., & Davis, G. C. (1996). A new port and cylinder wall wetting model to predict transient air/fuel excursions in a port fuel injected engine (No. 961186). SAE Technical Paper. DOI 10.4271/961186.
- [21] Marchitto, L., Merola, S., Tornatore, C., & Valentino, G. (2014). Experimental Study on the Spray Atomization of a Multi-hole Injector for Spark Ignition Engines Fuelled by Gasoline and n-Butanol (No. 2014-01-2743). SAE Technical Paper. DOI 10.4271/2014-01-2743.
- [22] Wigley, G., Goodwin, M., Pitcher, G., & Blondel, D. (2004). Imaging and PDA analysis of a GDI spray in the near-nozzle region. *Experiments in fluids*, 36(4), 565-574. DOI 10.1007/s00348-003-0690-1.

- [23] Park, S., Cho, H., Yoon, I., & Min, K. (2002). Measurement of droplet size distribution of gasoline direct injection spray by droplet generator and planar image technique. *Measurement Science and Technology*, 13(6), 859. DOI 10.1088/0957-0233/13/6/305.
- [24] Panão, M. R., & Moreira, A. L. N. (2005). Flow characteristics of spray impingement in PFI injection systems. *Experiments in Fluids*, 39(2), 364-374. DOI 10.1007/s00348-005-0996-2.
- [25] Esmail, M., Kawahara, N., Tomita, E., & Sumida, M. (2010). Direct microscopic image and measurement of the atomization process of a port fuel injector. *Measurement Science and Technology*, 21(7), 075403. DOI 10.1088/0957-0233/21/7/075403.
- [26] Karlsson, R. B., & Heywood, J. B. (2001). Piston fuel film observations in an optical access GDI engine (No. 2001-01-2022). SAE Technical Paper. DOI 10.4271/2001-01-2022
- [27] Li, J., Huang, Y., Alger, T. F., Matthews, R. D., Hall, M. J., Stanglmaier, R. H., ... & Anderson, R. W. (2001). Liquid fuel impingement on in-cylinder surfaces as a source of hydrocarbon emissions from direct injection gasoline engines. *Journal of engineering for gas turbines and power*, 123(3), 659-668. DOI 10.1115/1.1370398.
- [28] Montanaro, A., Malaguti, S., & Alfuso, S. (2012). Wall impingement process of a multi-hole GDI spray: Experimental and numerical investigation (No. 2012-01-1266). SAE Technical Paper. DOI 10.4271/2012-01-1266.
- [29] Stansfield, P. A., Wigley, G., Garner, C. P., Patel, R., Ladommatos, N., Pitcher, G., & Helie, J. (2007). Unthrottled engine operation using variable valve actuation: the impact on the flow field, mixing and combustion (No. 2007-01-1414). SAE Technical Paper. DOI 10.4271/2007-01-1414.

- [30] Cairns, A., Todd, A., Hoffman, H., Aleiferis, P., & Malcolm, J. (2009). Combining unthrottled operation with internal EGR under port and central direct fuel injection conditions in a single cylinder SI engine (No. 2009-01-1835). SAE Technical Paper. DOI 10.4271/2009-01-1835.
- [31] Moore, W., Foster, M., Lai, M. C., Xie, X. B., Zheng, Y., & Matsumoto, A. (2011). Charge motion benefits of valve deactivation to reduce fuel consumption and emissions in a GDi, VVA engine (No. 2011-01-1221). SAE Technical Paper. DOI 10.4271/2011-01-1221.
- [32] Pontoppidan, M., Gaviani, G., Bella, G., & Demaio, A. (2002). Study of the Benefits and Drawbacks of a Substantial Increase of Rail-Pressure in GDI-Injector Assemblies (No. 2002-01-1132). SAE Technical Paper. DOI 10.4271/2002-01-1132.
- [33] Ortmann, R., Arndt, S., Raimann, J., Grzeszik, R., & Würfel, G. (2001). Methods and analysis of fuel injection, mixture preparation and charge stratification in different direct injected SI engines (No. 2001-01-0970). SAE Technical Paper. DOI 10.4271/2001-01-0970.
- [34] Hentschel, W. (2000). Optical diagnostics for combustion process development of direct-injection gasoline engines. *Proceedings of the combustion institute*, 28(1), 1119-1135. DOI 10.1016/S0082-0784(00)80322-7.
- [35] Kawajiri, K., Yonezawa, T., Ohuchi, H., Sumida, M., & Katashiba, H. (2002). Study of interaction between spray and air motion, and spray wall impingement (No. 2002-01-0836). SAE Technical Paper. DOI 10.4271/2002-01-0836.
- [36] Solomon, A. S., Anderson, R. W., Najt, P. M., & Zhao, F. (2000). *Direct fuel injection for gasoline engines*. Warrendale, PA: Society of Automotive Engineers, 2000. 468.

- [37] Schwarz, C., Schünemann, E., Durst, B., Fischer, J., & Witt, A. (2006). Potentials of the spray-guided BMW DI combustion system (No. 2006-01-1265). SAE Technical Paper. DOI 10.4271/2006-01-1265.
- [38] Peterson, B., Reuss, D. L., & Sick, V. (2014). On the ignition and flame development in a spray-guided direct-injection spark-ignition engine. *Combustion and Flame*, 161(1), 240-255. DOI 10.1016/j.combustflame.2013.08.019.
- [39] Leonhard R. Bosch DI-Motronic Gasoline Direct Injection. The technology of direct injection. http://www.autospeed.com/cms/A_1761/article.html.
- [40] Kashdan, J. T., Mendez, S., & Bruneaux, G. (2007). On the origin of unburned hydrocarbon emissions in a wall guided, low NOx diesel combustion system (No. 2007-01-1836). SAE Technical Paper. DOI 10.4271/2007-01-1836.
- [41] Kubach, H., Gindele, J., & Spicher, U. (2001). Investigations of mixture formation and combustion in gasoline direct injection engines (No. 2001-01-3647). SAE Technical Paper. DOI 10.4271/2001-01-3647.
- [42] Preussner, C., Döring, C., Fehler, S., & Kampmann, S. (1998). GDI: interaction between mixture preparation, combustion system and injector performance (No. 980498). SAE Technical Paper. DOI 10.4271/980498.
- [43] Fu, L., Ishima, T., Long, W. Q., & Tian, J. P. (2009). Research on the Ignition-Chamber GDI Engine Combustion System. *Journal of Thermal Science and Technology*, 4(1), 53-62. DOI <http://dx.doi.org/10.1299/jtst.4.53>.
- [44] Baretzky, U., Andor, T., Diel, H., & Ullrich, W. (2002). The direct injection system of the 2001 audi turbo V8 le mans engines (No. 2002-01-3357). SAE Technical Paper. DOI 10.4271/2002-01-3357.

- [45] Anon, V. A. (2002). Bosch Motronic MED7 Gasoline Direct Injection. Volkswagen Self-Study Program, 253.
- [46] Kim, S. J., Kim, Y. N., & Lee, J. H. (2008). Analysis of the in-cylinder flow, mixture formation and combustion processes in a spray-guided GDI engine (No. 2008-01-0142). SAE Technical Paper. DOI 10.4271/2008-01-0142.
- [47] Baecker, H., Kaufmann, A., & Tichy, M. (2007). Experimental and simulative investigation on stratification potential of spray-guided GDI combustion systems (No. 2007-01-1407). SAE Technical Paper. DOI 10.4271/2007-01-1407.
- [48] Baumgarten, C. (2006). Mixture formation in internal combustion engines. Springer Science & Business Media. DOI 10.1007/3-540-30836-9.
- [49] Duclos, J. M., & Zolver, M. (1998, July). 3D modeling of intake, injection and combustion in a DI-SI engine under homogeneous and stratified operating conditions. In COMODIA (Vol. 98, pp. 335-340).
- [50] Gold, M., Stokes, J., Morgan, R., Heikal, M., De Sercey, G., & Begg, S. (2001). Air-fuel mixing in a homogeneous charge DI gasoline engine (No. 2001-01-0968). SAE Technical Paper. DOI 10.4271/2001-01-0968.
- [51] <http://www.autospeed.com/cms/article.html?&A=107830>
- [52] <http://www.greencarcongress.com/2014/02/20140207-mb.html>
- [53] Harada, J., Tomita, T., Mizuno, H., Mashiki, Z., & Ito, Y. (1997). Development of direct injection gasoline engine (No. 970540). SAE Technical Paper. DOI 10.4271/970540.
- [54] Wirth, M., Piock, W. F., Fraidl, G. K., Schoeggl, P., & Winklhofer, E. (1998). Gasoline DI engines: the complete system approach by interaction of advanced development tools (No. 980492). SAE Technical Paper. DOI 10.4271/980492.

- [55] Fuerhapter, A., Piock, W. F., & Fraidl, G. K. (2003). CSI-controlled auto ignition- the best solution for the fuel consumption-versus emission trade-Off? (No. 2003-01-0754). SAE Technical Paper. DOI 10.4271/2003-01-0754.
- [56] Reitz, R. D. (2013). Directions in internal combustion engine research. *Combustion and Flame*, 160(1), 1-8. DOI 10.1016/j.combustflame.2012.11.002.
- [57] Küssel, M., Moser, W., & Philipp, M. (1999). Motronic MED7 for gasoline direct injection engines: engine management system and calibration procedures (No. 1999-01-1284). SAE Technical Paper. DOI 10.4271/1999-01-1284.
- [58] Ehlers G, Pfalzgraf B, Wurms R (2003). Homogeneous Split - a Highly Efficient Strategy to Reduce the Exhaust Emissions of FSI Engines. 9th Symposium The Working Process of the Internal Combustion Engine, Institute for Internal Combustion Engines and Thermodynamics, Graz University of Technology, Austria.
- [59] Altenschmidt F., Laudenbach N., Reck T., Schaupp U., Waltner A., Wunsch R. (2013). BlueDIRECT – The Future of SI Engines at Mercedes-Benz; Strasbourg SIA congress 2013.
- [60] Wang, C., Xu, H., Herreros, J. M., Wang, J., & Cracknell, R. (2014). Impact of fuel and injection system on particle emissions from a GDI engine. *Applied Energy*, 132, 178-191. DOI 10.1016/j.apenergy.2014.06.012.
- [61] http://www.delphi.com/manufacturers/auto/powertrain/emissions_standards
- [62] Bonandrini G., R. Di Gioia, A. Musi, D. Papaleo, M. Picerno, L. Venturoli, (2013). Numerical and experimental methodology for the definition of GDI engines injection strategies towards future emission legislation. International Conference: The Spark Ignition Engine of the Future Strasbourg - Pole Formation / CCI de Strasbourg, December 4 & 5, 2013.

- [63] Buri, S., Kubach, H., & Spicher, U. (2010). Effects of increased injection pressures of up to 1000 bar—opportunities in stratified operation in a direct-injection spark-ignition engine. *International Journal of Engine Research*, 11(6), 473-484. DOI 10.1243/14680874JER608.
- [64] H. Kubach, H. Schumann, F. Buri S. Spicher U. (2013). Potential of High Pressure Direct Injection in Gasoline Engines, Strasbourg SIA congress 2013.

Chapter 2

Fuel spray morphology and atomization process

A spray is a cloud of dispersed liquid droplets, more or less dense, mechanically produced, with a sufficient momentum to penetrate into the surrounding gaseous medium.

Sprays are used in a wide range of applications, such as meteorology, agriculture, medicine, industrial field etc.

The present study is focused on the analysis of high pressure, high density fuel spray for automotive application. The spray atomization and evaporation play an important role in the air–fuel mixing process, and therefore on the combustion development, especially for Direct Injection Spark Ignition (DISI) engines; in fact, it is possible to improve the combustion efficiency by optimizing the mixture formation, resulting in a reduction of fuel consumption and exhaust emissions, and optimizing the mixture formation.

The development of fuel spray is influenced by several phenomena, due to the interaction between injected fuel and surrounding gas. The main factors affecting the spray behaviour are:

- Injection fluid dynamic conditions, mainly the turbulence and cavitation levels within the fluid, as well as the size distribution of injected droplets;
- First and second break-up of liquid jet;
- Collision and coalescence among the drops.

2.1 Injection fluid dynamic conditions

The fluid outflow velocity immediately downstream the nozzle and the flow turbulence level within the nozzle are the main fluid dynamic characteristics influencing the dispersions modes of liquid jet.

Inside the nozzle there is a two-phase flow; the presence of cavitation can considerably increase the injection velocity [1] because the steam bubbles reduce the effective outflow section for the liquid. Furthermore, their successive implosion increase the spray instability, enhancing the break-up processes.

Considering the multi-hole atomizers, it is important to characterize the fuel flow for any single hole. In fact, several studies [2] have demonstrated that upstream conditions for each hole vary with the effective geometry of the nozzle and with its dynamic control.

The control and the knowledge of the ideal conditions for the spray production are very important for improving the combustion control and for increasing the engine performance with regard to torque and power, fuel economy and pollutant emissions.

2.2 The atomization process

The atomization process, or break-up, is the phenomenon occurring when a liquid jet or a sheet is separated into small drops. This process is governed by the interaction

between surface tension and aerodynamic forces, which are induced by the relative motion jet-gas and drops-gas [3].

Break-up occurs when the magnitude of aerodynamics forces exceeds the surface tension force [4].

The jet disintegration phenomenon has been objective of theoretical and experimental investigations for more than 100 years.

Rayleigh studied the atomization dynamics, without considering the effect of jet viscosity, surrounding air density and gravity force. A more general theory was developed by Weber, taking into account liquid viscosity and gas density effects in the mathematical analysis. He supposed a stabilizing effect of jet viscosity and gas density that leads to a reduction of break-up area and an increase of drops size.

The most supported theory considers that the joint effect of cohesive and disruptive forces on the jet surface induces oscillations on the edge. These perturbations, amplified by the aerodynamic forces, influence the atomization process [5].

The jet disintegrates in liquid ligaments and drops when the wavelength of the initial disturbance is greater than a critic value. This process is called primary atomization (or primary break-up); a scheme of this phenomenon is shown in Figure 2.1.

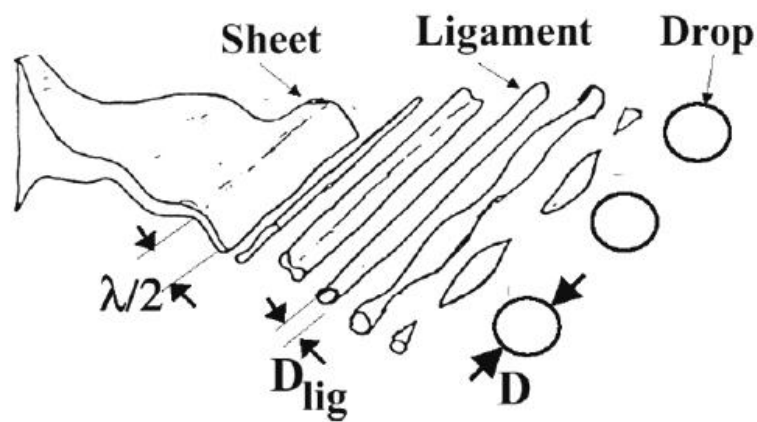


Figure 2.1 – Primary atomization [5].

The drops formed after the primary break-up are target of the combined action of inertia, viscosity, surface tension and aerodynamic forces; these forces cause non uniform pressure distribution on drops surface, inducing the drop deformation and its breakup in smaller drops (secondary atomization).

Dimensionless numbers, characterizing the atomization, are obtained as a function of the forces dominating the physical process. These are the Reynolds number (2.1) and the Weber number (2.2):

$$Re = \frac{u \cdot d}{\nu} \quad (2.1)$$

$$We = \frac{\rho_l \cdot u^2 \cdot d}{\sigma} \quad (2.2)$$

Where u is relative velocity, ν is cinematic viscosity, d is drop diameter, ρ_l and σ are density and surface tension of drop, respectively. The Weber number represents the ratio between disruptive aerodynamic forces and restoring surface tension force that has a coalescent effect and quantifies the relative importance of these two types of forces. It is often used to classify the secondary atomization processes.

The dimensionless Ohnesorge number (2.3) is obtained combining Reynolds and Weber numbers:

$$Oh = \frac{\nu_l}{(\rho_l \cdot \sigma \cdot d)^{0.5}} = \frac{\sqrt{We}}{Re} \quad (2.3)$$

This group contains only the properties of the drops formed in primary atomization before they split up into smaller drops during secondary atomization. It provides an indication of the drop resistance to further disintegration and take into accounts the effect of liquid viscosity on the drops.

2.2.1 Primary break-up

Depending on the causes generating the primary break-up, different atomization regimes can be distinguished:

- Aerodynamic-induced break-up: the atomization occurs when aerodynamic forces are greater than surface tension forces, which tend instead to avoid the break-up.
- Turbulence-induced break-up: it occurs when fully developed turbulent conditions are reached in the nozzle; the initial surface oscillations are caused by the turbulent fluctuations within the liquid at the nozzle exit.
- Cavitation-induced break-up: the cavitation babbles tend to explode, because the pressure surrounding the jet is higher than inner pressure of babbles; this causes intense perturbations into the spray and then its disintegration.

These three phenomena are generally present at the same time, with different intensity depending on the different nozzle layout and operative condition, and determine the spray structure.

In the primary break-up it is possible to individuate four regimes, depending on different combinations of inertial forces in liquid jet, surface tension, viscous and aerodynamic forces (Figure 2.2):

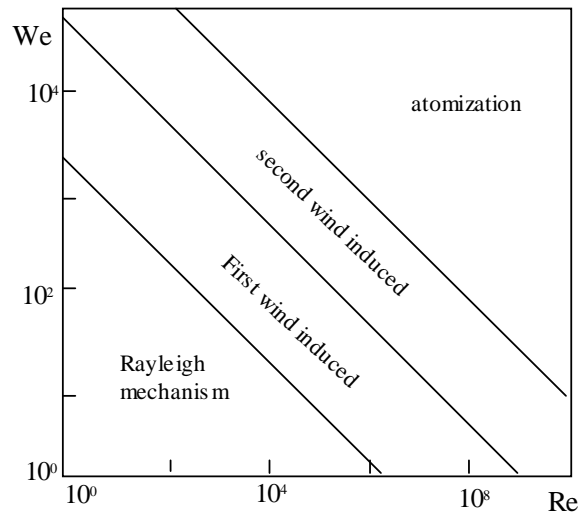


Figure 2.2 – Modes of jet break-up [6].

1. Rayleigh jet break-up. At low Reynolds values, the liquid jet velocity is low and the aerodynamic forces are negligible. The atomization is caused by the growth of axial-symmetric surface oscillations; the break-up occurs when the perturbation wavelength is greater than the jet diameter. The drop diameter is greater than jet diameter at the nozzle exit. Surface tension forces are weak, the break-up is slow and occurs away from the nozzle.
2. First wind-induced break-up. The relative velocity between jet and surrounding gas and the surface tension increase, accelerating the atomization process. Drop diameter is about the same as the jet diameter at the nozzle exit.
3. Second wind-induced break-up. Increasing Reynolds number and Weber number, the growth of short wavelength surface waves becomes unstable; drop diameter is less than jet diameter at the nozzle exit.
4. Atomization. The break-up occurs downstream of the nozzle and involves the complete jet disintegration. Drop diameter is a magnitude lower than jet diameter at the nozzle exit.

2.2.2 Secondary break-up

The secondary break-up is a more complicated phenomenon, if compared with primary break-up, and depends on the balance between surface tension, inertial and viscous forces. Experimental analysis has shown that for Weber numbers greater than one, the drops surface deforms; furthermore, if the Weber number exceeds a critic value (12 for liquid fuels), this deformation causes drop crushing. It is possible to individuate four atomization basic modes as function of the Weber number:

- Vibrational regime ($12 < We < 16$): under the action of aerodynamics pressure, the drop distorts from its spherical shape and becomes disk shaped. The external film disintegrates into a multitude of small droplets, while the liquid core breaks in larger drops.
- Bag break-up regime ($16 < We < 45$): this phenomenon occurs for relatively low values of air velocity; the drop becomes flatten and presents a concave surface near its pole. Under the action of aerodynamic pressure, small holes appear on the bag sheet and filaments form among these holes. After the break-up, the filaments produce fine drops, while the bag disintegrates in larger drops in a short time (Figure 2.3).

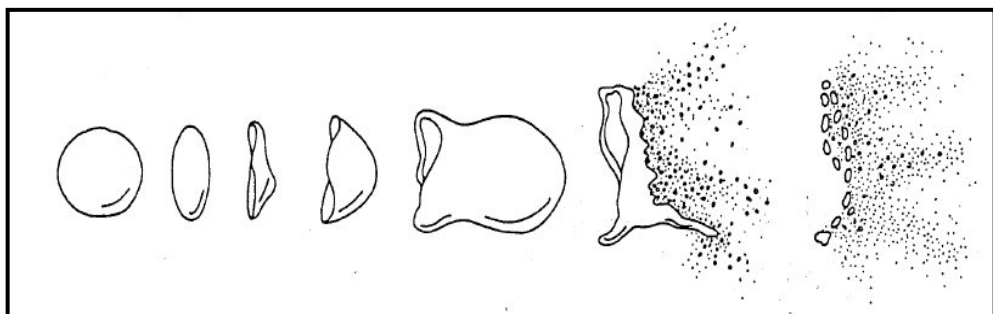


Figure 2.3 – Bag breakup regime.

- Stripping break-up regime ($100 < We < 1000$): the drops deform in the opposite direction and present a convex surface in the direction of the air flow. The drops edges split-up into fine filaments which, later, break up into small drops. The break-up occurs when the drop deformation reaches a critical value (Figure 2.4).
- Catastrophic break-up regime ($We > 1000$): when the Weber number increases, this break-up regime occurs. At high relative velocity, the forces generated by the surface tension play a dominant role in the drop deformation and disintegration process; they lead to a formation of unstable waves on drop surface. These surface waves, due to their unstable growth, tear the flattened drops into large fragments, which undergo additional breakup [7] (Figure 2.5).

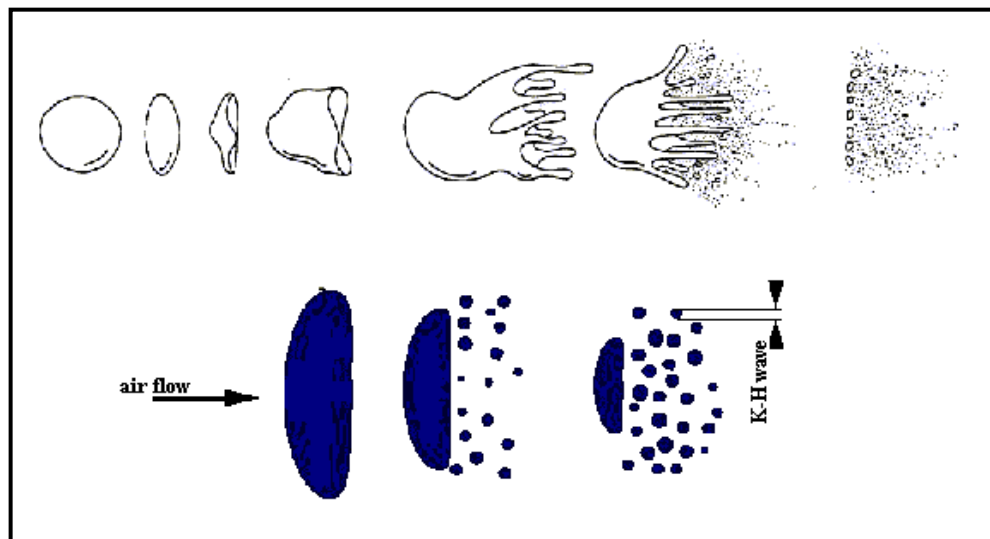


Figure 2.4 – Stripping breakup regime.

2.2.3 Particles collision

The collision is principally caused by different velocities of single drops, resulting from:

- Interaction between drops of different flows. This situation is observed in the impact zone, where the drops of the main spray meet the post-impingement ones, which move in the opposite direction.

- Different interaction with medium kinetic field of drops of various size. The bigger drops (blobs) have a highest inertia resulting in a reduced slowing down by aerodynamic forces; therefore, they can collide with smaller drops earlier injected at the same injection event. Furthermore, the blobs injected later, are subjected to a wake effect because their interaction with the medium is reduced by the previous drops.

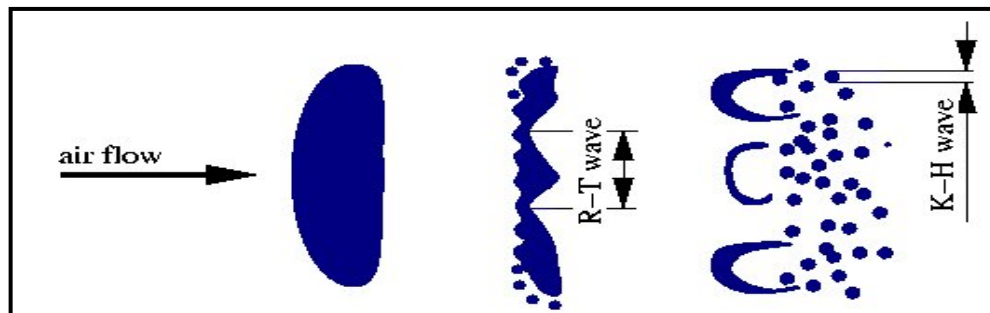


Figure 2.5 - Catastrophic breakup regime

- Different velocities in the injection interval. These phenomena can occur, especially when the injection event is prolonged and the injection pressures are high, due to propagation of pressure waves into the ducts.

Experimental observations highlighted that different types of collision are obtained, depending on inertial properties, fluids characteristics and relative motion between particles:

1. Bouncing collision: the drops bounce away from each other (Figure 2.6).
2. Grazing collision: the drops bounce but the contact between the surfaces is prevented by the presence of steam film.
3. Permanent coalescent. The drops coalesce and remain permanently joined (Figure 2.7).

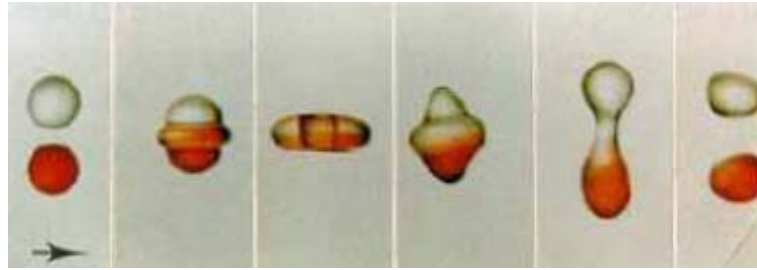


Figure 2.6 – Bouncing collision.

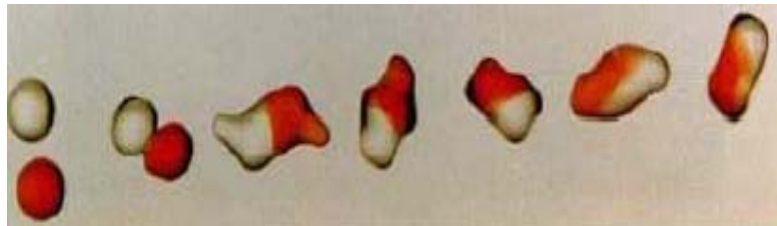


Figure 2.7 – Permanent coalescent.

4. Shattering collision. When the impact energy is high, from the edges of interacting drops are radially ejected smaller drops (Figure 2.8).

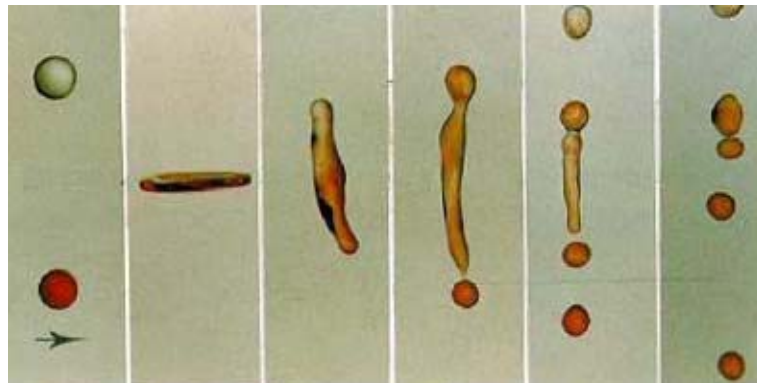


Figure 2.8 – Shattering collision.

The type of collision depends on size, velocity and angular momentum of the drops and physical characteristics of the liquid and the medium.

2.3 Main spray characteristics

Liquid velocity varies in the different point of jet section and in the successive injection instants, as well as the motion conditions of the drops and the air within the combustion chamber. This implies an unequal spatial atomization of the jet with a formation of drops whose diameter can varies in a wide range during the injection event. To define the atomization level is necessary to use statistical indices, as the mean diameter of drops, and a specific distribution function of their sizes. These parameters can be derived by the trend, experimentally obtained, of probability density function $f(x)$, where the variable x is the drop diameter [8]. The most interesting formulas for the mean diameters are:

- *Surface mean diameter (d_s):* it is defined as the diameter of a drop whose surface, if multiplied by the number of drops, equals the total surface of the sample.

$$d_s = \sqrt{\int_{X_m}^{X_M} x^2 \cdot f(x) dx} \quad (2.4)$$

where X_m is the minimum diameter observed and X_M is the maximum diameter observed.

- *Volume mean diameter (d_{vol}):* it is defined as the diameter of a drop whose volume, if multiplied by the number of drops, equals the total volume of the sample.

$$d_{vol} = \sqrt[3]{\int_{X_m}^{X_M} x^3 \cdot f(x) dx} \quad (2.5)$$

- *Sauter Mean Diameter (SMD):* it is defined as the diameter of the drop whose ratio of volume to surface is the same as that of the entire spray.

$$SMD = \frac{\int_{x_m}^{x_M} x^3 \cdot f(x) dx}{\int_{x_m}^{x_M} x^2 \cdot f(x) dx} \quad (2.6)$$

The Sauter mean diameter is the most used statistical index; in fact, the evaporation rate of liquid fuel determines the combustion rate and it is proportional to the heat flow between drop and surrounding gas, and thus to surface/volume ratio.

Atomization process is a function of the following parameters:

- Injection pressure, whose increase leads to an increment in drop velocities and, consequently, in an increase of the aerodynamic force intensities;
- Surface tension and fuel viscosity; an increase in the last causes an opposite effect to injection pressure;
- Geometrical characteristics of the injector;
- Thermo-fluid dynamic conditions within the combustion chamber, in terms of density, temperature and turbulence intensity, which have a significant effect on air-fuel interaction.

2.3.1 Liquid properties

The flow and spray characteristics of most atomizers are influenced by the liquid properties such as density, viscosity and surface tension.

The importance of density for atomization performance is reduced by the fact that most liquids exhibit only minor differences in this property.

Surface tension, instead, is important in atomization because it represents the force that resists the formation of new surface area. The minimum energy required for atomization is equal to the surface tension multiplied by the increase in liquid surface area.

Whenever atomization occurs under conditions where surface tension forces are important, the Weber number is a useful parameter for correlating drop size data.

In general, the viscosity is the most effective liquid property on the spray development. In fact, it affects not only the drop size distribution in the spray but also the nozzle flow rate and spray pattern. An increase in viscosity lowers the Reynolds number and prevents the development of any natural instability in the jet. The combined effect of these phenomena delays the disintegration and increases the drops size in the spray.

The viscosity of liquids generally decreases by increasing the temperature. The heavier fuel oils are often heat up, both to reduce the pumping power and improve the atomization [4].

2.3.2 Macroscopic parameters

A fuel jet is characterized by its macroscopic geometrical parameters: penetration and diffusion.

The spray penetration is defined as the maximum distance it reaches when injected into stagnant air [4]. It is governed by the relative magnitudes of two opposite forces: kinetic energy of the initial liquid jet and aerodynamic resistance of the surrounding gas.

The initial jet velocity is usually high but, as atomization proceeds and the spray surface area increases, the liquid kinetic energy is gradually dissipated in frictional losses with the gas. When the drops have exhausted their kinetic energy, their trajectory is mainly due to the gravity and the surrounding gas motion.

The following formula (2.7) can be used to establish the parameters that influence the penetration:

$$u = u_o \cdot e^{-\left(\frac{k \cdot \rho_a}{d_d \cdot \rho_l}\right) \cdot s} \quad (2.7)$$

where s is the penetration length, u is the instantaneous velocity of the single drop, as function of the initial velocity u_0 .

Therefore, the penetration increases if:

- the air density ρ_a decreases, corresponding to a lowering of the backpressure;
- the drop diameter d_d increases; a bigger drop penetrates better due to aerodynamic effect;
- the injection pressure increases (Figure 2.9); this phenomenon implies both an increase of the initial velocity and a better atomization of the jet.

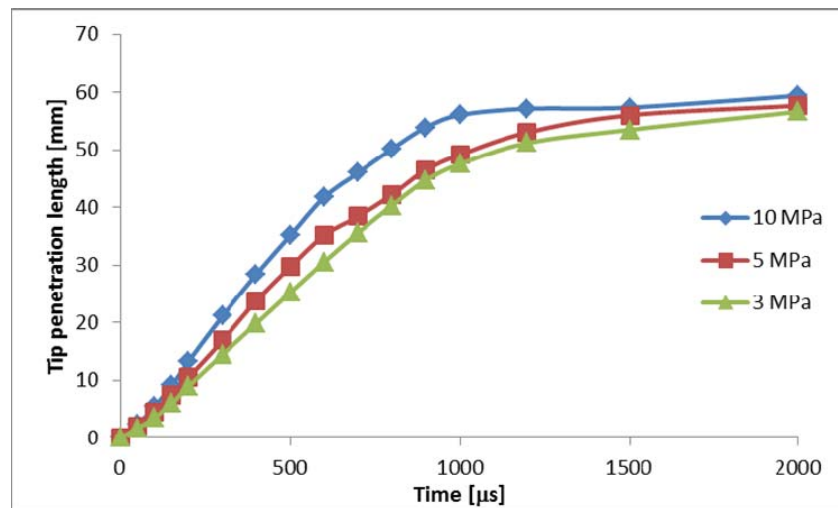


Figure 2.9 – Influence of injection pressure on penetration of non-evaporating spray with a backpressure of 0.1 MPa.

Spray penetration plays a key role for GDI engine performance. Too high spray penetration length leads to impingement of fuel on the combustion chamber walls; on the other hand, if the penetration length is inadequate, the air-fuel mixture results almost incomplete. Optimum engine performance is obtained when the spray penetration is well matched to the combustion chamber size and geometry.

Diffusion rate can be estimated through the spray cone angle, that is the angle between the tangents to the spray envelope [4]. The jet opening angle depends on the backpressure (or better on ratio of air density to fuel density) and on the nozzle geometry, particularly on the ratio between the nozzle length and its diameter. In fact, longer walls guide the jet better, preventing its opening.

Generally, two diffusion angles are identified: one at the exit of the injector hole and the other at a fixed distance from the nozzle exit (Figure 2.10).

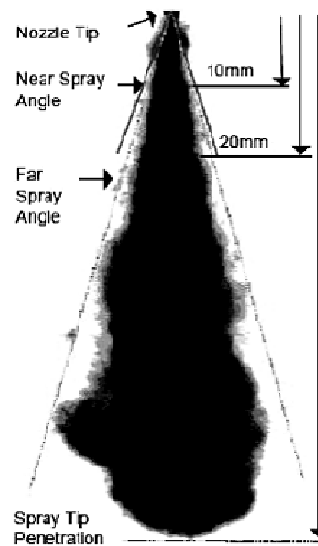


Figure 2.10 – Diffusion angles in a spray produced by an electro-injector.

In GDI engines, the fuel is directly injected into the combustion chamber through the nozzle. The jet, getting away from the nozzle, becomes turbulent and its external surface breaks up into many droplets. The air quantity inside the spray increases, the spray diverges, its width increases while the velocity decreases. Fuel droplets gradually evaporate when the air is incorporated in the jet. The jet penetrates further as the injection advances.

The penetration area becomes longer and wider by increasing the air temperature, due to a lowering of the air density in the cylinder [9].

To improve the combustion process and to reduce the concentration of unburned hydrocarbon to the exhaust, it is necessary to obtain a spray with a long penetration length and a great cone angle. In this way, a maximum air quantity is exploit and the combustion is optimized according to the increase in spray area.

2.3.3 Microscopic parameters

The atomization regime is determined by injection conditions: at low injection pressure, the velocity is poor and the drops have a diameter greater than the nozzle hole, while, at increasing velocities, the mean diameter of the drops becomes small leading to an improvement of atomization. In fact, the break-up of the fuel into a multitude of smaller droplets is a necessary condition to obtain a wide surface-volume ratio able to promote the evaporation process.

As aforementioned, the drops size is a function of the injection time and of the local position inside the jet. Hence, a distribution law is used for characterizing the spray behaviour in terms of drops size and mean diameter, generally represented by the Sauter mean diameter [10].

A good spray evaporation is important to achieve an optimal mixture of fuel and air.

Three phenomena influence the evaporation process of the droplets:

- droplet deceleration due to aerodynamic resistance;
- heat transfer from air to droplet;
- mass transfer from liquid to vapour.

When the drop gets in touch with the hot air in the combustion chamber, the fuel vapour pressure and the evaporation rate increase due to heat transfer. The vaporization process is fundamental because it influences ignition, stability and propagation of the flame.

REFERENCES

- [1] Arcoumanis, C., Gavaises, M., & French, B. (1997). Effect of fuel injection processes on the structure of diesel sprays (No. 970799). SAE Technical Paper. DOI 10.4271/970799.
- [2] Aleiferis, P. G., Serras-Pereira, J., Van Romunde, Z., Caine, J., & Wirth, M. (2010). Mechanisms of spray formation and combustion from a multi-hole injector with E85 and gasoline. *Combustion and Flame*, 157(4), 735-756. DOI 10.1016/j.combustflame.2009.12.019.
- [3] Cameretti, M. C., & Tuccillo, R. (2007, January). Flow and Atomization Models for CR Diesel Engine CFD Simulation. In ASME/IEEE 2007 Joint Rail Conference and Internal Combustion Engine Division Spring Technical Conference (pp. 451-461). American Society of Mechanical Engineers. DOI 10.1115/JRC/ICE2007-40068.
- [4] Lefebvre, A. (1988). *Atomization and sprays* (Vol. 1040, No. 2756). CRC press. ISBN 9780891166030.
- [5] Fraser, R. P., Eisenklam, P., Dombrowski, N., & Hasson, D. (1962). Drop formation from rapidly moving liquid sheets. *AIChE Journal*, 8(5), 672-680. DOI 10.1002/aic.690080522.
- [6] Reitz R. D. (1978) *Atomization and Other Breakup Regimes of a Liquid Jet*, Ph. D. thesis, Princeton University.
- [7] Liu, Z., & Reitz, R. D. (1997). An analysis of the distortion and breakup mechanisms of high speed liquid drops. *International journal of multiphase flow*, 23(4), 631-650. DOI 10.1016/S0301-9322(96)00086-9.
- [8] Ferrari, G. (2008). *Motori a combustione interna. Il capitello*. ISBN 8842670227.

[9] Suh, H. K., & Lee, C. S. (2008). Experimental and analytical study on the spray characteristics of dimethyl ether (DME) and diesel fuels within a common-rail injection system in a diesel engine. *Fuel*, 87(6), 925-932. DOI 10.1016/j.fuel.2007.05.051.

[10] Heywood, J. B. (1988). *Internal combustion engine fundamentals* (Vol. 930). New York: McGraw-hill. ISBN-10 007028637X.

Chapter 3

Fuel injection rate measurements

As widely discussed in the previous chapters, a correct managing of the air-fuel mixing process of direct injection systems is crucial for maximizing the efficiency and for reducing the exhaust emissions of the internal combustion engines. In fact, an accurate fuel metering allows to precisely manage the mass rate of the fuel injected in the combustion chamber and hence to control the spray development and fuel atomization. This is crucial for adjusting the air-fuel mixing because it affects the combustion mechanism and thus the engine performance and exhaust emissions [1-4].

For a complete characterization of the combustion system operation, the injection behaviour has to be investigated and properly calibrated, taking into account the combustion chamber shape and the in-cylinder flow field in a wide range of operating conditions. This issue can be addressed and solved through a complete experimental and numerical analysis [5]. Several experimental techniques can be applied for analysing the spray evolution, such as digital imaging, Phase Doppler Anemometry, Particle Image Velocimetry, X-ray tomography. Anyway, the injection system hydraulic behaviour, in terms of fuel metering accuracy and injection rate control capability, is the basis for controlling the spray formation and evolution and consequently the combustion process.

The results of an experimental campaign for the measurement of instantaneous fuel injection rate of a 6-hole nozzle for DISI Engines are shown in this chapter.

3.1 Experimental set-up

The experimental set-up for the fuel injection rate measurements is composed of a commercial high pressure Direct Injection (DI) system for Spark Ignition (SI) engine and an injection Gauge Rate Meter system, working on the Bosch tube principle [6].

The investigated injector is a 6-hole with solenoid actuation.

The solenoid current profile has been acquired from the engine electronic control unit (ECU) for different operative conditions. It has been reproduced by a home-made programmable ECU (PECU) for driving the injector and synchronizing the acquisition devices. The injection can be activated via external trigger and it is possible to set the main injection parameters: solenoid current profile shape and duration, number of injection events per cycle, rise time, dwell time and injection pressure.

3.1.1 The injection system

Figure 3.1 shows a sketch of the injection system: it could be ideally divided in two parts: a low pressure (blue) and a high pressure (red) circuit.

The low pressure circuit is composed of a tank, an electrical pump and a filtering system. The low pressure pump gets fuel from the tank and feeds, after filtering, the high pressure pump, at a pressure of about 0.4 MPa. The filtering system is used to clean the fuel by any solid particle in suspension and the condensate water formed in the tank.

The high pressure pump is a volumetric one with 3 pistons, radially placed (radialjet) at angular distance of 120° ; it compresses the fuel at high pressure, up to 15 MPa, and sends it to rail. The pump is driven by an asynchronous electric motor of 2.2 kW.

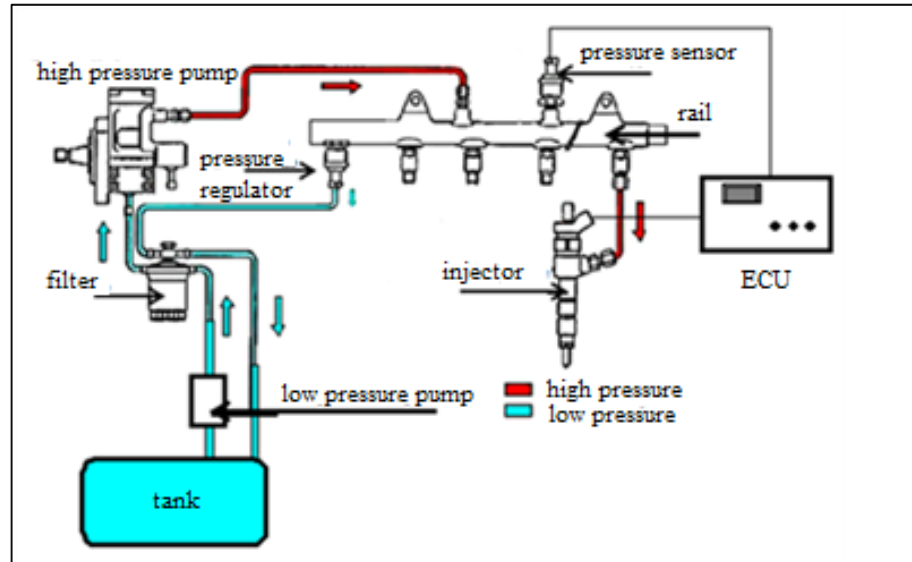


Figure 3.1 - Injection System

Each pumping unit has two valves (a poppet one for the suction and a spherical one for the delivering) and their alternating motion is obtained by a triangular cam keyed on the pump shaft. The compressed fuel is sent to the rail for dampening pressure fluctuations caused by the pulsating pump supply and the intermittent opening of the injectors. A pressure regulator and a pressure sensor are placed on the rail for setting the injection pressure.

The injection pressure, the start and duration of the injection are managed by an electronic control unit (ECU) that regulates the opening of the electro-injector.

Experiments have been performed using a six-hole Magneti Marelli IHP3-264 with solenoid actuation, 9.0 g/s static flow @ 10 MPa with 0.140 mm hole diameter and a

duct length ranging from 0.168 to 0.266 mm depending on hole positioning with respect to the injector axis. They have a L/D ratio from 1.2 to 1.9, respectively.

Figure 3.2 shows the hole configuration and jets axes inclination with respect to the nozzle body. This particular arrangement is designed for optimizing the spray distribution inside the combustion chamber of the reference engine (Fiat 16v 1.4L GDI TC) and for reducing impingement phenomena. A slope of the jets axes is necessary since the injector is side mounted in the combustion chamber, opposite to the spark plug. The fuel used for experiments is commercial gasoline with an octane number of 95 and density of 720 kg/m^3 .

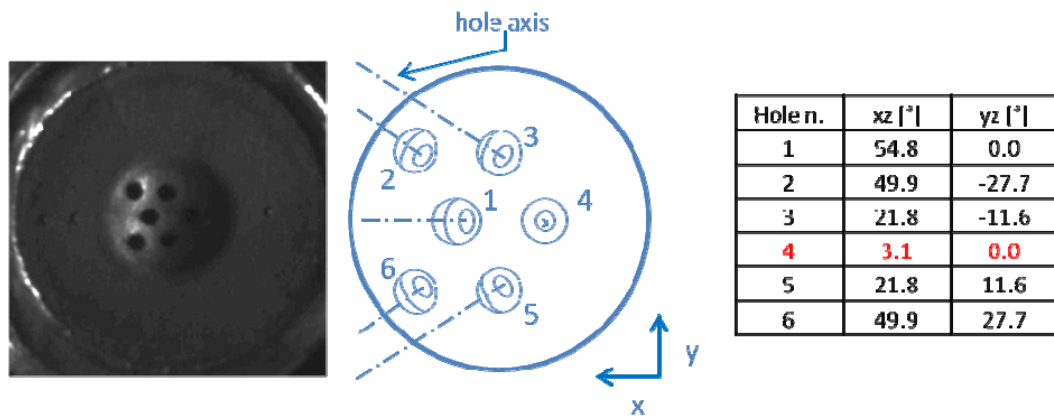


Figure 3.2 - Nozzle image (left), sketch (centre) with jets position referred to the nozzle axis and jets axes inclination with respect to the nozzle body.

3.1.2 The Bosch tube

Several techniques can be applied for the measurement of the injection hydraulic behaviour, such as: momentum flux [7-8], Zeuch's [9-10] and Bosch's method [11].

With the momentum flux method the impingement force of the spray on a surface is estimated through a force sensor. Considering the fluid at the nozzle-exit in liquid-phase flowing through the hole area with a constant velocity, the instantaneous values of

momentum and mass rate can be easily estimated [12]. This method is widely used for investigating the properties of diesel sprays because it can provide information about each single jet composing the spray and cavitation area. Looking at the DISI nozzles, the use of this technique is limited by the spray configuration; in fact, due to the low opening of the cone-angle, it is impossible to limit the impact of fuel on the sensitive surface to a single jet.

Using the Zeuch method, the spray is injected in a closed, fixed-volume chamber filled with the same injected fluid. In the measuring chamber, the pressure level before the injection event is constant. The fuel delivering in the control volume induces a pressure variation proportional to the instantaneous injection rate [9].

Similarly to the Zeuch method, the Bosch method consists of an injection into a fuel filled measuring chamber with a specific backpressure [13]. Downstream a tube, with properly designed length and cross area, reduces the back pressure signal oscillations [14] and the interference with the returning shock wave. The discharged fuel produces a pressure increasing inside the tube proportional to the amount of the fuel mass.

Figure 3.3 shows the AVL injection rate meter used for the experimental tests. Specifically, the Bosch Tube Gauge Rate System collects the single shot through the detection of the pressure increasing induced by the entering fluid in the control volume. The control volume is a small chamber, located immediately downstream of the nozzle, equipped with a transducer, which detects the instantaneous changes in pressure due to the fuel introduction. The used pressure transducer is a GM12D-AVL. The detected electrical signal is amplified by a charge amplifier AVL 3057-V01. The measurement resolution is determined by the time base of the transducer-amplifier system.

Downstream the control volume, a hydraulic tube filled with gasoline lowers the pressure oscillations and delay the return back.

The tube has a total length L of 12 m, 4 mm inner diameter. This inside diameter determines the magnitude of the pressure waves. The length of the measuring tube affects the attenuation efficiency of the device and the measurable injection frequency. In fact, longer is the tube later is the shock waves reflection (period $2L/a$, where a is the sound speed in the fuel).

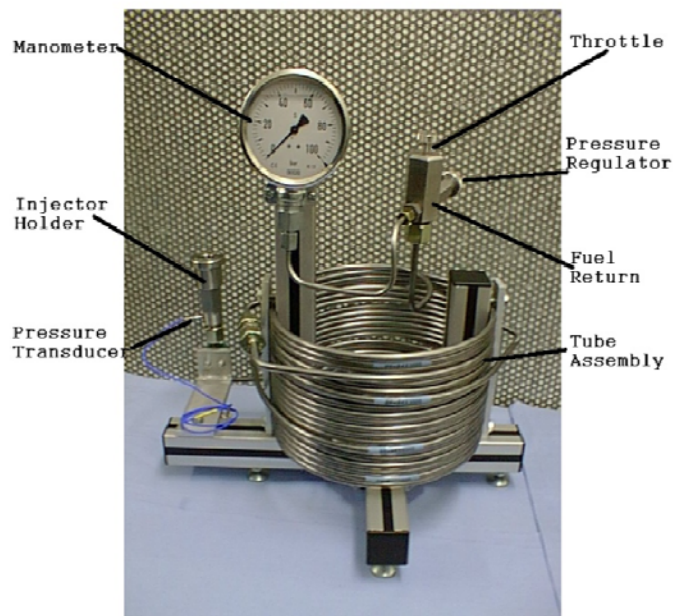


Figure 3.3 - AVL Injection Gauge Rate System.

The size of the orifice determines which part of the fuel transported with the pressure wave is reflected and which part enters the follower tube. If the orifice is too large, most of the transported fuel passes through the orifice and a negative pressure wave is reflected back into the measuring tube. At the end of the duct, a calibrated control valve regulates the pressure in the pipe keeping constant the pressure to avoid cavitation effects by draining the excess of fuel generated by incoming new fuel.

The instantaneous fuel injected mass is proportional to the pressure variation through parameters related to the geometry and to the chemical-physical characteristics of the fuel, as reported in formula 3.1:

$$\dot{v} = \frac{\Delta p_{gauge} \cdot A_{tube}}{a \cdot \rho} \cdot 10^5 \quad (3.1)$$

where \dot{v} is the instantaneous volume fuel rate [mm³/s], Δp_{gauge} [bar] is the pressure change, A_{tube} is the area of the tube inner section [mm²], a is the sound speed in the fluid [m/s], ρ is the fluid density [kg/m³]. Once the flow rate has been estimated, the total injected amount in the period [t_{i-inj} , t_{f-inj}] is:

$$V = \int_{t_{i-inj}}^{t_{f-inj}} \dot{v} \cdot dt \quad (3.2)$$

The results obtained by the fuel injection meter have been compared with the weight of the fluid averaged on 1000 shots, collected at the valve exhaust, by a high precision balance (OHAUS Explorer 410GX1) having a precision of 0.001 g.

3.2 Operative conditions and results

The tests have been performed at two different injection pressures (P_{inj}) 5 MPa and 10 MPa. The injection durations have been calibrated to achieve a relative AFR of about 1.1, corresponding to mass injection rate (m_{inj}) of 26 mg/str, in order to reproduce a wide open throttle condition for the SI engine described in the chapter 7 of this dissertation. The corresponding injection durations are: 2900 μ s at 10 MPa and 4000 μ s at 5 MPa [15].

Figure 3.4 shows the relationship between the solenoid current command and the corresponding injection rate at 10.0 MPa. The typical shape of solenoid injector energizing current has been observed: after a transition peak at about 12 A for lifting the needle, the current is kept constant for the whole injection duration to a holding level around 4 A.

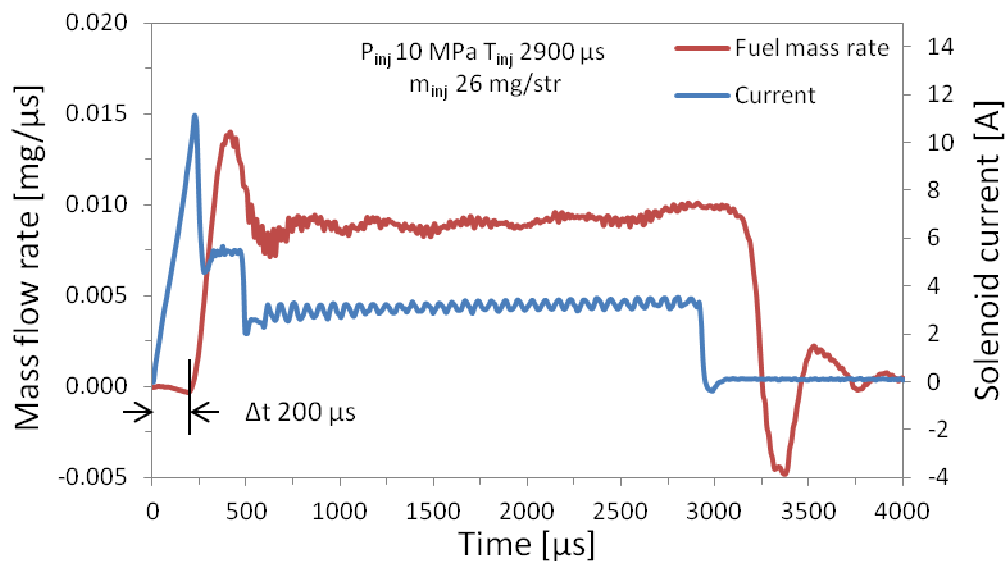


Figure 3.4 - Solenoid current command and corresponding fuel injection rate at 10 MPa injection pressure.

The fuel mass rate shows an almost constant trend up to end of the injection. A quick increase of signal is recorded at the start. The needle is rapidly lifting due to the excitation current to solenoid and a strong increase in flow section area is obtained. The signal peak is likely due to the pressure oscillations in the measuring chamber; even if the circuit is filled with gasoline at a backpressure of about 0.5 MPa, it is not high enough for removing the signal fluctuations at the start of injection when the momentum is maximum. On the other hand, a higher backpressure value could affect the measurements lowering the estimated flow rate with respect to the actual one.

A delay of about 200 μs has been recorded between the start of the solenoid current and the first evidence of fuel injection rate signal due to the inertia of the needle in the injector. At the end of the injection, damped oscillations have been found because of fluid dynamic effects in the Bosch tube [16].

The comparison between the mass flow rates at the two different investigated injection pressures is shown in figure 3.5. As aforementioned, the durations have been adjusted for spraying the same fuel amount; hence an injection current time of 2900 μs has been set at 10 MPa and 4000 μs at 5 MPa.

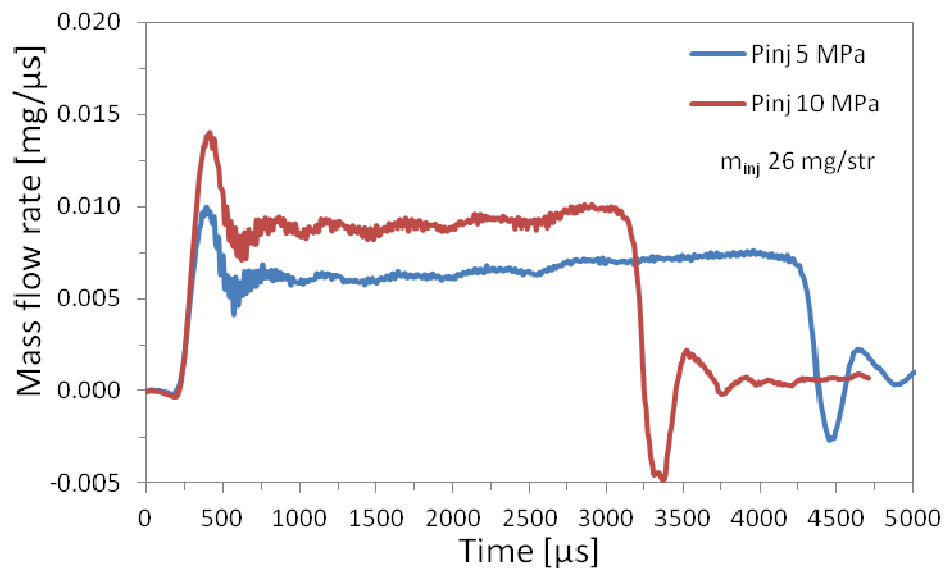


Figure 3.5 - Fuel injection rate profiles for the different injection pressures: 5MPa and 10 MPa.

Though the pressure enhances the needle lift, the same injection delay of 200 μs and the same delay to nozzle close of 300 μs have been found for both the tested pressures.

For both investigated conditions, after a transient stage corresponding to the needle lift, the flow rate is almost constant even if the 5 MPa curve provides a slightly increasing trend at the end indicating a less stable behaviour. As expected, the higher injection

pressure induces an increase in mass flow rate, allowing to reduce the injection time and hence to rise the time available for air-fuel mixing when working in the engine.

REFERENCES

- [1] Postrioti, L., Mariani, F., & Battistoni, M. (2012). Experimental and numerical momentum flux evaluation of high pressure Diesel spray. *Fuel*, 98, 149-163. DOI 10.1016/j.fuel.2012.03.043.
- [2] Heywood, J. B. (1988). *Internal combustion engine fundamentals* (Vol. 930). New York: McGraw-Hill. ISBN 0-07-028637-X.
- [3] Baumgarten, C. (2006). *Mixture formation in internal combustion engines*. Springer Science & Business Media. DOI 10.1007/3-540-30836-9.
- [4] Winter, J., Dittus, B., Kerst, A., Muck, O., Schulz, R., & Vogel, A. (2004). Nozzle hole geometry—a powerful instrument for advanced spray design. *Konferenzband Valencia: Thiesel*.
- [5] Lucchini, T., D'Errico, G., Onorati, A., Bonandrini, G., Venturoli, L., & Di Gioia, R. (2012). Development of a CFD approach to model fuel-air mixing in gasoline direct-injection engines (No. 2012-01-0146). *SAE Technical Paper*. DOI 10.4271/2012-01-0146.
- [6] Bosch, W. (1966). The fuel rate indicator: a new measuring instrument for display of the characteristics of individual injection (No. 660749). *SAE Technical Paper*. DOI 10.4271/660749
- [7] Matsuoka, S., K. Yokota, and T. Kamimoto. "The measurement of injection rate." *Proceedings of the Institution of Mechanical Engineers, Conference Proceedings*. Vol. 184. No. 10. SAGE Publications, 1969. DOI 10.1243/PIME_CONF_1969_184_323_02.
- [8] Payri, R., Garcia, J. M., Salvador, F. J., & Gimeno, J. (2005). Using spray momentum flux measurements to understand the influence of diesel nozzle geometry on spray characteristics. *Fuel*, 84(5), 551-561. DOI 10.1016/j.fuel.2004.10.009.

- [9] Postrioti, L., Buitoni, G., Pesce, F. C., & Ciaravino, C. (2014). Zeuch method-based injection rate analysis of a common-rail system operated with advanced injection strategies. *Fuel*, 128, 188-198. DOI 10.1016/j.fuel.2014.03.006.
- [10] Takamura, A., Fukushima, S., Omori, Y., & Kamimoto, T. (1989). Development of a new measurement tool for fuel injection rate in diesel engines (No. 890317). SAE Technical Paper. DOI 10.4271/890317.
- [11] Costa, M., Sorge, U., & Allocca, L. (2012). CFD optimization for GDI spray model tuning and enhancement of engine performance. *Advances in Engineering Software*, 49, 43-53. DOI 10.1016/j.advengsoft.2012.03.004.
- [12] Payri, R., García, A., Domenech, V., Durrett, R., & Plazas, A. H. (2012). An experimental study of gasoline effects on injection rate, momentum flux and spray characteristics using a common rail diesel injection system. *Fuel*, 97, 390-399. DOI 10.1016/j.fuel.2011.11.065.
- [13] Bower, G. R., & Foster, D. E. (1991). A Comparison of the Bosch and Zuech rate of injection meters (No. 910724). SAE Technical Paper. DOI 10.4271/910724.
- [14] Dernote, J., Hespel, C., Foucher, F., Houille, S., & Mounaïm-Rousselle, C. (2012). Influence of physical fuel properties on the injection rate in a Diesel injector. *Fuel*, 96, 153-160. DOI 10.1016/j.fuel.2011.11.073.
- [15] Marchitto, L., Merola, S., Tornatore, C., & Valentino, G. (2014). Experimental Study on the Spray Atomization of a Multi-hole Injector for Spark Ignition Engines Fuelled by Gasoline and n-Butanol (No. 2014-01-2743). SAE Technical Paper. DOI 10.4271/2014-01-2743.
- [16] White, F.M., *Fluid mechanics*, Mc Graw Hill, 1986. ISBN 9781438919478.

Chapter 4

High Speed Visualization and Particle Image Velocimetry

It is well known that the combustion efficiency strongly depends on the air/fuel mixture, which is strongly connected to the fuel injection into the combustion chamber. Exhaust emissions can be significantly reduced by accurate control of the spray characteristics and the air/fuel mixture formation [1-2]. Improving the atomization increases the fuel surface/volume ratio and improves the contact with the surrounding air, facilitating a complete combustion [3].

The investigations concerning the fuel spray behaviour can be classified in two main classes: macroscopic and microscopic. The macroscopic parameters such as the cone angle and tip penetration are estimated through direct visualization techniques [4-6] as Mie scattering and Laser Induced fluorescence (LIF). The microscopic parameters such as droplets velocity and size are measured through Particle Image Velocimetry (PIV), Laser Doppler Velocimetry (LDV) and Phase Doppler Anemometry (PDA) techniques [7-9]. PDA and LDV can provide information about the spray atomization and droplets velocity [10-11]. However these techniques are strongly limited by the local nature of

the measurements. On the other hand, PIV can provide the overall spray velocity field in a plane corresponding to a Nd:YAG laser sheet [12].

In order to better understand the basics of spray characteristics in internal combustion engines, the previously reported experimental methodologies have been applied by other research groups in ambient pressure and in temperature constant volume vessels [1, 13].

This chapter presents the results of optical investigations providing information about the liquid spray morphology, tip penetration, cone angle and velocity vector distribution of the liquid fuel droplets. In particular 2D Mie-scattering visualization and PIV technique have been applied to characterize the spray of commercial gasoline from the 6-hole nozzle for Direct Injection Spark Ignition (DISI) Engine. Technical specifications of injector have been detailed in Cap. 3. Measurements have been carried out in an optically accessible injection vessel at ambient temperature and pressure.

4.1 Experimental set-up

This section describes the experimental setup for the optical characterization the fuel spray. The tests have been performed in a quiescent vessel: the injector has been located within a chamber with an optical access on a side for image acquisition, and a second one at 90° , used for the laser illumination. The injector has been mounted with the axis coincident to that of the chamber. Figure 4.1 shows the layout of experimental setup.

A pulsed twin head Nd:YAG laser illuminates the fuel jets emerging from a high pressure direct injection system while a CCD camera collects the scattered light. The main geometrical parameters of spray, such as tip penetration and jet cone angle, have been characterized through digital imaging while the Particle Image Velocimetry (PIV) technique has provided information about the spray flow field.

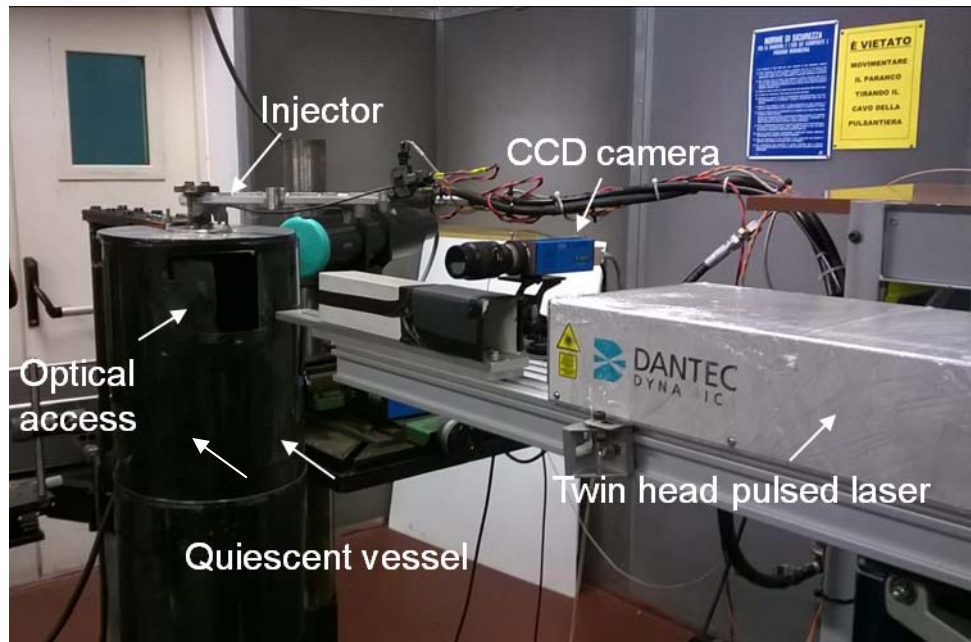


Figure 4.1 – Experimental apparatus.

The experimental setup consists of three parts: the GDI injection system (par. 3.1.1.), the synchronization system for phasing of the injection events with lighting and image acquisition, the PIV system, composed of a pulsed Nd:YAG laser and a CCD camera.

4.1.1 Synchronization system

An accurate synchronization of optical acquisition and lighting system with the injection event is necessary to perform PIV measurements. Figure 4.2 shows a sketch of synchronization flow chart.

A pulse generator (model 9514 of Quantum Composers) has been used for managing the injection timing, the PIV timer box and the FLC shutter. It allows to generate up to four output pulses, it can work in external or internal trigger mode.

For this experimental campaign, a first TTL signal is sent to the electronic control unit (ECU) for generating the energization signal to the solenoid injector. The TTL works as a gate signal for injection timing: the electronic injection start, duration and end are the

same of the TTL. A second TTL is sent to the Timer Box, which controls the CCD camera and the laser timing. The last signal is sent to an external shutter, used for setting the second frame exposure time of CCD when the double frame mode is selected. Further details about the CCD camera and the issues related to its managing will be provided in the next section.

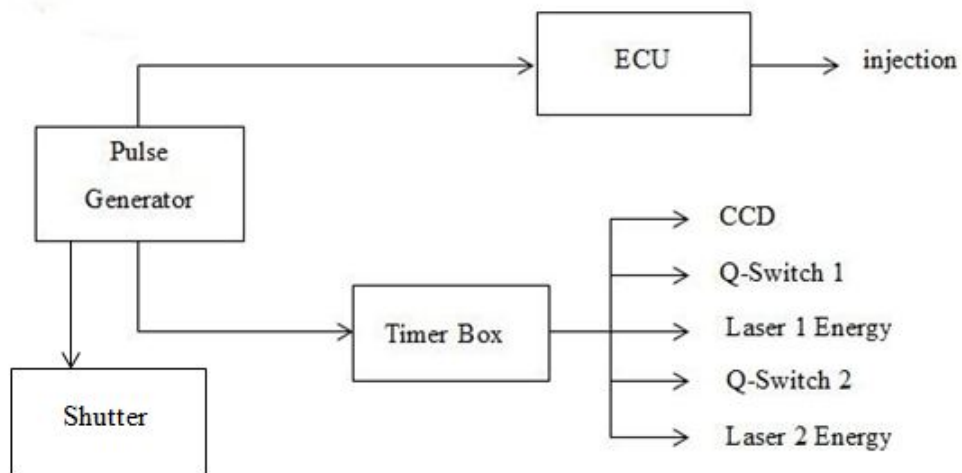


Figure 4.2 – Synchronization system.

The spray behaviour is not affected by the injection frequency; hence, it is kept low for leaving enough time to clean the injection rig. The injection duration has been set for injecting the same fuel amount of 26 mg/str at all the investigated operative conditions, as discussed in the chapter 3.

4.1.2 PIV system

The PIV system, used for characterizing spray geometry and flow field, is composed of a CCD camera and a twin head pulsed Nd:YAG laser. A dedicated software allows to manage the data acquisition and signal post-processing.

4.1.2.1 CCD Camera

The image acquisition has been performed through a pco.2000 cooled 14bit CCD camera. Table 4.1 lists the detector characteristics.

Table 4.1 – Specifications of CCD camera [14].

Sensor size	2048×2048 pixel
Frame Rate @Full Resolution	14.7 fps
Image Sensor	KAI-4022
Minimum exposure time	500 ns
Active Area	15.6×15.3 mm ²
Sensor Diagonal Dimension	21.9 mm
Pixel size	7.4×7.4 μm ²
Dynamic range	14 bit

CCD cameras ensure high quality image and low noise/signal ratio thanks to their quantum efficiency (QE) that is better than higher speed CMOS cameras. The QE is the ratio between the incident photons and converted electrons of the camera sensor. In CCD sensor the quantum efficiency is about 50% in visible range [15], while CMOS sensor reaches about 30%.

The Charge-Coupled Device (CCD) sensor is a thin silicon surface divided into a regular array of thousands or millions of light-sensitive capacitors, or pixels. They capture and store image information in the form of localized electrical charge varying with incident light intensity. These elements are coupled, so that each capacitor, stimulated by an electrical pulse, transfers its contents to its neighbour. The last capacitor in the array dumps its charge into a charge amplifier, which converts the charge into a voltage signal.

CCD cameras work at lower acquisition rate than CMOS ones due to the different signal conversion. In the CCD sensor the charge is transported across the chip and read at one corner of array; hence it is equipped with only one analog-to-digital converter per line. Instead, CMOS devices convert charge to voltage pixel by pixel.

Since the Particle Image Velocimetry measurements need of two image acquisitions with a tight time interval, some modifications are necessary for using CCD cameras. In this work, even if the maximum acquisition frequency of the PCO.2000 is 14.7 Hz, the “double frame mode” option allows to acquire two consecutive images per each trigger signal with a time interval smaller than 1 μ s. The first exposure time can be set up to a minimum of 500 ns. During the readout time of the first image, the second exposure occurs. The second exposure time cannot be directly adjusted; its length is exactly determined by the readout time of the first image. This results in an exposure time of 68 ms for the second frame. The inter-frame time, that is the transition time between the end of first exposure and the start of second exposure, can be reduced up to 180 ns. The CCD camera, placed at 90° with respect to the laser sheet, is connected to a frame grabber and is driven by a dedicated pulse generator (timer box) for synchronization of laser pulses and camera. Images have been taken lining up the light sheet to a plane containing the injector axis. An external ferroelectric liquid crystal shutter is mounted in front of the image sensor in order to regulate the second frame exposure time.

4.1.2.2 Nd:YAG Laser

A twin head pulsed Nd:YAG laser (Litron NANO-L 200-15-Figure 4.3) has lighted a section of the spray structure. Nd:YAG (neodymium-doped yttrium aluminium garnet) is a crystal that is used as a lasing medium for solid-state lasers [16].



Figure 4.3 – Laser used in the experiments.

Pulsed Nd:YAG lasers are typically operated in the Q-switching mode. This technique allows to emit energetic pulses with higher peak power, higher pulse energy and longer pulse duration if compared with a beam produced by a continuous wave mode. Q-switch can be considered as a variable attenuator inside the laser's optical resonator; the pulses are obtained modulating the intracavity losses, which corresponds to a variation of the factor (Quality factor) of the laser resonator. Initially the Q-factor is kept low due to high resonator losses and thus the laser cannot emit. The energy pumping accumulates into gain medium. When stored energy reaches maximum level, the resonator losses are reduced and the Q-switch device is changed from low to high Q factor allowing to begin the optical amplification process of stimulated emission. The power of laser radiation in the laser resonator increases rapidly due to the large amount of stored energy; but at the same time also the reduction in the energy stored is quick. The effect is a high intensity, pulsed beam.

The two laser heads allow to deliver a high intensity double laser pulse, with a time interval short enough for performing PIV measurements even on fast phenomena. The two heads are mounted on a common aluminium chassis and the beams are combined

using polariser plates, before passing through a harmonic generator placed on the same chassis. The first and the second laser beam are combined in the beam combining polariser. Since there is always a slight loss through the beam combining and steering polarisers, ceramic beam dumps are used to catch the uncombined energy.

Each single laser head is composed of:

- Resonator housing: the laser body is machined from a solid piece of aluminium; its rigid design gives high mechanical rigidity and thermal stability.
- Pumping chamber: it comprises a rod holder and separate lamp holder. They both contain two coupled diffuse ceramic reflectors, which give highly uniform pumping to the laser rod. The laser rod and lamp are separated by a tough ionic glass filter that totally absorbs all of UV radiations emitted by the flashlamp.
- Pockels cell: it is an electro-optic modulator consisting of a cylindrical KD*P (potassium di-deuterium phosphate) crystal that is totally immersed in an index matching fluid to protect it from any moisture generated during the flashlamp change procedure. It is the basic component for Q-switching lasers; in fact it is used for controlling the polarization of laser beam, which is modulated by applying a variable electric voltage [17].
- Quarter-wave plate and polariser: they are used to hold off energy within the cavity. Light passes through the polariser and is horizontally polarised. It then passes through the Pockels cell, which with no bias voltage applied does not affect the polarisation. The quarter wave plate divides the passing light into two polarisations, one of which undergoes a 90° phase shift in relation to the other. The light leaving the quarter wave plate is thus circularly polarised.

Upon reflection off the rear mirror, the light once again passes through the quarter wave plate and again one polarisation undergoes a further 90° phase shift, leading to vertically polarized light exiting the quarter wave plate. This light passes back through the Pockels cell and is reflected out of the cavity by the polarizer, preventing any pulse build up. When bias voltage are applied to the Pockels cell, an additional 90° phase shift in one polarization is added in each pass, this leads to a total phase shift of 360° or 0° , and therefore horizontally polarized light is returned and passes through the polarizer allowing the laser beam pulse to build up [18].

The maximum output energy of this laser is 230 mJ at 532 nm, with a repetition rate of 15 Hz. The laser beam is shaped in a sheet with a thickness of about 0.2 mm and a height of 60 mm through an appropriate optical path composed of a series of spherical and cylindrical lenses.

4.2 Particle Image Velocimetry principle and methodologies

Particle Image Velocimetry (PIV) is a technique for instantaneous planar velocity field measurements, widely used in experimental fluid mechanics, based on the estimation of displacement of fine particles following the fluid flow [19].

The CCD camera acquires the signal emerging from the light scattering of the spray illuminated by the laser sheet, with an acquisition frequency of 2 Hz. The exposure time for the first frame is fixed at 5 μ s, while the second frame exposure time is kept below 80 μ s by means of the external ferroelectric liquid crystal shutter.

The laser pulse time must be short enough (5 ns for the present work) to freeze the particles motion during the pulse exposure in order to avoid blurring of the image [20].

In order to obtain vector maps representing the motion field in the time, a Lagrangian approach is used. A single particle p of flow is followed and its position is revealed in the two subsequent frames.

The velocity is determined as the ratio between the two displacement components of the particle p in the time interval of the two light pulses, Δx_p and Δy_p respectively, and the time between pulses Δt .

$$|\mathbf{v}_p(\mathbf{x}, t_i)| = \frac{|x_p(2) - x_p(1)|}{\Delta t} = \frac{|\Delta x_p|}{\Delta t} \quad (4.1)$$

The time between laser pulses must be long enough to evaluate the displacement of particles with sufficient resolution while short enough to avoid particles with an out-of-plane velocity component leaving the light sheet between subsequent illuminations [13]. For the present activity, the well-known “one-quarter formula” has been used to estimate the time pulse delay Δt [21]:

$$\frac{|v|_{max} \cdot \Delta t}{s} \leq 0.25 \cdot (N_{IA} \cdot d_{pixel}) \quad (4.2)$$

where v_{max} is the maximum velocity value expected in the motion field, s is the scale factor, N_{IA} is the final size of interrogation area and d_{pixel} is the pixels size.

Since it is possible individuate a single particle on the image but it is not possible follow its displacement, statistical methods are used.

Images are divided in smaller investigation areas. The signal corresponding to each area is analyzed for finding the local displacement between first and second frame, assuming that the displacements within the considered window are homogeneous. In this way, each area is associated with a displacement vector, and hence a velocity vector, which represents the fluid behaviour in considered zone.

The overall velocity field is then obtained through a light intensity peak correlation method.

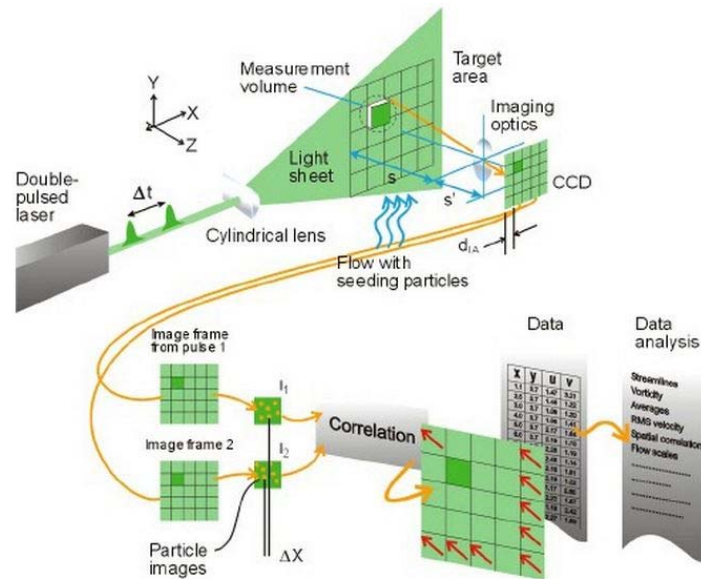


Figure 4.4 – Operating principle of PIV [22].

Figure 4.4 shows the sequence of operations necessary to characterize the fluid flow, starting from the images acquisition until the extraction of the data and their consecutive analysis.

The most simple correlation algorithm is the cross-correlation which allows to obtain a velocity vector map for each pair of acquired images, based on the intensity of the light scattered from liquid drops.

Supposing that $I_1(\mathbf{x})$ and $I_2(\mathbf{x})$ are the transmitted light intensities of frame 1 and frame 2, the two-dimensional spatial convolution of these quantities with separation vector \mathbf{s} is used for obtaining the image displacement [23]:

$$R(\mathbf{s}) = \int I_1(\mathbf{x})I_2(\mathbf{x} + \mathbf{s})d\mathbf{x} \quad (4.3)$$

It is convenient to decompose the estimator for cross-correlation into three components:

$$R(\mathbf{s}) = R_c(\mathbf{s}) + R_d(\mathbf{s}) + R_f(\mathbf{s}) \quad (4.4)$$

where R_c is the convolution of the mean intensities, R_f is the fluctuating noise component of the correlation estimator and R_d is the displacement correlation which gives the image displacement. This peak represents the most common displacement of particles present in the investigation area. The velocity is obtained as the ratio between the coordinates of the peak and the time Δt . This operation is repeated over all areas which compose the image, achieving the i -th velocity vector map.

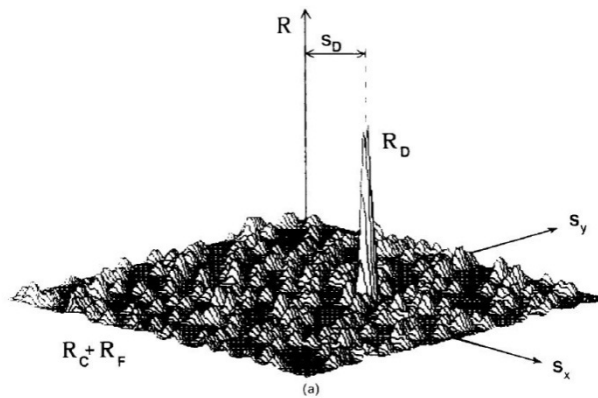


Figure 4.5 – Composition of peaks in the cross-correlation function R [12].

A more advanced algorithm is the adaptive correlation, which utilizes variable window sizing and window shifting methods, in order to reduce the errors associated with conventional cross-correlation [24].

The adaptive correlation method carries out cross-correlation procedure starting from an larger interrogation area moving to the smaller final interrogation area, using the intermediate results as the information for the next interrogation area of smaller size, until the final IA is reached.

Moreover, some filters are used to further reduce the false samples. The local validation is generally applied to the adaptive correlation in order to discriminate the sample over

the noise and an overlap of interrogation areas is often used to compensate the loss of vector field resolution during the processing.

High velocity gradients can drastically reduce the quality of cross-correlation peaks. Increasing the gradients, the peak height decreases with a consequent reduction of the signal to noise ratio. Hence the probability to obtain a spurious measurements is higher. To limit this effect, an accurate sizing of the interrogation area size is necessary, taking into account the one-quarter rule (4.2).

Figure 4.6 shows the adaptive correlation parameters as provided by the Dantec Dynamic Studio software used for the PIV analysis, particularly it is possible to set the final interrogation area size and the number of intermediate steps.

The iterative interrogation process implies that the measurement reliability is increased at each successive iteration. The result of the first interrogation is used as a first estimate of the displacement for the next interrogation step; at each new interrogation this value is refined by using only local information for the estimation of the displacement. In this way, the estimation at each interrogation gets closer to the actual displacement increasing the reliability of the result at each iteration [12].

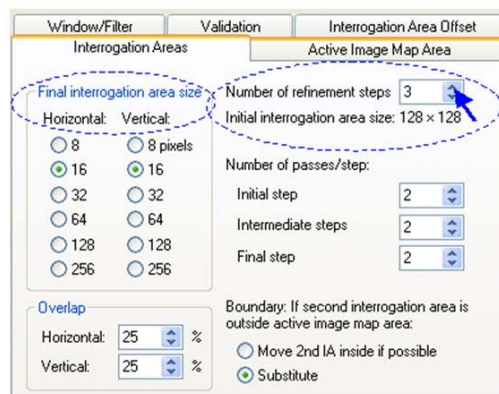


Figure 4.6 – Interrogation areas section of adaptive correlation window

The overlap level between neighbouring interrogation areas can be set in both horizontal and vertical direction depending on the prevailing motion direction. Overlapping allows to reduce the “loss-of-pairs”, since it increases the probability to find both positions of particle in the pair of images. This technique is based on a natural interpolation of motion field, which generates a dependence on the neighbouring measurements.

In this work, a final interrogation area of 32x32 pixels (corresponding to 1.107 mm) has been set with 2 refinement steps; the initial interrogation area was equivalent to 128x128 pixels, corresponding to 4.429 mm; 50% horizontal and vertical overlapping was performed. Some validation parameters for adaptive correlation has been used in combination to fine-tune the processing and to remove spurious vectors.

As aforementioned, the cross-correlation peak represents the average displacement of the particles and it is clearly higher than noise peaks. However, in some cases the peaks could provide comparable widths and therefore a criterion for discriminating the signal from the surrounding noise is necessary. One of the most effective method is the Peak Height Validation which establishes a minimum noise threshold for validating the vector. Considering the two taller peaks, $R_{max,1}$ and $R_{max,2}$, the *Peak Height Validation* criterion defines that the measurement is valid if [12]:

$$\frac{R_{max,1}}{R_{max,2}} \geq k_1 \quad (4.5)$$

In the present work k_1 has been equal to 1.5.

The displacement-correlation peak is affected by the experimental conditions, such as the image density, the in-plane and out-of-plane fluid motion and the spatial gradients.

For a more deeper understanding of the interaction jet-air at the nozzle exit where the velocity gradient is higher and the spray is denser, a second set of measurements was

performed by increasing the spatial resolution. Even if the field of view was reduced by 70.820 mm to 28.126 mm, the scale factor was improved up to 1:1.86. Considering the sensor sizes of 2048 x 2048 pixels and the pixel size of 7.4 μm , the correlation pixels-millimetre resulted 72.8 pixel/mm.

This set-up involved an increase of velocity gradients and thus a higher value of noise to signal ratio. Therefore, a reduction of the ratio between the two taller peak was necessary, from 1.5 to 1.15, in order to obtain more reliable measurements. The related results will be detailed in the next section.

Since the Peak Height Validation reduces the number of valid vector a Local Neighbourhood Validation is applied for substitute the missed velocity values. If an invalid vector is detected, it is removed and replaced by a new vector, estimated as the local interpolation of the vectors present in the neighbourhood area [25].

The sizes of the neighbourhood area is set by the user, as well as the Acceptance Factor, which is used to perform the *Moving Average*.

Given a general vector in (x,y) position, an average of vectors of neighbour area ($N \times N$ sizes) is calculated as:

$$\bar{\mathbf{u}}(x, y) = \frac{1}{N^2} \sum_{i=x-\frac{N-1}{2}}^{x+\frac{N-1}{2}} \sum_{j=x-\frac{N-1}{2}}^{x+\frac{N-1}{2}} \mathbf{u}(i, j) \quad (4.6)$$

In order to accept the vector $\mathbf{u}(x,y)$, it must respect the following relation:

$$\|\mathbf{u}(x, y) - \bar{\mathbf{u}}(x, y)\| < C \quad (4.7)$$

In a first iteration, a global maximum of the difference between the velocity and the average is found. The constant C is equal to:

$$C = k_2 \max_{(x,y)} \|\mathbf{u}(x, y) - \bar{\mathbf{u}}(x, y)\| \quad (4.8)$$

where $k_2 \in [0,1]$ is the Acceptance Factor.

This factor is the parameter used to determine if a vector should be considered as false positive and if it can be replaced by a new vector, calculated by local interpolation with n iterations. At the first iteration the vectors with a larger deviation are deleted and then the average is recomputed until to reach the setting value.

If the Acceptance Factor is too large, the velocity vector map is less spatially correct; on the other hand, if it is too low, the vector map is too smoothed because many vectors are removed.

In this work, an Acceptance Factor equal to 0.15 and an iteration number equal to 3 were set, for performing the *Moving Average*.

Finally, the rejected vector is substituted with the average vector $\bar{\mathbf{u}}(x, y)$.

4.3 Operative conditions and results

For a complete optical investigation of the spray morphology, both macroscopic parameters and microscopic parameters have been estimated.

As aforementioned, the macroscopic parameters have been analyzed through digital imaging, while the spray flow field has been characterized by means of the Particle Image Velocimetry technique.

The two injection strategies calibrated through the fuel injection rate analysis have been tested. The injection duration have been 2900 μs and 4000 μs at 10 and 5 MPa injection pressure, respectively.

As widely discussed in the previous section, the PIV technique is based on a complex scattered light peak correlation algorithm. Hence, a high spatial resolution is required

for providing more accurate measurements of velocity fields. For this reason two different scale factor (SF) have been used for PIV measurements: the first one, hereinafter named as test 1, for maximizing the field of view (FoV) (SF 1:4.67, FoV 70.820); the second one (test 2 below), for maximizing the spatial resolution and get more detailed information on the spray velocity field in the region immediately downstream the nozzle.

Considering the high number of acquisitions for each operative condition (100 couples of images for each operative condition), the PIV analysis has been performed at four different acquisition times, characteristics of the whole spray development: 200 μs , 400 μs , 800 μs and 1200 μs .

The reference time was the effective start of injection, defined as the instant corresponding to the first evidence of fuel delivering detected by digital imaging. An injection delay of 200 μs with respect to the electronic start was estimated, in agreement with fuel injection rate measurements.

The digital imaging has allowed to follow the spray development until the end of injection. The time resolution for the image acquisition has been variable: a 50 μs has been set for characterizing the early stage of the injection, typically less stable, while time interval of 100 μs has been set for the instants after 300 μs .

4.3.1 High Speed Visualization

Figure 4.7 shows sequences of selected images representing the gasoline spray evolution and detecting at fixed injection pressures: of 5 MPa (top) and 10 MPa (down). In both the sequences, the spray propagates compact up to about 200 μs after the SOI due to the high momentum flux at the nozzle exit. At 400 μs after SOI, a small amount of fuel droplets separates by the jet because of the interaction with the surrounding air.

The momentum is high enough to limit this phenomenon to the jet boundaries. 800 μs and 1200 μs after the SOI, the spray continues the propagation and a strong momentum loss occurs due to the drag effect of the surrounding air, particularly on the spray periphery. As a consequence, several droplet clusters leave the spray forming curling shape zones. This behaviour suggests the presence of vortices caused by the impact of the spray against the quiescent air, especially in the spray zone corresponding to the jets with higher slope with respect to the nozzle body [7, 11, 26].

An accurate analysis of figure 4.7 provides preliminary information concerning the injection pressure effect on the spray development. As expected, a comparison of the images at the same acquisition time highlights the faster spray propagation at 10 MPa compared to 5 MPa. Even if a quantitative correlation between the spray mass concentration and signal luminous intensity is not possible, due to the multi-scattering phenomena, the brighter spray images at 10 MPa clearly indicate higher density level because of the presence of higher atomization.

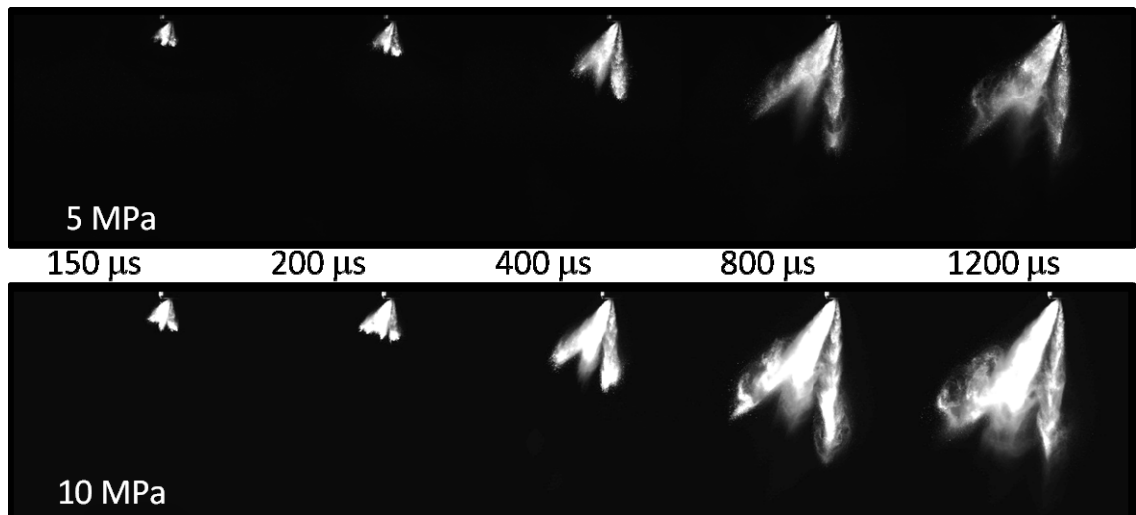


Figure 4.7 – Temporal evolution of the spray carried out in an optically accessible injection vessel at ambient temperature and pressure for two injection pressures.

As widely discussed, the digital imaging can provide quantitative information about the spray geometry and dispersion in the surrounding air. The results of the tip penetration length measurements are reported in figure 4.8, as function of the time after the start of injection (ASOI) at different injection pressures. Three different regions can be distinguished, corresponding to three different stages of the spray evolution. In the first region, the penetration curve linearly grows with respect to the acquisition time with a strong pendency. This region represents the first instants of the injection, in which the momentum value is high. The effect of the interaction between jet and air is low and the jet penetrates compact in the surrounding ambient.

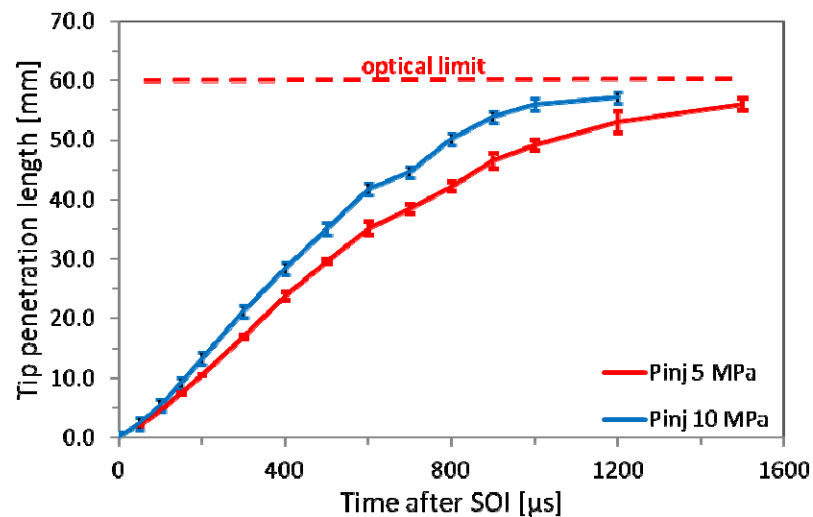


Figure 4.8 – Tip penetration length at selected injection pressures.

In the second region, a strong bending of the curve is observed, indicating a reduction of propagation speed. The drops formed by the primary atomization, are subject to the second break-up, which breaks them into smaller drops with lower momentum. The propagation speed continues to lower and the penetration provides a parabolic trend.

At the end of the curve, the spray is far from the nozzle and the effect of the injection pressure are now mitigated by the spray interaction with the ambient; the momentum is

very low because the drops have exhausted their kinetic energy. Their trajectory is mainly due to the gravity and the curve tends to an asymptotic value.

The effect of the injection pressure on the penetration length is quite evident. The higher injection pressure induce a higher jet velocity, hence both the kinetic energy and the momentum are improved. As the atomization proceeds, the droplets kinetic energy and the momentum gradually decrease, due to the interaction with the air and hence the pressure influence is less significant. It should be noted that the laser sheet height should be taken into account. In fact, the light intensity reduction at the FoV boundaries reduces the measurements accuracy, due to the signal weakness. For this reason measurements were considered valid up to 60 mm, estimated as optical limit.

In order to better evaluate the spray spreading in the chamber jet cone angle measurements have been performed. The related results are shown in figure 4.9. For both injection pressures, the trend is almost constant versus time. This behaviour could be expected [27]. No evidence of the injection pressure effect on the cone angle has been highlighted. Both curves propagates in a range between 14 and 18 deg.

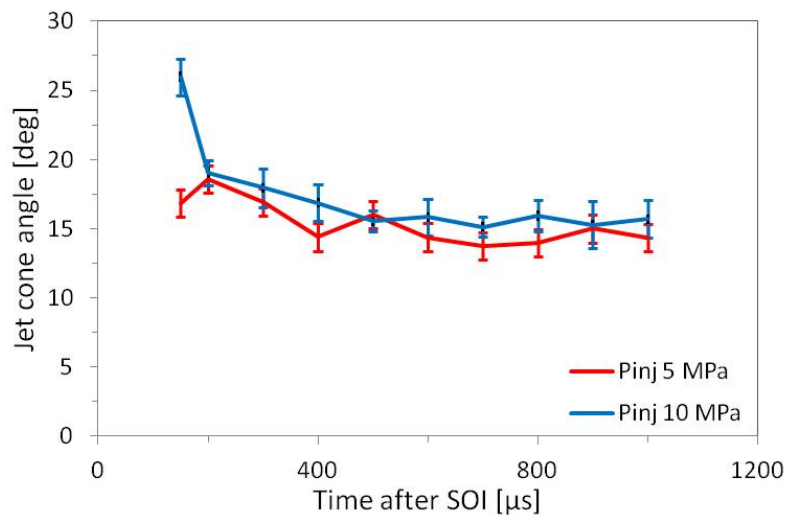


Figure 4.9 – Cone angle in function of the injection pressure.

Two different regions can be distinguished at 10 MPa: in the first region the cone angle rapidly decreases. The break-up is not yet complete and spray is characterized by large ligaments and droplets with high momentum. The interaction with the air is low and it occurs on the spray edges; as consequence, the spray is more compact. As the jet penetrates into the surrounding ambient, the interaction with the air increases, the break-up occurs and the spray widens.

In the second region the break-up goes on, leading up to formation of smaller drops and a decrease of the momentum. In this zone, the cone angle is almost constant. The case at 10 MPa highlights a less oscillating trend than at 5 MPa, indicating a more stable spray dispersion.

4.3.2 Particle Image Velocimetry

The geometrical configuration of the injector IHP3-264 and spray visualization at 1000 μs , obtained fixing the injection pressure at 10 MPa are reported in figure 4.10, while Table 4.2 concerns the inclination of each hole with respect to the laser sheet plane xz and to a second plane yz , perpendicular to the laser sheet plane and containing the nozzle axis z . Three different plumes can be distinguished in Figure 4.10. The first, on the left, is the result of three overlapped jets: 1, 2 and 6.

The jet 1 axis lies in the laser sheet plane. The jets 2 and 6 propagate symmetrically with respect to the laser light plane. The jet 6 is closer to the CCD camera and it covers the jets 1 and 2. The second plume represents the overlap of the jet 5 and 3 behind of it. Only the jet 4 propagates independent from the others and hence has been set for the quantitative measurements.

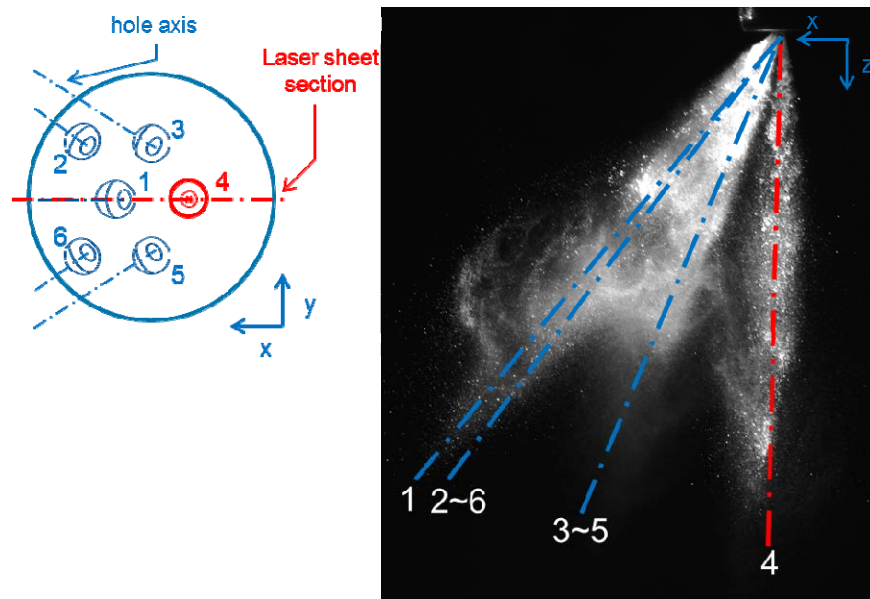


Figure 4.10 –Nozzle bottom view (left) and spray visualization (right) at 1000 μ s, obtained fixing the injection pressure at 10 MPa.

The laser sheet crosses the nozzle diameter and the jets 1 and 4. The CCD is focused on the lighting sheet plane. Since the jet 1 is covered by the jet 6, the measurements concerning the jet 4 are considered more reliable than those carried out on the other five jets. In fact, as aforementioned the PIV measurements are based on light intensity peak correlation, hence a focus loss has a smoothing effect on the signal with an increase in false samples.

Table 4.2 – Tilt angles of injector holes in respect to the axis x and y

Hole	xz [°]	yz [°]
1	54.8	0.0
2	49.9	-27.7
3	21.8	-11.6
4	3.1	0.0
5	21.8	11.6
6	49.9	27.7

The velocity vector maps for each injection strategy, at four different acquisition times is obtained through the adaptive correlation procedure, detailed in the previous section. A time between pulses of $2.3 \mu\text{s}$ has been set, taking into account the “one quarter rule” [19] previously discussed, with a final interrogation area of 32×32 pixels.

First, the maximum FoV is analyzed as it allows a more comprehensive analysis of spray development.

Figure 4.11 shows the vector maps at the injection pressure of 5 MPa. At all the investigated acquisition times the jet 4 achieves the maximum velocity: 82, 89, 84 and 81 m/s at 200, 400, 800 and 1200 μs acquisition time, respectively. Even if similar maximum speed are expected for all the jets composing the spray, an accurate analysis of the nozzle geometry can explain this result. The PIV is a planar measurement, hence the detected values refer to the values of the velocity component in the laser sheet plane. Hence, while the jet 4 propagates in the measurement plane and the PIV detects the effective velocity value, the jet 5 and 6 propagate out of the plane and the measured values represent a component of the actual velocity. Considering the inclination angle with respect to the nozzle body axis as reported in table 4.2 a correction factor of $\cos(11.6^\circ) \sim 0.98$ for jet 5 and of $\cos(27.7^\circ) \sim 0.88$ for jet 6 can be estimated. Anyway this hypothesis is valid only in the region immediately downstream of the nozzle because the jets 5 and 6 propagate out of the laser sheet plane. Since the laser sheet plane coincides with focus plane, far from the nozzle a strong blurring effect impedes further measurements.

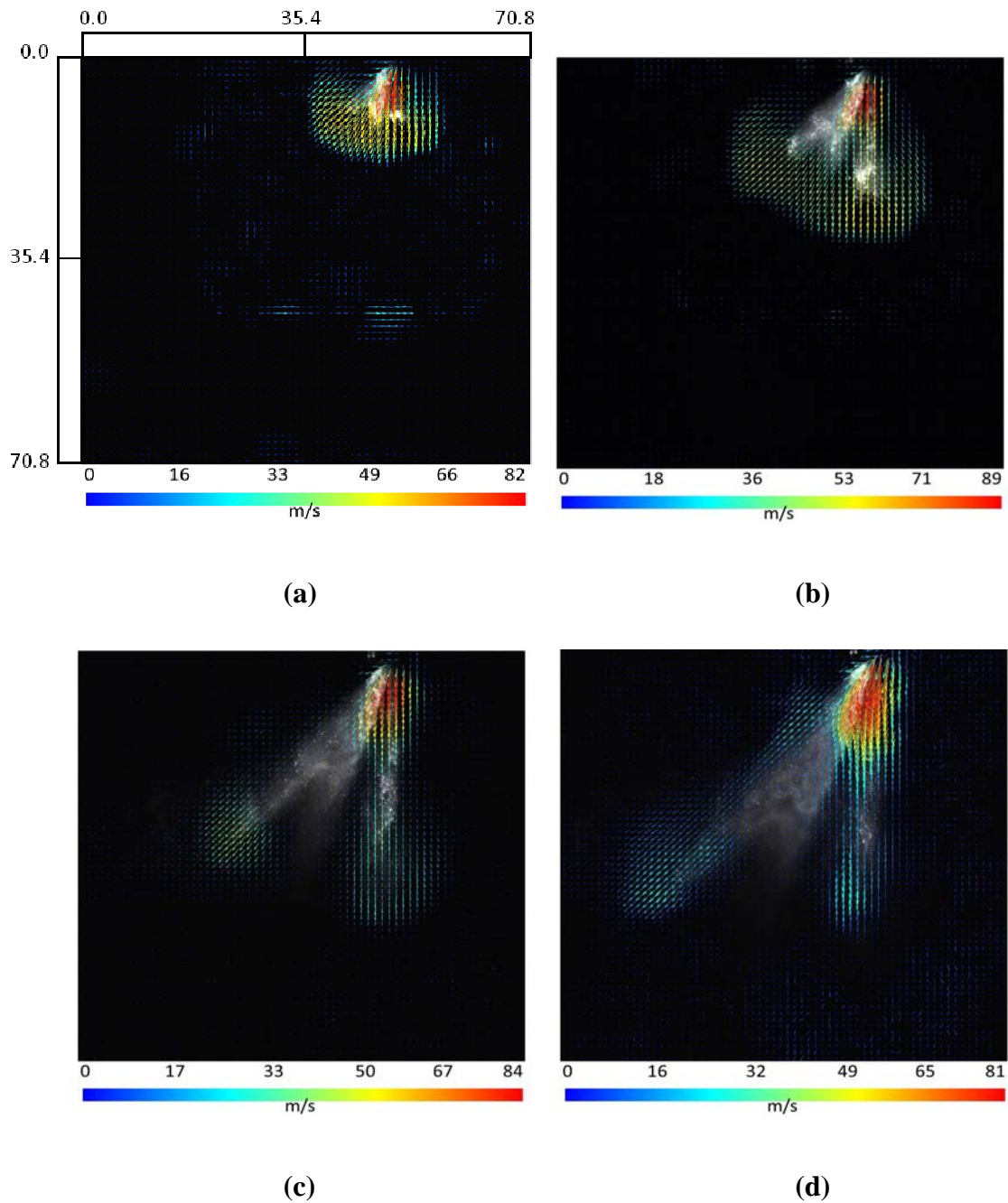


Figure 4.11 – Velocity vector maps at the injection pressure of 5 MPa at 200 μs (a), 400 μs (b), 800 μs (c) and 1200 μs (d)

At 200 μs , the break-up is not effective, the spray is compact, hence the velocity map is almost uniform along the jet profile.

As the atomization proceeds, the spray breaks into smaller droplets and the detected velocity lowers. As a consequence, two motion fields can be clearly distinguished at 400 μs : the first, at the nozzle exit, in which the velocities are comparable with those at 200 μs and the second, further down, in which the break-up is occurred, characterized by smaller droplets with lower velocities.

At 800 μs , the spray is almost full developed, the maximum velocity value is recorded close to the nozzle and it decreases when moving downstream.

The penetration length increases and the distance of the jets 5 and 6 from the camera focal plane grows. As a consequence, the velocity maps lack in wide regions of the spray.

At 1200 μs the break-up phenomena are complete and the spray develops toward steady condition. In Figure 4.12 the vector maps about 10 MPa injection pressure are reported.

The same considerations as for 5 MPa can be done about the effects of the acquisition times on the velocity distribution.

The higher injection pressure increases significantly the spray density and the atomization is enhanced. As consequence the multi-scattering effect is accentuated and, in the region corresponding to the overlap of the jets 3-5 and 1-2-6, the number of validated vectors decreases preventing the measurements even at the earliest time. The jet 4 propagates compact longer than at 5 MPa. In fact, the higher injection pressure implies a greater momentum and consequently the break-up of the spray into droplets occurs further from the nozzle, in spite of the better atomization.

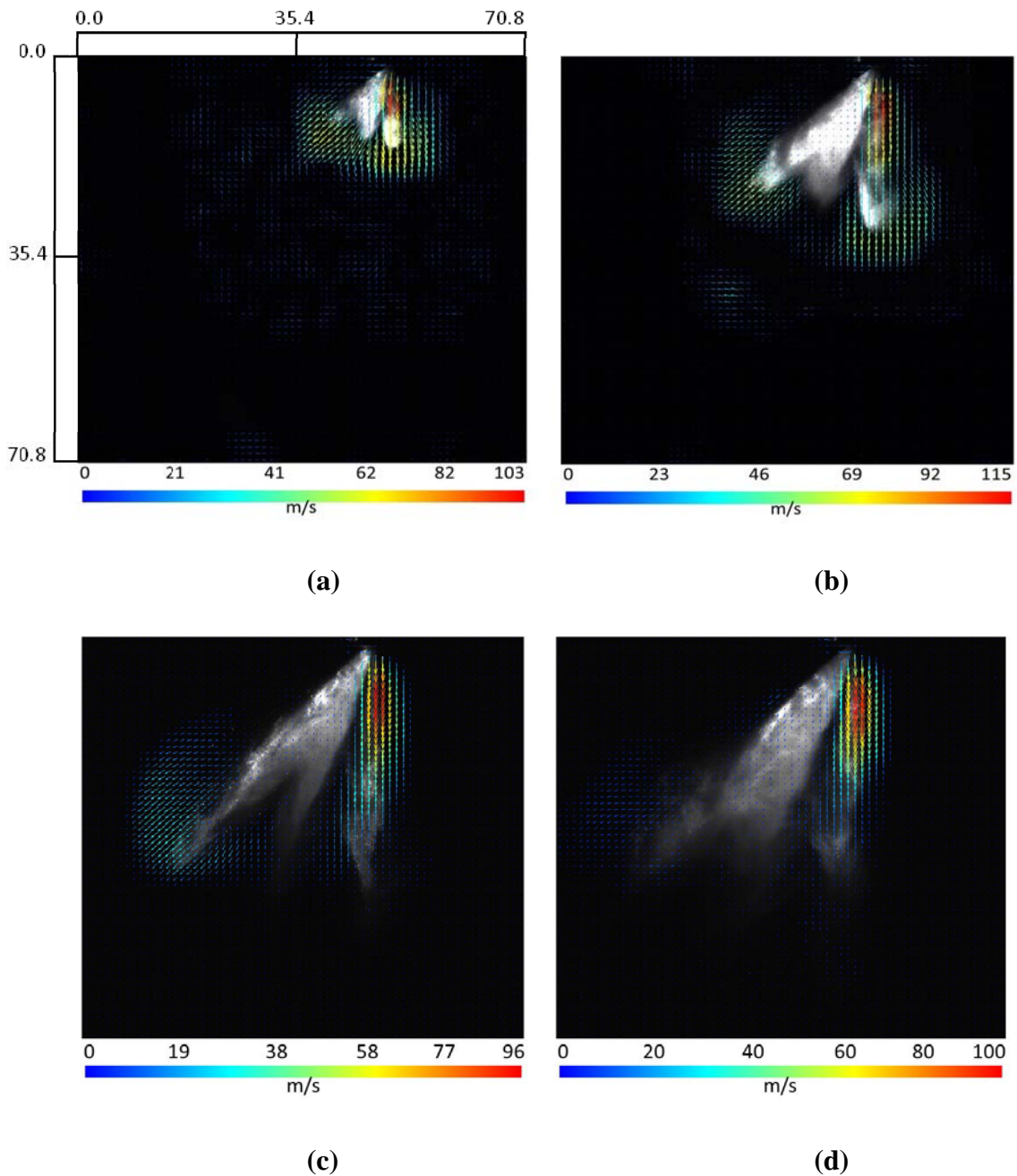


Figure 4.12 – Velocity vector maps at the injection pressure of 10 MPa at 200 μs (a), 400 μs (b), 800 μs (c) and 1200 μs (d)

At 1200 μs the spray edge reaches the laser sheet boundary, in which the luminous intensity is lower; hence it should be taken into account a slight underestimation of the velocities in this region.

At all the injection pressures, the velocity peak at 400 μs is higher than at 200 μs . This behaviour can be explained considering that at 200 μs the injector needle is not yet completely lifted and thus the regime is unsteady.

The velocity increases up to a maximum value at 400 μs , reaching 115 m/s at 10 MPa and 89 m/s at 5 MPa.

For a quantitative analysis of the droplets speed, the profiles along the jet 4 axis have been extracted. Figure 4.13 shows the comparison among the velocity profiles related to the investigated injection pressures at different acquisition times. The velocity is reported as function of the distance from the injector nozzle.

The maximum velocity is reached at about 5 mm from the orifice at all the investigated conditions; particularly, the maximum value is recorded at 400 μs from SOI and it is 115 and 90 at 10 and 5 MPa, respectively.

As expected, at each acquisition time, the higher injection pressure provides the greater velocity. At both 200 μs and 400 μs , the velocity difference between 5 MPa and 10 MPa is around 30 m/s. At 200 μs , the velocity rapidly decreases up to about 5-10 mm from the nozzle, where the first drops clusters separate and break into smaller droplets; after the trend is almost constant up to jet tip, corresponding to a distance from the nozzle of about 12 and 15 mm at 5 and 10 MPa, respectively.

At 400 μs the spray penetration is longer and two phases can be distinguished. In the first one the atomization is occurring and the velocities rapidly decrease up to about 10-20 mm.

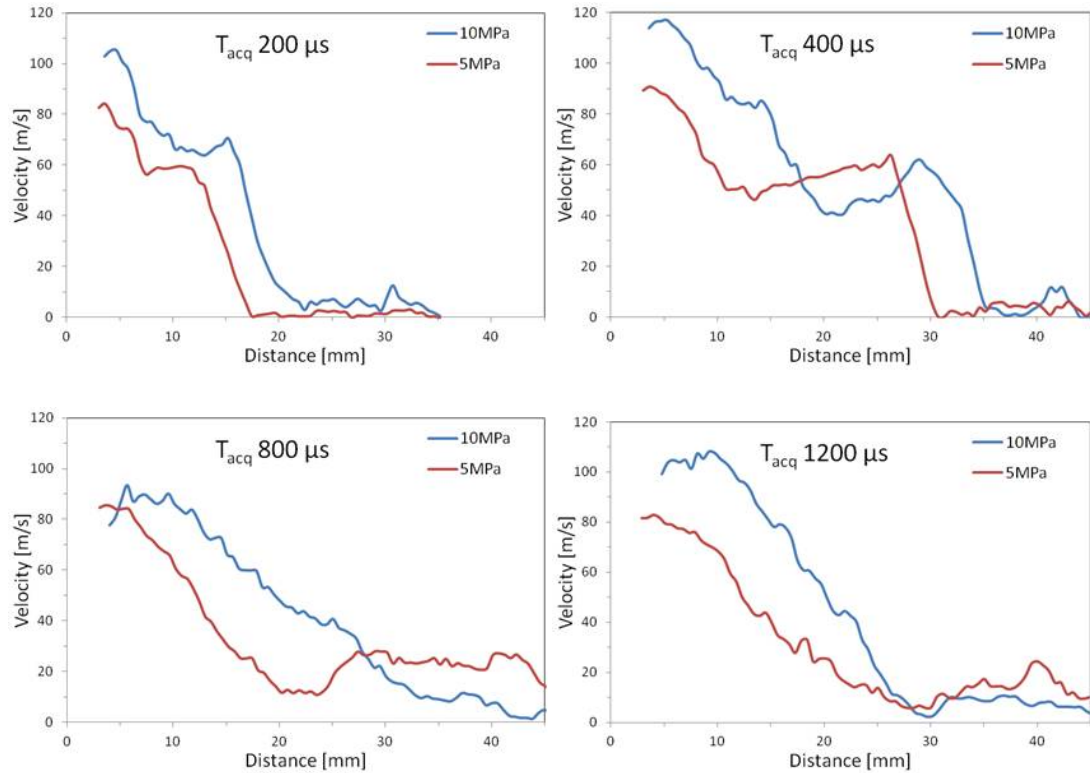


Figure 4.13 – Velocity profiles along the investigated jet axis for selected injection pressure

In the second phase, a slight linear increasing trend is recorded. This region is characterized by coalescent phenomena among the slow droplets, arising from the first atomization, and the faster drops injected later.

At 800 μs the spray develops toward steady conditions. The curves are smoothed: the velocity slowly decreases because the atomization is almost complete.

For better detail the behaviour downstream the nozzle where the break-up phenomena occur the PIV measurements have been repeated by increasing the SF up to 1:1.86, the FoV has been limited to a region sizing $\sim 21.3 \times 21.3$ mm

A final interrogation area of 32×32 pixels (corresponding to 0.44×0.44 mm²) has been set because of the high velocity gradients at the exit of the nozzle. With a greater final interrogation area, the velocity maps result smooth, because the area includes a greater

number of both high and low peaks, and the average among these peaks leads to a lower velocity. Furthermore, a reduction of the ratio between the two taller peaks, from 1.5 to 1.15, has been necessary. The higher velocity gradients, in fact, involve an increase in the noise to signal ratio.

The velocity vector maps related to three injection strategies are reported in the figures 4.14 and 4.15. As expected the maximum speed detected is comparable with one recorded with maximum FoV configuration. A slight difference is evident at 800 μ s for 10 MPa pressure; in which a maximum speed increase has been detected from 96 m/s to 109 m/s. This behaviour can be explained considering that a higher spatial resolution results in a greater capacity to describe the local variations of the motion field. At the earlier injection times the region close to the nozzle, in which the velocity reaches the maximum value, is wider. Hence the smoothing effect caused by the lower spatial resolution doesn't affect the velocity profile. Moreover, the higher scale factor allowed to obtain a better characterization of the motion field related to the jets 5 and 6.

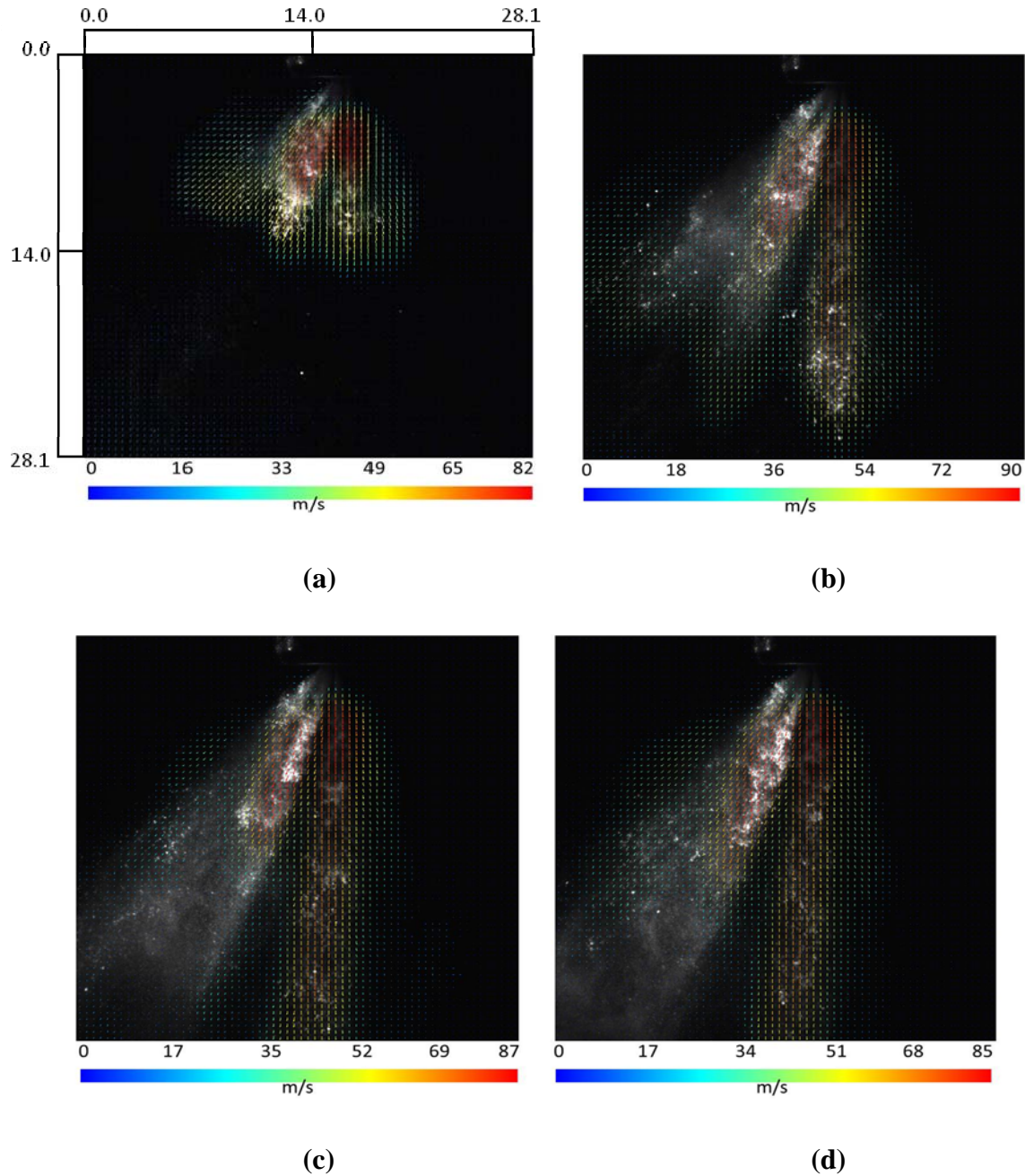


Figure 4.14 – Velocity vector maps at the injection pressure of 5 MPa at 200 μs (a), 400 μs (b), 800 μs (c) and 1200 μs (d)

Particularly at 5 MPa injection pressure, providing less dense sprays, the spray can be quantitatively characterized also far from the jet 4. This is not possible at 10 MPa, because the fuel spray is more dense and the multi-scattering effect is too high.

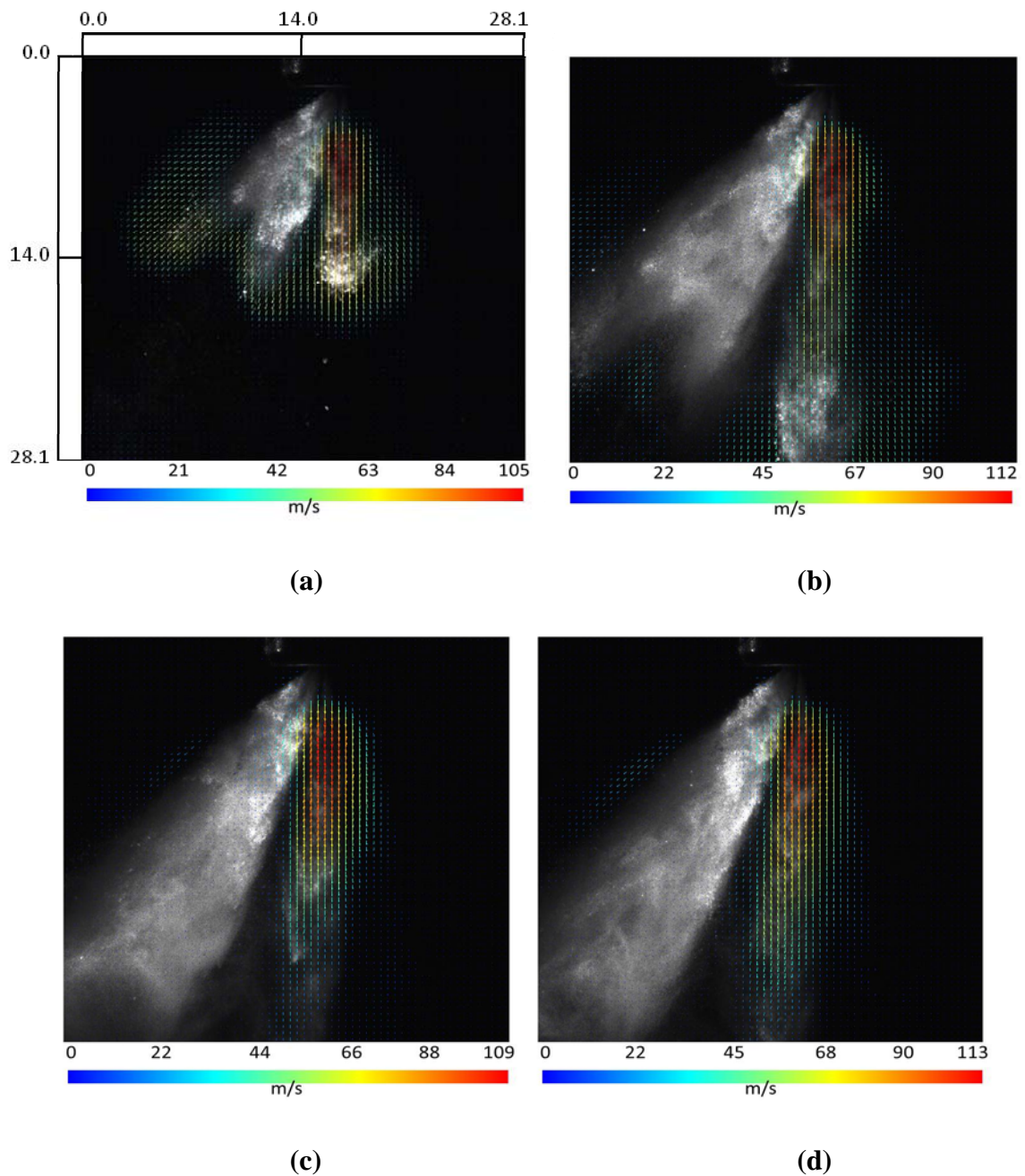


Figure 4.15 – Velocity vector maps at the injection pressure of 10 MPa at 200 μs (a), 400 μs (b), 800 μs (c) and 1200 μs (d)

Even if it is not possible to directly estimate the droplet size through the PIV a first estimate of the break-up regime can be performed by means of the Ohnesorge maps.

The Ohnesorge number is function of Weber number and Reynolds number. The first one depends on the square of velocity, while the second one depends on the velocity and the hole diameter, which is chosen as characteristic length.

Since the Ohnesorge number is defined as the ratio between the square root of the Weber number and the Reynolds number, it is a function of fuel properties and nozzle diameter and it is independent on the velocity. As aforementioned the tests have been performed at ambient temperature and pressure. Hence the fuel properties can be considered constant. For this reason, the Ohnesorge number of gasoline, in this work, is constant and equal to 0.0089.

According to Reitz et al. [28], four different break-up regimes can be individuated on the Ohnesorge diagram:

- Rayleigh break-up: drops diameter is greater than hole diameter;
- First wind-induced regime: drops diameter is about equal to the hole diameter;
- Second wind-induced regime: drops diameter is lower than hole diameter;
- Atomization regime: drops diameter is an order of magnitude lower than hole diameter.

Figures 4.16-4.17 report the Ohnesorge maps at 200 μs and 400 μs from the start of injection, at all the investigated injection pressures. Since the aim is to evaluate the break-up regime, just the position closer to the nozzle have been considered. As expected, a stronger atomization occurs at 10 MPa. As a result all the positions referring to 10 MPa injection pressure are in the right side of the diagram in the region corresponding to the atomization regime. At 5 MPa injection pressure, just the position closer to the nozzle, at 5 mm is placed between the second wind-induced regime zone and the atomization regime zone. However it can be taken into account that the

Ohnesorge diagram has been obtained considering the characteristic length as the nozzle hole diameter. This hypothesis is acceptable immediately downstream of the nozzle.

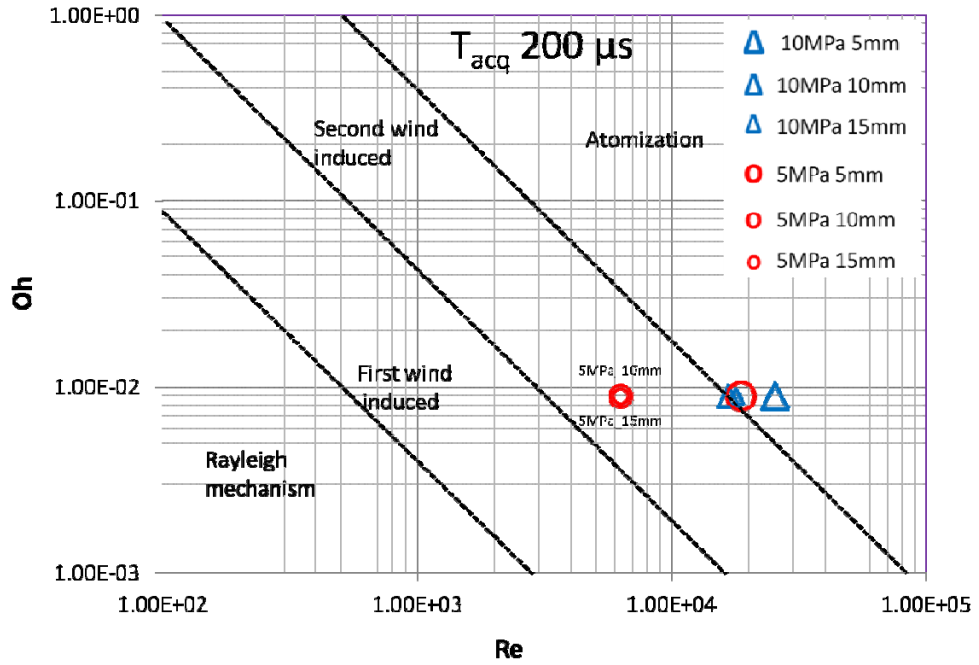


Figure 4.16 – Ohnesorge map at $200 \mu s$.

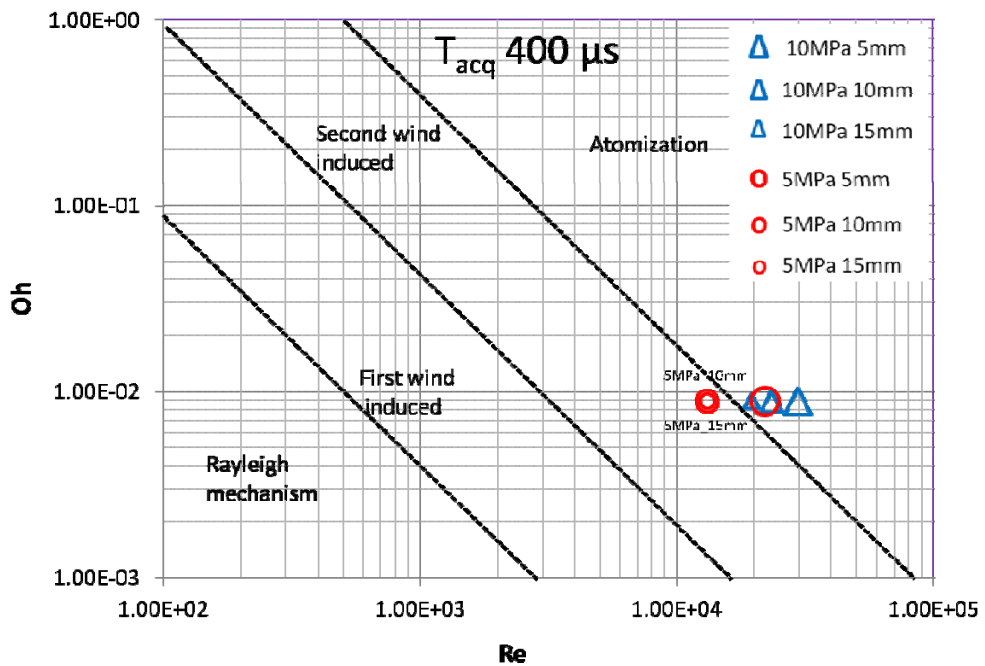


Figure 4.17 – Ohnesorge map at $400 \mu s$.

A shift on the right side of the diagram is evident at all the investigated conditions. At 10 MPa the atomization regime is reached at all the distances from the nozzle, while also the point at 5 mm for the pressure of 5 MPa reaches the atomization regime.

At 10 MPa the break-up also continues far from the nozzle while at 5 MPa it gradually reduces due to a lower momentum, which dissipates earlier.

This shift is caused because at 400 μs the needle is totally and velocities reach their maximum. The 200 μs acquisition time is characterized by a transient regime because the injector needle is lifting and the velocities are still growing. At 400 μs , instead, the needle is completely lifted and thus the maximum velocity value increases in comparison with the 200 μs velocity.

REFERENCES

- [1] Soid, S. N., & Zainal, Z. A. (2011). Spray and combustion characterization for internal combustion engines using optical measuring techniques—A review. *Energy*, 36(2), 724-741. DOI 10.1016/j.energy.2010.11.022
- [2] Han, Z., Fan, L., & Reitz, R. D. (1997). Multidimensional modeling of spray atomization and air-fuel mixing in a direct-injection spark-ignition engine (No. 970884). SAE Technical Paper. DOI 10.4271/970884.
- [3] Su, T. F., Chang, C. T., Reitz, R. D., Farrell, P. V., Pierpont, A. D., & Tow, T. C. (1995). Effects of injection pressure and nozzle geometry on spray SMD and DI emissions (No. 952360). SAE Technical Paper. DOI 10.4271/952360.
- [4] Ipp, W., Wagner, V., Krämer, H., Wensing, M., Leipertz, A., Arndt, S., & Jain, A. K. (1999). Spray formation of high pressure swirl gasoline injectors investigated by two-dimensional Mie and LIEF techniques (No. 1999-01-0498). SAE Technical Paper. DOI 10.4271/1999-01-0498.
- [5] Kim, H. J., Park, S. H., & Lee, C. S. (2014). Light intensity and image visualization of GDI injector sprays according to nozzle hole arrangements. *Optik-International Journal for Light and Electron Optics*, 125(12), 2763-2767. DOI 10.1016/j.ijleo.2013.11.030.
- [6] Marchitto, L., Valentino, G., Merola, S., & Tornatore, C. (2015). Characterization of Alcohol Sprays From Multi-Hole Injector for DISI Engines Through PIV Technique (No. 2015-01-0927). SAE Technical Paper. DOI 10.4271/2015-01-0927.
- [7] Wigley, G., Goodwin, M., Pitcher, G., & Blondel, D. (2004). Imaging and PDA analysis of a GDI spray in the near-nozzle region. *Experiments in fluids*, 36(4), 565-574. DOI 10.1007/s00348-003-0690-1.

- [8] Allocca, L., Alfuso, S., Marchitto, L., & Valentino, G. (2009). GDI multi-hole injector: particle size and velocity distribution for single and jet-to-jet evolution analysis. In *The 11th Triennial Intl. Annual Conf. on Liquid Atomization and Spray Systems*.
- [9] Maeda, M., Akasaka, Y., & Kawaguchi, T. (2002). Improvements of the interferometric technique for simultaneous measurement of droplet size and velocity vector field and its application to a transient spray. *Experiments in fluids*, 33(1), 125-134. DOI 10.1007/s00348-002-0453-4.
- [10] Marchitto, L., Merola, S., Tornatore, C., & Valentino, G. (2014). Experimental Study on the Spray Atomization of a Multi-hole Injector for Spark Ignition Engines Fuelled by Gasoline and n-Butanol (No. 2014-01-2743). SAE Technical Paper. DOI 10.4271/2014-01-2743.
- [11] Aleiferis, P. G., & Van Romunde, Z. R. (2013). An analysis of spray development with iso-octane, n-pentane, gasoline, ethanol and n-butanol from a multi-hole injector under hot fuel conditions. *Fuel*, 105, 143-168. DOI 10.1016/j.fuel.2012.07.044,
- [12] Lee, K. H., Lee, C. H., & Lee, C. S. (2004). An experimental study on the spray behavior and fuel distribution of GDI injectors using the entropy analysis and PIV method. *Fuel*, 83(7), 971-980. DOI 10.1016/j.fuel.2003.10.021.
- [13] Nauwerck, A., Pfeil, J., Velji, A., Spicher, U., & Richter, B. (2005). A basic experimental study of gasoline direct injection at significantly high injection pressures (No. 2005-01-0098). SAE Technical Paper. DOI 10.4271/2005-01-0098.
- [14] <http://www.pco.de/sensitive-cameras/pco2000/>
- [15] Wichmann Verlag, Heidelberg 2001.
- [16] Walter Koechner (1965) *Solid-state laser engineering*, Springer-Verlag.

- [17] RP Photonics Encyclopedia.
- [18] Litron Lasers, Nano Series Nd:YAG Pulsed Laser System, Laser Operators handbook. Version 1 March 2004.
- [19] Adrian, R. J., & Westerweel, J. (2011). *Particle image velocimetry* (Vol. 30). Cambridge University Press. ISBN 9780521440080.
- [20] Raffel M., Willert C., Wereley S., Kompenhans J., Particle Image Velocimetry, A Practical Guide, Springer, 2007.
- [21] Adrian, R. J., & Yao, C. S. (1994). Development of pulsed laser velocimetry (PLV) for measurement of turbulent flow. SPIE MILESTONE SERIES MS, 99, 300-300.
- [22] Dantec Dynamics, Laser Optical Measurements System and Sensors <http://www.dantecdynamics.com/>
- [23] Keane R. D., Adrian R. J., Theory of cross-correlation analysis of PIV images, Applied Scientific Research, 49:191–215, Kluwer Academic Publishers, 1992.
- [24] Liu, J., & Iskander, M. (2004). Adaptive cross correlation for imaging displacements in soils. Journal of computing in civil engineering, 18(1), 46-57. DOI 10.1061/(ASCE)0887-3801(2004)18:1(46).
- [25] Dantec Dynamics, DynamicStudio User's Handbook, 2009.
- [26] Van Romunde, Z., Aleiferis, P. G., Cracknell, R. F., & Walmsley, H. L. (2007). Effect of fuel properties on spray development from a multi-hole DISI engine injector (No. 2007-01-4032). SAE Technical Paper. DOI 10.4271/2007-01-4032.
- [27] Varde K.S., Spray cone angle and its correlation in a high pressure fuel spray, Department of Mechanical Engineering, University of Michigan-Dearborn, April 1985.
- [28] Reitz, R. D., & Bracco, F. V. (1986). Mechanisms of breakup of round liquid jets. Encyclopedia of fluid mechanics, 3, 233-249.

Chapter 5

Phase Doppler Anemometry

As previously discussed, an accurate characterization of the physical processes involving the fuel injection, the liquid breakup and the spray atomization is essential for both optimizing the injection systems and running 3D CFD codes [1-2]. In fact, the liquid jet inner structure influences the fuel dispersion and evaporation; while, the break-up process affects both engine performance and exhaust emission [3-4].

It is well known the importance of investigating the spray structure immediately downstream of the nozzle, because in this region the processes affecting the overall spray development occur [5]. However, this is also a hard challenge due to the elevated density of high pressure DI systems [6]. The high injection pressure favours the break-up of the jet, inducing the formation of droplets one magnitude smaller than the nozzle hole. The spray atomization is necessary for increasing the fuel surface/volume ratio enhancing the evaporation [7].

First information about the spray development and atomization regime has been provided through the spray morphology analysis and Particle Image Velocimetry. PIV measurements have allowed to characterize the spatial distribution of droplet velocity at fixed acquisition times. However, during the injection time, the droplet size and velocity distribution at a fixed location changes depended on the injection conditions, such as the

difference in droplet size at the spray core and spray edge as the atomization process goes on.

In order to characterize spray break-up, droplet size and velocity distributions have been measured through the Phase Doppler Anemometry (PDA) and Laser Doppler Velocimetry (LDV). The most significant results are discussed in the present chapter.

5.1 Experimental set-up

Experiments for the characterization of the spray break-up have been conducted in a quiescent cylindrical vessel, at ambient pressure and temperature. The nozzle has been placed coaxial with the chamber height. A Dantec Dynamics PDA system has been used for the droplets size and velocity measurements. The system is composed of an Argon-ion laser operating at 514.5 and 488 nm, a 310 mm; transmitting optics separate the beam of 65.0 mm and modular collecting optics working in forward scattering mode, at an off-axis of 30°. A single aperture of 0.025 mm has been set into the receiver to limit the scattered light to the detectors. The transmitter and receiving probe have been mounted on a x-y-z translation stage that has allowed the positioning of the probe volume within the spray at different locations, with micrometric accuracy. A pulse generator has been used to trigger the programmable electronic control unit for the injection system and the PDA processor.

The experimental setup can be considered schematically composed of three parts: the GDI injection system (sec. 3.1.1.), the synchronization system for phasing of the injection events with signal acquisition and the PDA system.

5.1.1 Synchronization system

Timing and duration of acquisition and injection have been managed through an Engine Timing Unit (ETU), a pulse generator and an electronic control unit (ECU) (fig 5.1). The ETU can work independent from the engine, simulating a certain rotation speed, in a range between 1000 and 6000 rpm. ETU synchronizes the signals with the engine cycle while the pulse generator receives two input TTL signals coming from an encoder. The inputs are Trigger, in correspondence of the top dead center, and CDM -Crank Degree Medium, with a frequency corresponding to the angular resolution of the Encoder. In this way it is possible to manage the signals as a function of the engine crank angle degree.

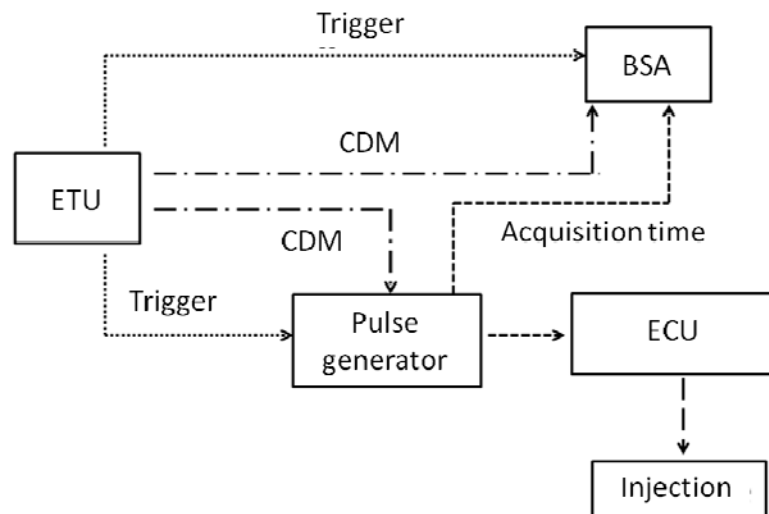


Figure 5.1 –Synchronization flow sketch.

The sampling rate can be reduced with respect to the simulated engine speed, periodically removing the pulses (mode work / rest). The measurements have been performed at 4 Hz frequency, in order to leave enough time for cleaning

the injection chamber by residual drops, without altering the fluid-dynamic conditions.

In the described experiments, ETU has been used for the synchronization of the PDA with the injection system. In particular, the simulated trigger and CDM signals have been sent to the PDA processor while a synchronous signal has been used as external trigger for the pulse generator. The latter activates the injection by a gate signal to the ECU, imposing the injection frequency and duration. A second gate signal is sent to the PDA system to set the photomultipliers acquisition window. A time interval slightly longer than the injection duration is fixed to take into account the injection delay and the flight time of the fuel droplets. CDM establishes the sampling rate of PDA processor. During injection phase, each acquisition provides time resolved data concerning the droplet size and velocity with a time resolution of $\sim 11 \mu\text{s}$.

5.1.2 PDA System

Experimental apparatus for PDA measurements is shown in figure 5.2; it is constituted by:

- Argon Ion laser;
- Transmitting probe;
- Receiving probe;
- Data acquisition processor;
- Data acquisition and post-processing software.

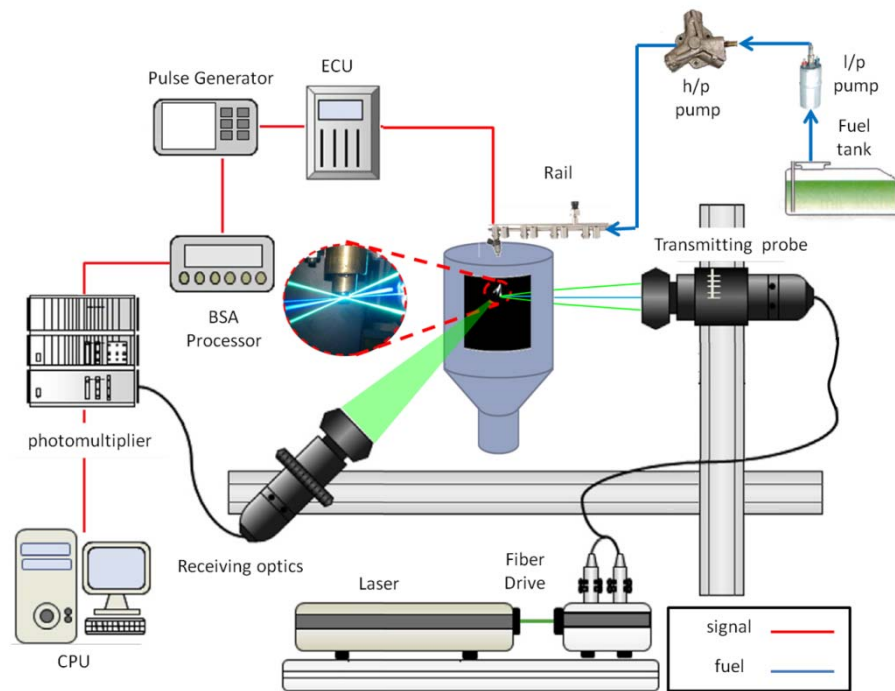


Figure 5.2 – Experimental apparatus.

5.1.2.1 Laser

Argon ions laser is an optical device that uses Argon and Krypton ions as lasing medium. Applying a voltage to the Argon cell, the atoms are excited with an energy equal to the energy of transition between two energy levels (with respect to the ground state). As a result, a cyan light beam is obtained. The emitted laser is focused in the so called “Fiber Drive”.

The Fiber Drive consists of:

- a *neutral beam separator* which separates the incoming laser beam into two beams with the same intensity through a prism;
- a *Bragg cell* which is a beam separator generating two beams: one at the inlet frequency, the second with a frequency shift of 40 MHz;

- A *color separator* which splits each laser beam emerging from Bragg cell in two beams: the first is green with a wavelength of 514.5 nm, and the latter is blue with a wavelength of 488 nm.

The resulting four beams are focused into optical fibers bringing them to a transmitting probe.

5.1.2.2 Transmitting probe

Transmitting probe consists of a set of optics, to focus the four beams in a measurement volume, and of a beam expander to improve the relative distance between the beams. The main features of the probe are: 310 mm focal length, 65 mm distance between the beams. The measurement volume is determined by the interference of the two beams; its dimensions are $d_x \sim 0.2$ mm; $d_y \sim 0.2$ mm; $d_z \sim 2.0$ mm (Figure 5.3); the volume is defined by several interference fringes separated by $\delta_f \sim 2.5$ μm distance.

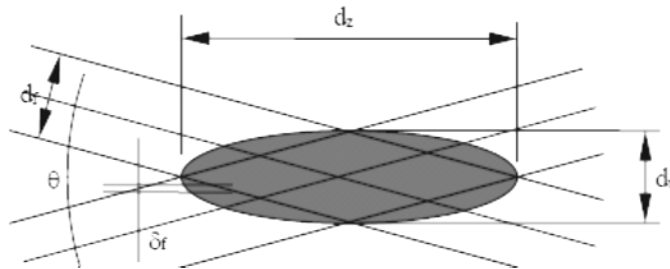


Figure 5.3 – Probe volume.

5.1.2.3 Receiving probe

Receiving probe collects the light diffused by the samples when they cross the measuring volume and then it sends the signal to the photomultipliers PhMs through four optical fibers. PhMs are extremely sensitive detectors that multiply the current produced by incident light, enabling even the detection of

few individual photons when the incident flux of light is very low. The main components of the receiving probe are (Figure 5.4):

- achromatic biconvex lens;
- mask (mask);
- spatial filter (slit).

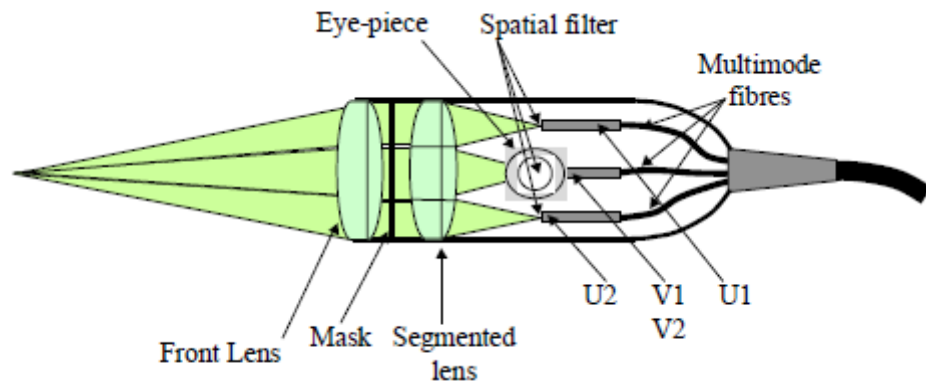


Figure 5.4 - Scheme of the receiving probe

Achromatic biconvex lens with a focal length of 310 mm is a collimator and it has been used for collecting the signal. It converges the beam into a parallel one which is filtered by a plate with appropriate slits to separate the spurious signal from the four components sent to the photomultipliers: U1, U2, V1 e V2. By changing the plate slits shape and the dimension it is possible to set the droplet size measurement range. Downstream the mask it is placed a lens that focuses the light on to a spatial filter (slit) for a more precise tuning of the size range; four values of maximum droplets size can be selected as 25; 50; 100; 200 μm . The final part of the probe is composed of four lenses (segmented lens), which focus the corresponding light portions on the optical fiber connected to the photomultipliers.

5.1.2.4 BSA Processor

Burst Spectrum Analyzer (BSA) is used to process the signal emerging from the receiving probe and to measure the droplets size and velocity. BSA is a dedicated CPU which estimates the phase and frequency shift of the Doppler signals from the photomultipliers. The signals are detected, processed and validated simultaneously and continuously. Specifically, they follow two paths. In the first, signal are filtered through a band-pass to improve the SNR and then they are sent to the spectrum analyzer. After this phase, two electronic mixers multiply the input signals by a sinusoidal signal produced through an oscillator, obtaining two output signals in quadrature. The signals thus obtained are sent a to low-pass filters for eliminating the high frequency noise from the Doppler signal. Analog and digital converters allow the sampling of the signals that are processed by Fourier transform. In the second path a circuit measures the arrival time and the transit time of the signal in the control buffer. The signals cross a low pass filter allowing to obtain the Doppler signal basis; a rectifier and a second low pass filter produce an envelope curve of the Doppler signal. When both the reference and the envelope signals exceed a threshold value, the sampling is activated and the starting and transit time are recorded. If the envelope later reaches a higher threshold the sampling starts again.

5.1.2.5 Data acquisition software

The data acquisition and processing are managed through the Dantec Dynamics BSA Flow software, which allows the real time monitoring of the results and the setting of the following hardware parameters:

- centre frequency and bandwidth for limiting the speed range. A reduced width of the band may exclude useful samples, while a very high value can cause the sampling of false positives;
- photomultiplier high voltage. Higher voltages allow to detect even small particles but could saturate the photomultipliers signal;
- signal gain, which represents Doppler signal amplification. A high signal gain value increases the noise, while small gain can determine poor amplification of weak signals due to smaller particles;

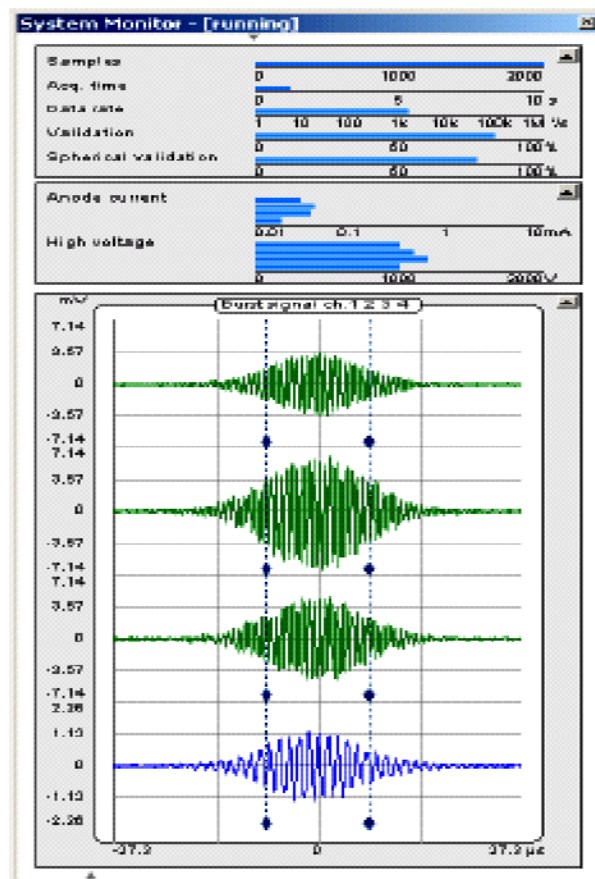


Figure 5.5 – Doppler signal monitor

- spherical validation, to discriminate the droplets crossing the measurement volume by the noise signal. Based on the hypothesis that

droplets are approximately spherical, the ratio between the droplets curvatures in two different positions is estimated and kept below a certain threshold.

The software allows to control the Doppler signals of each photomultiplier, the data rate and sample validation rate (Figure 5.5).

5.2 LDV-PDA principle and methodology

The Laser Doppler Velocimetry (LDV) and Phase Doppler Anemometry (PDA) are optical techniques, based on the Doppler effect of electromagnetic waves, which allow to perform time resolved measurements of droplets size and velocity. These techniques provide some advantages with respect to Particle Image Velocimetry (PIV) previously described. In particular the calibration is not necessary because the measurements are based on the stability and linearity of the optical electromagnetic waves. Moreover LDV and PDA are independent on physical parameters such as temperature and pressure. Further, the small size of probe volume allows to get a high spatial resolution and local measurements of Eulerian speed. The small measuring volume and high dynamic of the electronic process also provide high temporal resolution.

5.2.1 LDV and PDA principle

Similarly to PDA, in LDV setup the light beam emitted by a Ar-ion Laser is focused on a beam splitter to obtain two different beams; a Bragg cell shifts the frequency (40MHz) of one of the two beams; then the beams are collected in the optical fibers and focused in a point by the transmitting probe. Intersection of the laser beams generates a fringes plane (with light and dark zones) parallel

to the bisector of the beams: the measurements are performed when a very small particle, carried by the flow, cross the fringes spreading light with a frequency proportional to the crossing speed in the probe volume: this frequency is defined Doppler frequency (f_d). The size of the tracer particle must be large enough to spread light of sufficient intensity to detect the signal, but small enough to faithfully follow the flow (laminar or turbulent).

The intensity of the incident light on a plane is estimated through the Fresnel equations, as function of incidence and transmission angles, considering the different polarizations: perpendicular (S) and parallel (P):

$$t_s = \frac{2 \cdot \sin \varphi_t \cdot \cos \varphi_i}{\sin(\varphi_i + \varphi_t)} = \frac{2 \cdot n_1 \cdot \cos \varphi_i}{n_1 \cdot \cos \varphi_i + n_2 \cdot \cos \varphi_t} \quad (5.1)$$

$$t_p = \frac{2 \cdot \sin \varphi_t \cdot \cos \varphi_i}{\sin(\varphi_i + \varphi_t) \cdot \cos(\varphi_i - \varphi_t)} = \frac{2 \cdot n_1 \cdot \cos \varphi_i}{n_2 \cdot \cos \varphi_i + n_1 \cdot \cos \varphi_t} \quad (5.2)$$

$$r_s = \frac{\sin(\varphi_i - \varphi_t)}{\sin(\varphi_i + \varphi_t)} = \frac{n_1 \cdot \cos \varphi_i - n_2 \cdot \cos \varphi_t}{n_1 \cdot \cos \varphi_i + n_2 \cdot \cos \varphi_t} \quad (5.3)$$

$$r_p = \frac{\tan(\varphi_i - \varphi_t)}{\tan(\varphi_i + \varphi_t)} = \frac{n_2 \cdot \cos \varphi_i - n_1 \cdot \cos \varphi_t}{n_2 \cdot \cos \varphi_i + n_1 \cdot \cos \varphi_t} \quad (5.4)$$

Where t_s and t_p are the components of transmitted light intensity; r_s and r_p are the components of reflected light intensity; φ_i the incidence angle; φ_t the transmission angle; n_1 and n_2 the refractive indices (Figure 5.6).

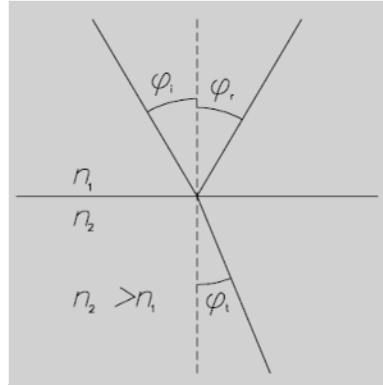


Figure 5.6 - Reflection and refraction of light on a surface.

When a particle is lightened, it scatters light in three different modes (Figure 5.7): reflection from the outer surface of the particle, refraction through the particle (first order refraction) and refraction with one internal reflection (second order refraction).

The mean size of the investigated particles generally varies in a range between 0.1 and 50 μm ; since these dimensions are comparable with the wavelength of the laser light, the analysis of the diffusion can be performed through the Lorenz - Mie theory. This approach is based on the dependency of the scattered light intensity on the particles size, assumed spherical. However, also the shape and orientation of particles affects the light scattering [8].

The particle size affects not only the scattered light intensity (larger droplets scatter more light than smaller) but also the spatial distribution of the scattered light as shown in figure 5.8. For large particles the ratio of forward to backward scattered light can be in the order of 10^2 to 10^3 , while smaller particles scatter more uniformly.

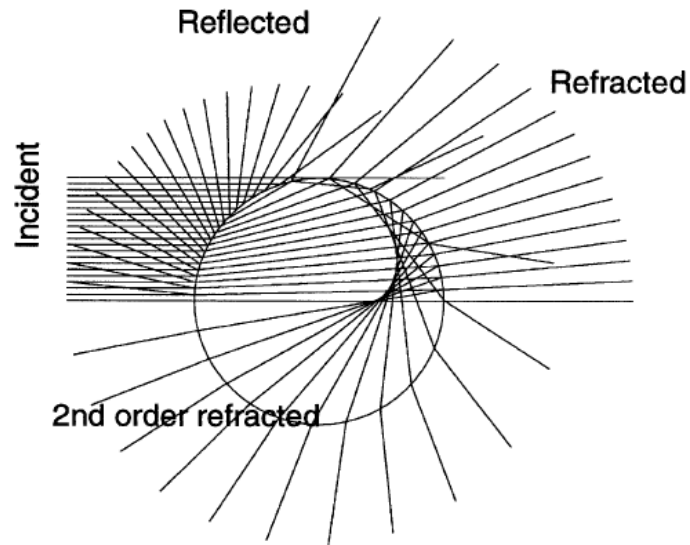


Figure 5.7 - The three different light scattering modes [9].

The direct surface reflection is prevailing for larger particles and hence the intensity can be considered proportional to the square of the particle diameter. By decreasing the particle size, the diffraction becomes significant and polarization of the incident light has strongly affect the light scattering. This is crucial for selecting the right configuration for positioning transmitting and receiving probes.

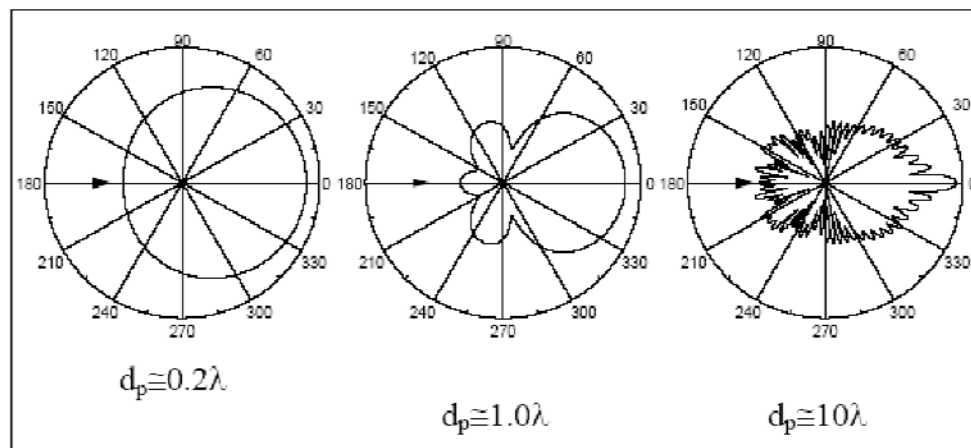


Figure 5.8 - Light scattered by spherical particles of different size (the intensity of light is shown in logarithmic scale).

When two coherent laser beams intersect, generate parallel planes of interference of light and shadow (Figure 5.9). These planes are known as interference fringes, and their

distance δ depends on the wavelength and the angle between the incident rays according to the relation

$$\delta = \frac{\lambda}{2 \sin(\theta/2)} \quad (5.5)$$

where λ is the laser wavelength and θ is the angle between the two beams.

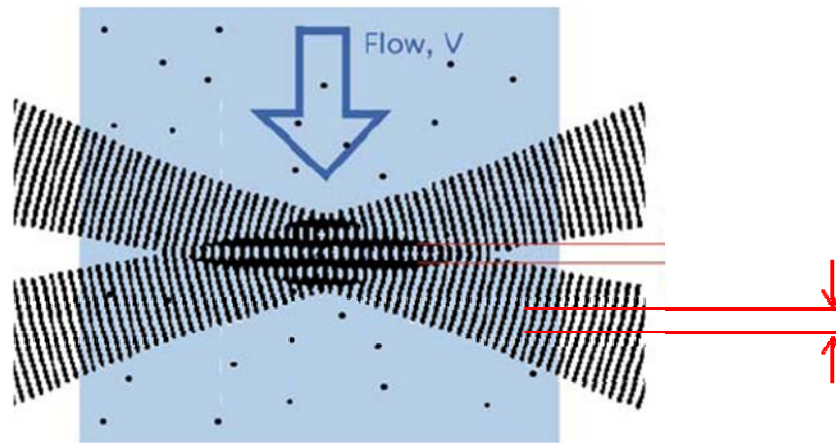


Figure 5.9 - Interference fringes due to the intersection of two coherent laser beams.

The fringes are perpendicular to the speed component of the particle crossing the measurement volume, and the refracted light intensity changes with a frequency proportional to the particle velocity:

$$f_d = V_a / \delta \quad (5.6)$$

replacing the formula of δ is obtained:

$$f_d = 2 \left(\frac{V_a}{\lambda} \right) \quad (5.7)$$

However, a small beam divergence α should be taken into account for a right estimation of δ .

If the two beams do not intersect in the area of the constriction, the wave front may be curved rather than flat, and thus the spacing of the fringes will not be constant but will depend on the position in the volume of measurement. Consequently, the measure of the Doppler frequency will be dependent also on the position of the particle and it will no longer be directly proportional to the speed. The resulted Doppler frequency is not able to deliver the speed direction. To solve this problem, frequency shift f_b , typically of 40 MHz, is added to one of the two beams through a Bragg cell.

Shifting the two beams, the photomultiplier output will give a variable signal, with a frequency $f_b + f_d$ if the particles follow the verse of the shifted beam towards the not shifted one; frequency $f_b - f_d$ will correspond to the reverse case.

This approach allows to get information about one component of the velocity. The same principle can be extended to two-dimensional and three-dimensional case. By introducing a second pair of beams is possible to estimate another speed component and the particles size through PDA.

PDA technique is an extension of LDV. The optical setup consists of a laser, a receiver probe, a transmitter probe and three photomultipliers connected to a processor. The particle sizing is performed by comparing the phase difference of the two light diffused signals that are collected by the two detectors.

More in detail, when a tracer particle diffuses light, the two detectors collect two Doppler signals whose phase difference depends on the size of the particle (figure 5.10). The corresponding phase difference can be estimated as:

$$\Phi_{12} = 2 \cdot \pi \cdot f \cdot \Delta t \quad (5.8)$$

where f is the light frequency and Δt is the delay between the waves reaching the detectors. By changing the particle size, a phase difference is obtained (figure 5.11).

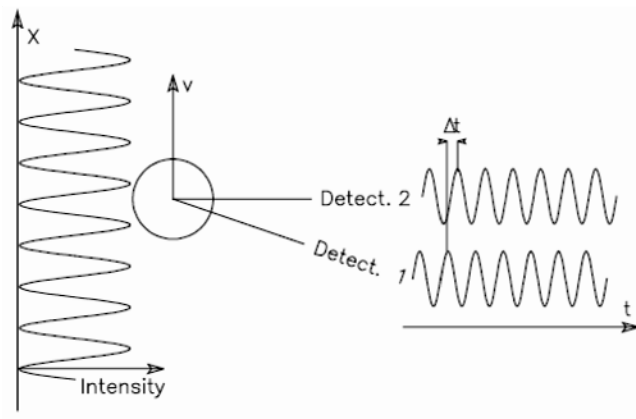


Figure 5.10 – Phase difference between two detectors at different angles.

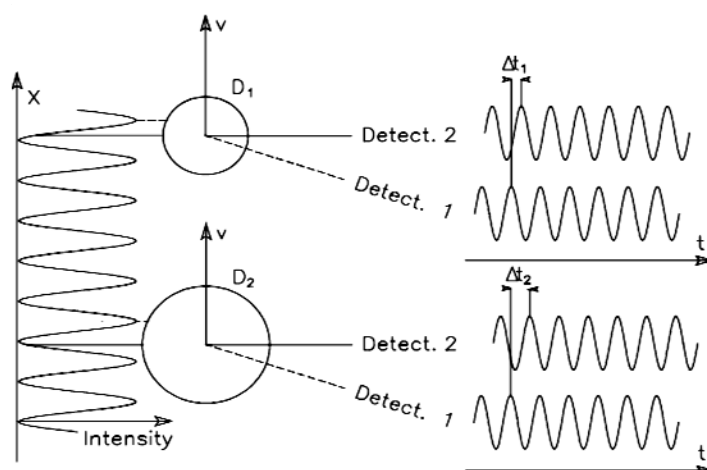


Figure 5.11 – Increasing phase difference with increasing particle diameter.

The phase can be expressed as:

$$\Phi_i = \alpha \cdot \beta_i \quad (5.9)$$

where the size parameter is:

$$\alpha = \pi \cdot D \cdot \frac{n_1}{\lambda} \quad (5.10)$$

in which n_1 is the refractive index of the medium in which the particle is located; λ is the wavelength of the laser in vacuum; D is the diameter.

β_i is a geometric factor depending on the nature of the diffused light and on the characteristic angles of the PDA system: θ , that is the intersection angle between the two incident beams; φ and ψ that define the position of the photomultiplier (Fig. 5.12). Looking at formulas 5.9 and 5.10 is evident the linear relationship between the phase and diameter. The system described allows to measure dimensions within a limited range because of the uncertainty of the so-called 2π . As shown in figure 5.13, if the diameter exceeds a certain value, two different diameters correspond to the same phase.

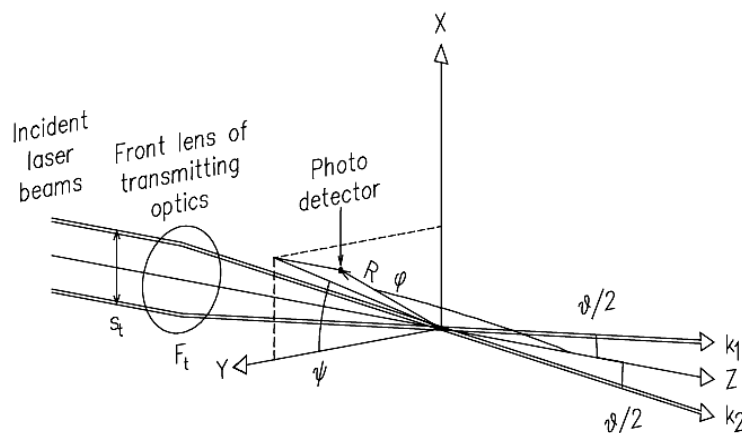


Figure 5.12 - Coordinates in the system.

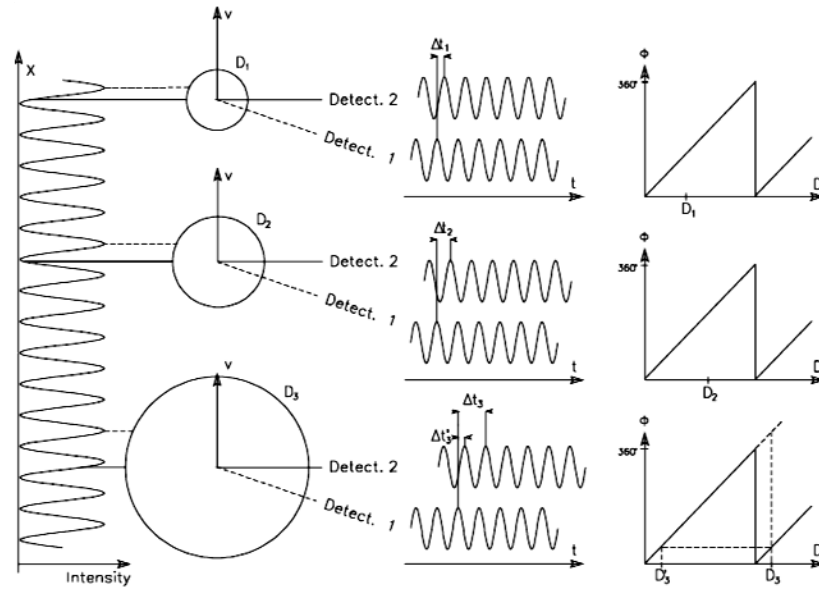


Figure 5.13 - The 2π ambiguity.

To extend the valid dimensional range, the PDA uses three photomultipliers to perform the following conditions:

- detectors are axial-symmetric;
- the most distant coupling determines the largest slope of the ratio diameter-phase, with a higher resolution and a smaller range of values (U_1 , U_2);
- U_1 - U_3 coupling defines the lowest slope.

The phase shift Φ_{12} , relative to the coupling U_1 - U_2 , determines four possible diameters (figure 5.14), while the value of Φ_{13} indicates which one of the values for D is the correct. In this way it is possible also to evaluate the spherical shape of the particles, since the phase difference of each coupling provides information about the curvature of the particle's surface. By comparing the curvature in two different positions of particle a sphericity ratio can be obtained.

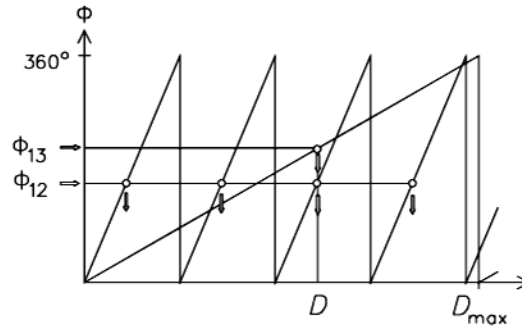


Figure 5.14 - Phase diagram of two pairs of photo-detectors at different separations.

5.2.2 Experimental methodologies

LDV and PDA techniques have been applied to characterize the spatial and temporal evolution of velocity and size of the fuel droplets composing the spray from a 6-hole nozzle for Direct Injection Spark Ignition (DISI) Engine. Technical specifications of injector have been detailed in Cap. 3. Measurements have been carried out in the optically accessible injection vessel at ambient temperature and pressure. A Cartesian coordinate system z-x has been defined: the origin, the vertical axis z and horizontal axis y have been set coincident with nozzle hole exit, the nozzle body axis and with a horizontal axis in the direction of the nozzle electrical connector, respectively.

The transmitting and receiving probes are placed on triaxial micrometric motion stages to obtain the correct positioning of the measurement volume and the focusing of the receivers with an accuracy of 1 μm . As for PIV, the measurements have been performed on a single jet (jet 4 of figure 4.10).

The high injection pressure induces a high spray density involving an increase of multi-scattering and reflection phenomena that limit the sampling rate, especially in the jet core. Therefore two different axes have been taken into

account for the measurements with Δz increment of 5 mm: the first axis coincident with the jet axis, the latter corresponding to the jet boundary profile. In fact, the reduced density in the boundary spray regions allows to increase the data rate even at small distances from the nozzle (Figure 5.15).

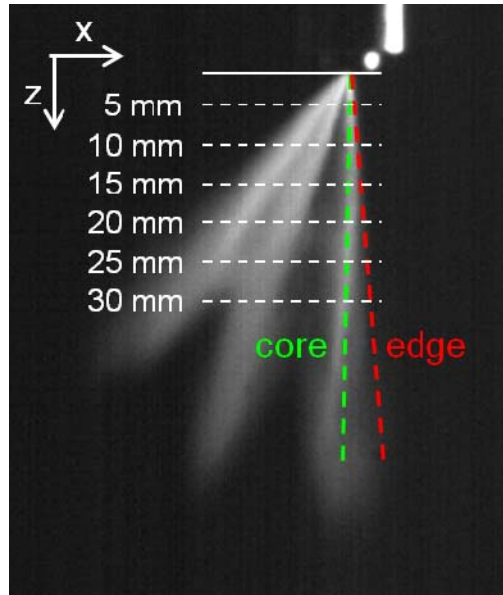


Figure 5.15 – PDA measurement grid.

The measurements have been carried out considering 300 injection events at two different injection pressures: 5 MPa and 10 MPa. The acquisition window has been set larger than the whole injection event and its start has been synchronized with the electronic start of the injection. This set-up has allowed to characterize the whole injection event: from the needle lift up to the closing of the nozzle hole. Depending on the injection time and the injection pressure, specific acquisition times have been used for the different injection strategies:

- 4000 μs for injection pressure of 10 MPa and injection time of 2917 μs ;
- 5000 μs for injection pressure of 5 MPa and injection time of 4000 μs .

The data post-processing has been performed through Labview NI (vers.2011) routine developed in IM to achieve a correct analysis of the PDA statistical distributions. The routine build the histogram of occurrence (number of repetitions in the k-th interval Δx , over N measurements) as function of droplets diameter and speed. Successively, the routine estimates the expected value (μ) and the variance (σ) of the Gaussian curve closest to experimental data distribution. The statistical analysis of the distribution has allowed to individuate the criteria for filtering the experimental data and reducing the false samples. Specifically, all the samples out of the Gaussian curve limits have been excluded (Figure 5.16) and variable substitution procedure has been applied in order to obtain a new distribution $f(z)$, characterized by a zero expected value and an unit variance.

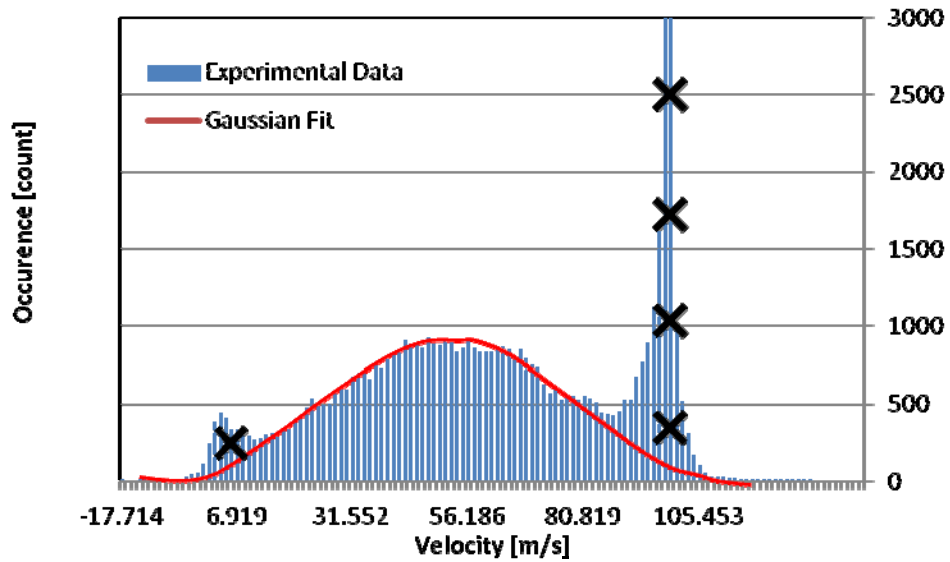


Figure 5.16– Fitting of Gaussian curve with droplets velocity distribution.

Hence, it has been possible to define a confidence interval. A statistical confidence level $z = 2$ has been set for the droplets velocity population with an acceptance of 95.45 % (Figure 5.17). A further filter has been applied on the

sampling rate, rejecting all the data with a sample number lower than the 5% of the maximum.

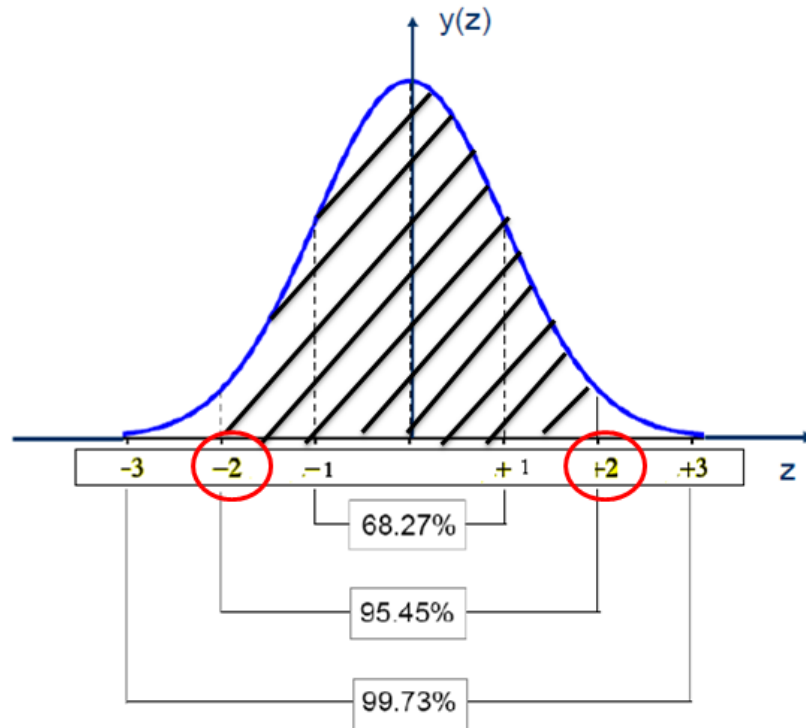


Figure 5.17– Confidence levels.

5.3 Operative conditions and results

As previously described, LDV and PDA measurements have been performed on two different axes: the first on the edge of the jet, the latter coincident with the jet axis (fig. 5.15). Figure 5.18 shows the temporal profiles of droplet mean velocity, measured along the jet edge. The red dashed line indicates the electrical end of injection, since, as aforementioned, the solenoid energizing time (ET) has been set at 4 ms and 2.9 ms at 5 and 10 MPa, respectively. Results have been obtained as the ensemble average over 300 acquisition cycles, with a time bin of 50 μ s. As shown in fig. 5.18(a-b), the first signal due to the presence of droplets has been detected for 10 MPa at about 250 μ s from

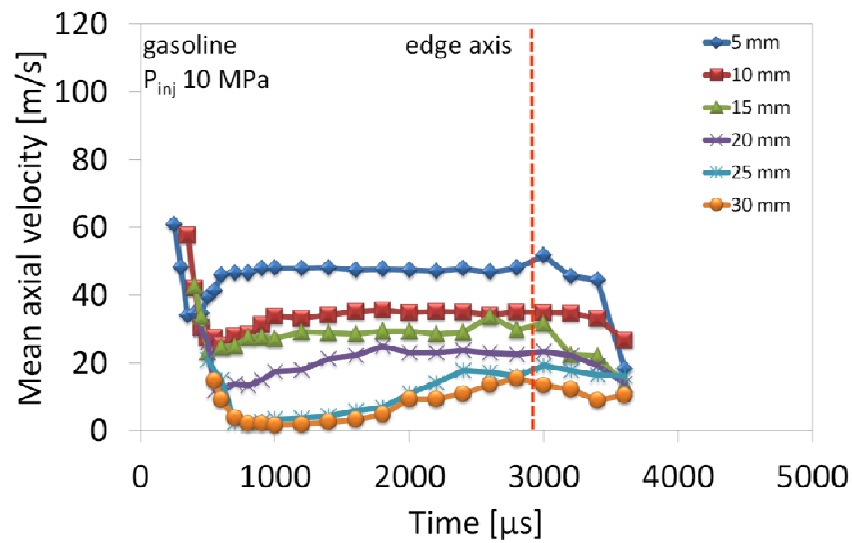
the electronic start of the injection and 50 μs after the effective start of the injection as measured by injection rate analysis and digital imaging. This has been due to the *time of flight* that is the interval of time required by droplets to reach the control volume.

As expected [10], the velocity profiles show a similar shape at all the investigated injection pressures. Three different curve sections can distinguished:

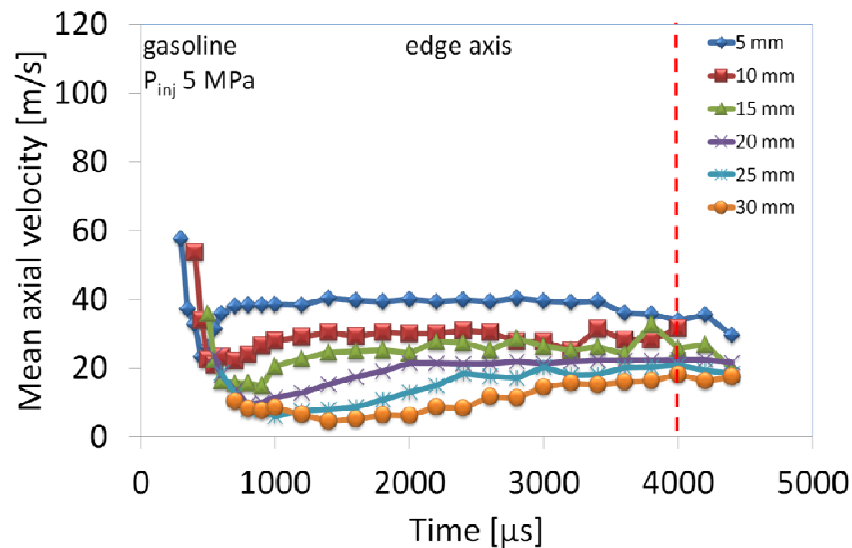
- Early stage (needle lift) corresponding to the transient stage of the injection start: this section is characterized by a rapid speed decrease ;
- Steady stage (needle completely lift): the speed is almost constant until the end of the injection;
- Late stage (nozzle closing), due to the end of the injection: a quick reduction of speed is detected.

The first droplets coming out from the nozzle, located on the jet tip, are the first to impact with the air and hence they quickly lose their quantity of motion. The succeeding droplets are affected by a “wake effect”; they are injected into the air which is following the first droplets motion, hence the braking effect of the air is lowered and the droplets penetrate longer before the break-up [11].

As expected, a velocity reduction is recorded at bigger distances from the nozzle. Moving far from the nozzle, the spray becomes less dense and more affected by the interaction with the air, the effect of the high injection pressure is considerably reduced. The break is occurred, the droplets break into smaller ones the momentum is drastically reduced.



(a)



(b)

Figure 5.18 – Temporal profiles of droplet mean axial velocity at 10 MPa (top) and 5 MPa (bottom) injection pressure along the jet edge.

As expected the minimum speed has been detected at 30 mm from the nozzle with a velocity reduction of about 90% with respect to the maximum value, if it compared to the position of 5 mm. At this distance the effect of injection pressure is negligible and the droplets are dragged by the air.

Figure 5.19 shows the effect of the injection pressure on the mean axial velocity. The data refer to the axial velocity averaged over the time corresponding to the steady stage of the injection. As expected [12], the pressure decrease induces a velocity reduction, due to the lowering of momentum flux. The maximum axial velocity of about 50 m/s is reached at the injection pressure of 10 MPa, for the first droplets injected and detected at 5 mm from the nozzle. As the distance from the nozzle increases, the break-up phenomena proceed with a reduction of velocity; the injection pressure effect is drastically reduced and the velocity gap between the two injection strategies becomes negligible.

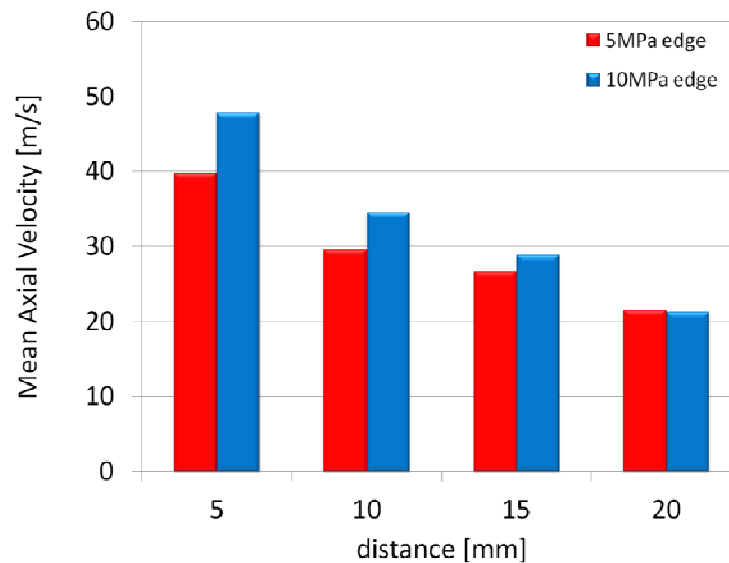
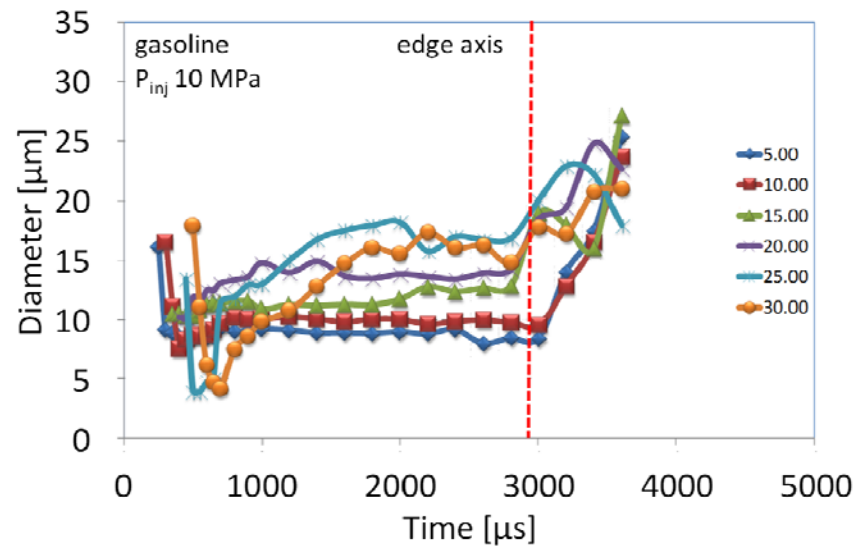
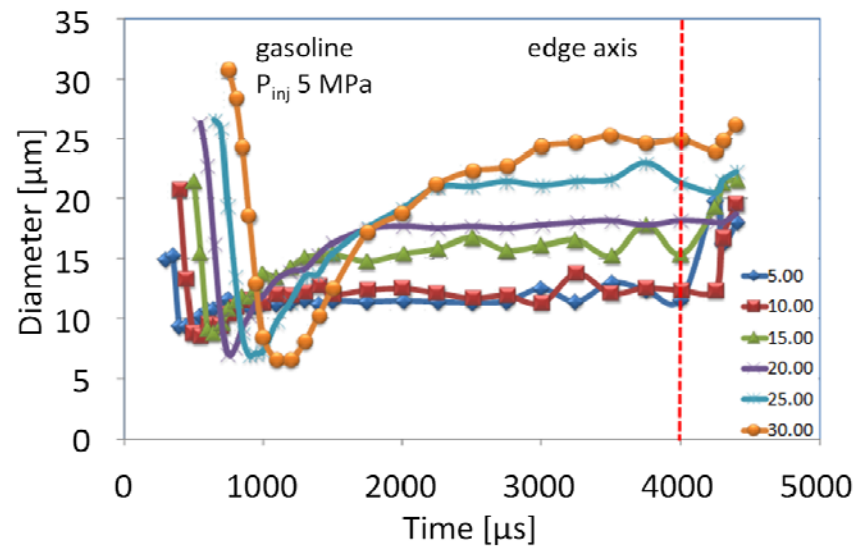


Figure 5.19 – Effect of injection pressure on the mean velocity along the edge axis.



(a)



(b)

Figure 5.20– Temporal profiles of droplet diameter at 10 MPa (top) and 5 MPa (bottom) injection pressure along the jet edge.

Figure 5.20 shows the temporal profiles of droplet size for gasoline fuel at 5 MPa and 10 MPa injection pressure, measured along the jet edge. An opposite tendency with respect to the speed profiles has been found for the droplets diameters: the droplets size increases by increasing the distance from the nozzle

[13]. As for the velocity profiles three different sections of the curve can be identified, depending on the injection stages.

At the start of injection the diameter values rapidly decrease up to a minimum. After, the droplets size shows an increasing trend up to a quasi-steady stage, with almost constant values until the end of the injection.

During the final transient stage, an increase of droplet diameters is recorded, after the closure of the nozzle.

By looking at results shown in figure 5.20 a), a more detailed analysis can be performed. At the needle lift, the droplets provide high diameters, about 15 μm at 5 mm distance, because the primary breakup is still happening. Then the values tend to a constant with a reduction of about 45% with respect to the maximum. Finally, the droplets detected during the last acquisition time, after the end of injection, reach larger size (about 25 μm at 10 MPa, 5 mm distance from the nozzle). This phenomenon is likely due to coalescence phenomena occurring when the needle falls, closing the nozzle, depriving the droplets of the pressure gradient force.

As for the speed, the effect of the injection pressure on the mean diameter averaged on the whole steady stage of the injection is shown in figure 5.21. An increase of the droplet size is recorded by increasing the distance from the nozzle.

As known by the literature [10, 14], an increase in injection pressure results in a better spray atomization because the interaction with surrounding air is enhanced. As an effect a droplets size decrease is measured. As the distance from the nozzle increases the difference reduces.

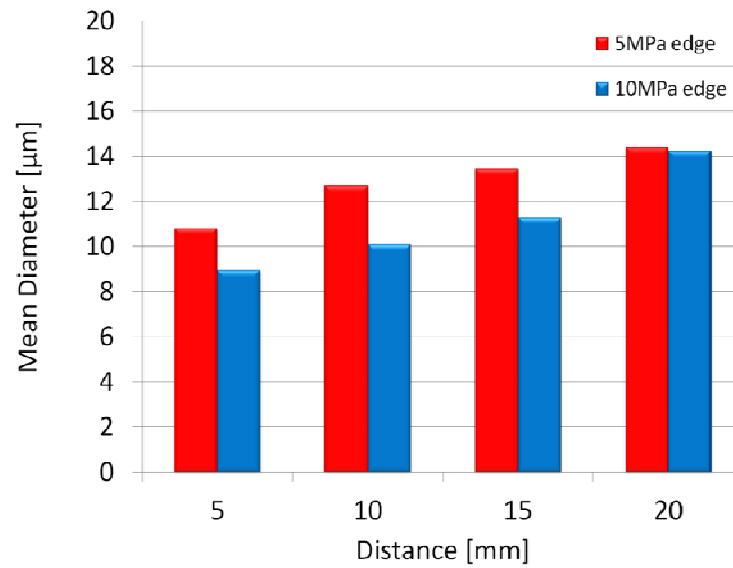
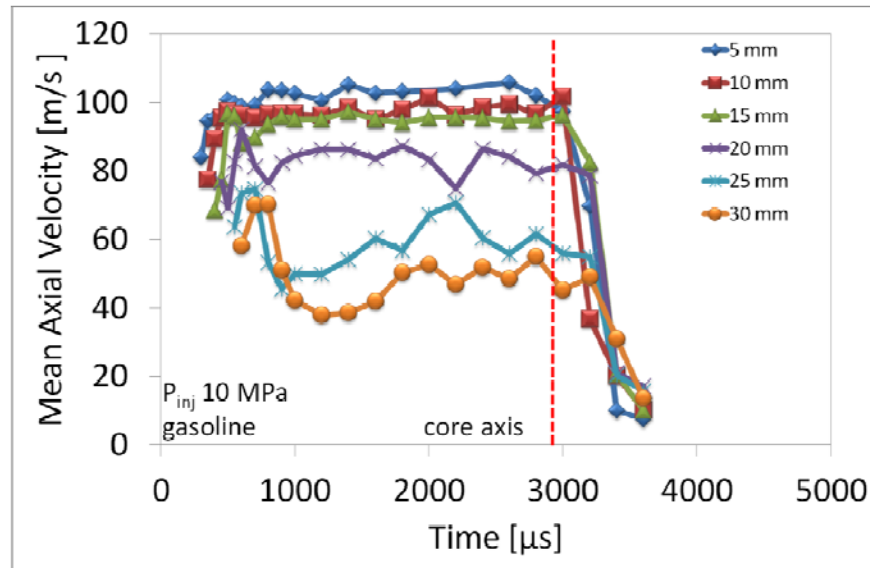


Figure 5.21 – Effect of injection pressure on the mean diameter along the edge axis.

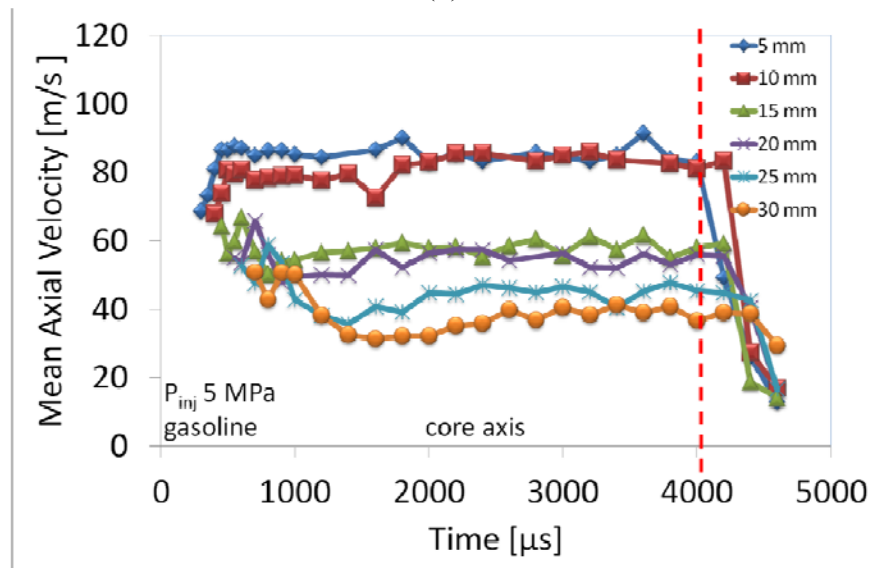
Figure 5.22 shows the temporal profiles of droplet mean velocity, measured along the jet axis at both investigated injection pressures. Although the droplets and velocity distributions along the axis exhibit similar trends to those of the edge profile, a significant velocity increase can be observed. This result is evident in Figure 5.23, comparing the mean velocity along the jet core axis and jet edge, at both injection pressures, estimated as the average over the time interval between 1000 μ s and 2000 μ s (quasi steady stage of the injection).

The droplets on the jet edge reduce drastically the axial velocity with a maximum value of about 48 m/s at 5 mm from the nozzle and 10 MPa of injection pressure, while the minimum is about 21.5 at 20 mm and 5 MPa. Axial velocities on the jet axis reach the highest value of 105 m/s at 5 mm from the nozzle and 10 MPa of injection pressure with a decreasing trend along the axis. The effect of the injection pressure on the droplets velocity along the jet core is

significant with a strong axial velocity reduction at the lower injection pressure and particularly at far locations from the nozzle.

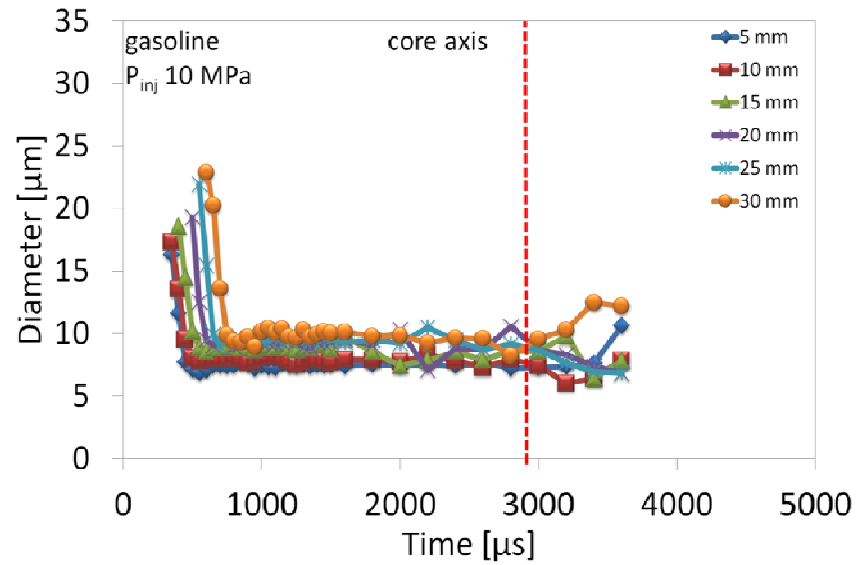


(a)

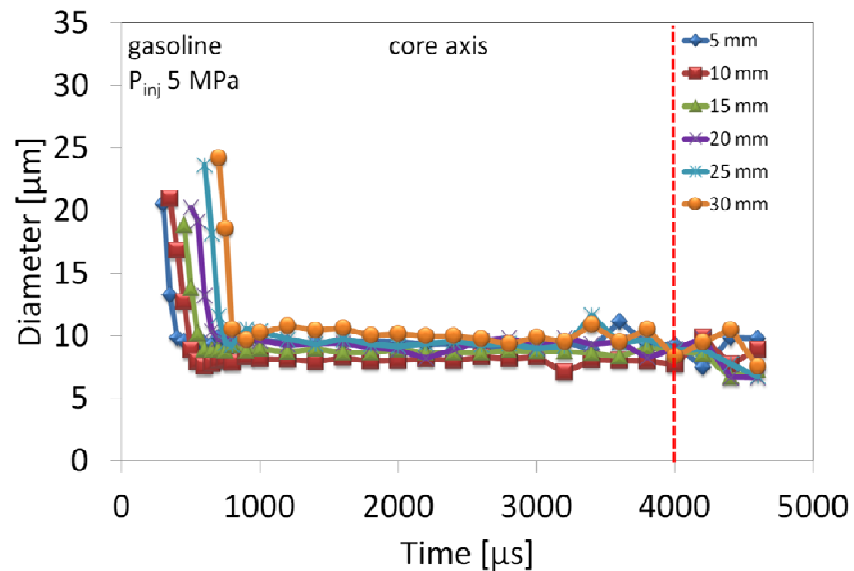


(b)

Figure 5.22 – Temporal profiles of droplet mean axial velocity at 10 MPa (top) and 5 MPa (bottom) injection pressure along the jet axis.



(a)



(b)

Figure 5.24 – Temporal profiles of droplet diameter at 10 MPa (top) and 5 MPa (bottom) injection pressure along the jet axis.

Slight effect of the injection pressure on the mean diameter is observed, while a slight increase is detected at longer distances from the nozzle. The only exception to this behavior is at 5 mm where the lower injection pressure provide larger size. This result might be due to an increase of break-up length at the lower injection pressures. By comparing the droplets mean diameter on the jet edge to those on the jet axis, the higher

atomization in the core jet results in lower droplets diameter. This difference is highlighted in the farther locations. The maximum difference in diameter is obtained at 20 mm, where 14.4 μm size is reached at 5 MPa on the edge and 9.2 μm on the core axis.

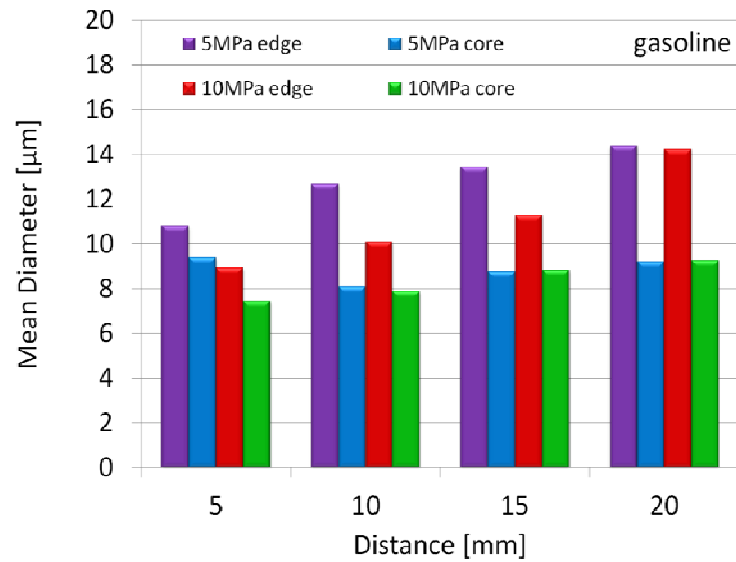


Figure 5.25 – Mean diameter vs distance from nozzle along the core and the edge axes.

REFERENCES

-
- [1] Wigley, G., Goodwin, M., Pitcher, G., & Blondel, D. (2004). Imaging and PDA analysis of a GDI spray in the near-nozzle region. *Experiments in fluids*, 36(4), 565-574. DOI 10.1007/s00348-003-0690-1.
- [2] Li, T., Nishida, K., & Hiroyasu, H. (2011). Droplet size distribution and evaporation characteristics of fuel spray by a swirl type atomizer. *Fuel*, 90(7), 2367-2376. DOI 10.1016/j.fuel.2011.03.011.
- [3] Lee, S., & Park, S. (2014). Experimental study on spray break-up and atomization processes from GDI injector using high injection pressure up to 30MPa. *International Journal of Heat and Fluid Flow*, 45, 14-22. DOI 10.1016/j.ijheatfluidflow.2013.11.005-
- [4] Zhang, S., & McMahon, W. (2012). Particulate emissions for LEV II light-duty gasoline direct injection vehicles (No. 2012-01-0442). SAE Technical Paper. DOI 10.4271/2012-01-0442.
- [5] Chen, L., Stone, R., & Richardson, D. (2012). A study of mixture preparation and PM emissions using a direct injection engine fuelled with stoichiometric gasoline/ethanol blends. *Fuel*, 96, 120-130. DOI 10.1016/j.fuel.2011.12.070.
- [6] Zigan, L., Shi, J. M., Krotow, I., Schmitz, I., Wensing, M., & Leipertz, A. (2013). Fuel property and fuel temperature effects on internal nozzle flow, atomization and cyclic spray fluctuations of a direct injection spark ignition–injector. *International Journal of Engine Research*, 1468087413482320. DOI 10.1177/1468087413482320.
- [7] Soid, S. N., & Zainal, Z. A. (2011). Spray and combustion characterization for internal combustion engines using optical measuring techniques–A review. *Energy*, 36(2), 724-741. DOI 10.1016/j.energy.2010.11.022
- [8] Van de Hulst HC. Light scattering by small particles. NewYork: Dover, 1981

-
- [9] BSA Flow Software Installation & User's guide
- [10] Li H. (2013) CFD modelling study of sprays and combustion of gasoline and DMF in direct injection gasoline engines. PhD thesis, University of Birmingham.
- [11] L. Allocca, S. Alfuso, L. Marchitto, G. Valentino, GDI Multi-Hole Injector: Particle Size and Velocity Distribution for Single and Jet-to-Jet Evolution Analysis, ICLASS 2009, 11th Triennial International Annual Conference on Liquid Atomization and Spray Systems, Vail, Colorado USA, July 2009
- [12] Marchitto, L., Merola, S., Tornatore, C., & Valentino, G. (2014). Experimental Study on the Spray Atomization of a Multi-hole Injector for Spark Ignition Engines Fuelled by Gasoline and n-Butanol (No. 2014-01-2743). SAE Technical Paper. DOI 10.4271/2014-01-2743.
- [13] Knorsch, T., Heldmann, M., Zigan, L., Wensing, M., & Leipertz, A. (2013). On the role of physiochemical properties on evaporation behavior of DISI biofuel sprays. *Experiments in fluids*, 54(6), 1-14. DOI 10.1007/s00348-013-1522-6.
- [14] Mitroglou N., Nouri M., Gavaises M., Arcoumanis C. (2006) Spray Characteristics of a Multi-hole Injector for Direct-Injection Gasoline Engines *International Journal of Engine Research* June 1, 2006 vol. 7 no. 3 255-270.

Chapter 6

X-ray tomography for GDI injection characterization

The importance of investigating the inner structure of high pressure sprays have been widely discussed in this dissertation: even if an increase on injection pressure allows to enhance the break-up of the liquid bulks, a full knowledge of atomization mechanisms is necessary for effectively taking advantage of the larger spray dispersion.

Experiments on the injection systems are generally performed through optical techniques based on the scattering of light sources ranging from UV to IR wavelength region ($\sim 180 - 900\text{nm}$) [1]. As shown in the previous chapters, the global morphology of the jet can be obtained through Mie scattering technique, while PIV, LDV and PDA can provide information about the spray flow field and droplets sizing. However, strong limitations concerning the inner structure of the spray occur due to the high fuel density reached close to the nozzle and in the core of the jet. In these zones, both light absorption and multiple scattering prevent to carry out measurements with acceptable signal to noise ratio, limiting them to less dense region on the spray boundaries [2-4].

Recently, Linne et al. [5] successfully applied a ballistic imaging to get high-resolution, single-shot images of the liquid core of a dense sprays featuring jet structure, morphology and droplet ruptures.

However, while conventional optical techniques can provide information about liquid and vapor phase structures, they cannot be useful for quantitative measurement of local fuel densities. This lack of data can be compensated through X-ray measurements. Thanks to the weak interaction of the X-radiation with the hydrocarbon chain of fuel due to their low atomic number, it can penetrate fuel jet structures and provide spatially-resolved information along the line of sight [6]. This approach is not completely new: first experiments of X-ray absorption by liquid sprays date back to the 80's. In 1984 Gomi and Hasegawa [7] estimated the mass distribution of liquid phase in a water/gaseous nitrogen spray by X-ray absorption method.

Recently, Synchrotron Radiation Source (SRS) based-absorption techniques have been applied to investigate high-dense regions of fuel sprays providing quantitative measurements of the fuel mass [8]. SRS are high-brilliant sources providing monochromatic and collimated radiation beams with pulsed structure at high frequency. Portable X-ray sources are rarely used with respect to SRS because of their lower energy, high divergence and structure continue in time [9].

Recent progresses in advanced optics for X-ray applications, like Polycapillary lenses, have allowed to collimate X-ray beams with a relatively high intensity enabling to acquire high contrast images [10-13].

The present chapter shows the results of a X-ray absorption tomography applied on the spray of a GDI 6-hole nozzle (sec. 3.1.1) by a desktop apparatus using a portable X-ray source coupled with a polycapillary semilens for studying the structure. Three-

dimensional computed tomography (3D CT) of GDI sprays have been realized performing accurate fuel mass density measurements in the region immediately downstream of the nozzle exit [14].

6.1 Experimental set-up

A X-Ray micro computed tomography set-up has been designed for investigating the inner structure of GDI (sec. 3.1.1.) sprays. The tomographic reconstruction of absorption signal has been used for quantitative measurements of the spray density. The experimental apparatus is reported in figure 6.1.

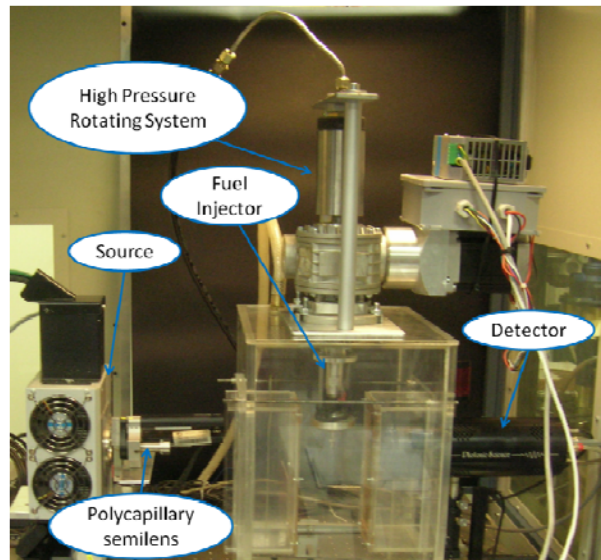


Figure 6.1 - X-Ray micro computed tomography set-up.

A X-ray tube (Oxford Apogee 5000), with spot size of about $50\ \mu\text{m}$ has been coupled with a polycapillary semilens providing a quasi-parallel beam, with a residual divergence of about $1.4\ \text{mrad}$ and a transmissivity of about 60%. It is about 60 mm long, the entrance and the exit diameters are 3 and 4 mm, respectively.

X-rays are generated when matter is irradiated by an electrons beam. Generally, a filament is heated to produce electrons that are then accelerated in vacuum by a high

electric field in the range 20-60 kV towards a metal anode target. The corresponding electric current is in the range 5-100 mA. A copper target has been set for generating the X-ray beam in this work. The signal emerging from the high pressure fuel spray has been collected through a Photonic Science CCD camera (FDI 1:1.61), with a sensitive area of $14 \times 10 \text{ mm}^2$ and $10.4 \times 10.4 \text{ }\mu\text{m}^2$ pixel size, with 12 bit image digitalization [15]. A pulse generator has been used for triggering both image acquisition and injection ensuring a correct synchronization.

Commercial gasoline has been used ($\rho \sim 720 \text{ kg/m}^3$) for the experiments. The gasoline is a mixture of different hydrocarbon chains; hence it is featured by a very low absorption coefficient in the X-ray range. For this reason a fuel additive containing Cerium (4% in volume) has been used as X-Ray absorption improver. Two different injection pressures have been tested: 5 MPa and 10 MPa at 4 Hz frequency in a Plexiglas vessel at atmospheric backpressure and ambient temperature. The injection duration was 4 ms. Two 25 μm Kapton windows, transparent to X-radiation, separate the injection vessel from the X-ray cabinet in order to avoid contamination from gasoline droplets and vapour exit. An exhaust blower prevents the fuel fog to fill the chamber and accumulate on the Kapton windows. The blower has operated at low velocity avoiding interfering with the spray plume propagation.

6.1.1 Polycapillary optics

Polycapillary half-lens has allowed to focus the X-ray beam with around 60% transmissivity. The polycapillary optics are X-ray optical systems working at grazing incidence. They take advantage of the phenomenon of total external reflection (TER): if a X-ray beam impacts on a surface with an incidence angle lower than the critical angle of TER θ_c , it is reflected with a reflection factor close to one [16]. Even if the possibility

of deflecting x-ray beams from a surface according the TER phenomenon was demonstrated in 1923 [17], the technical limits to produce high-precision optics working at grazing angles ($\theta \sim 10^{-3}$) did not allow to exploit the TER principle until recent years. Currently, polycapillary optics represent a robust X-ray optical instrument for shaping beams with high intensity transmissivity. They consist of thousands of micrometric diameter hollow glass tubes used to collect, focus, and redirect x-ray beams (figure 6.2).

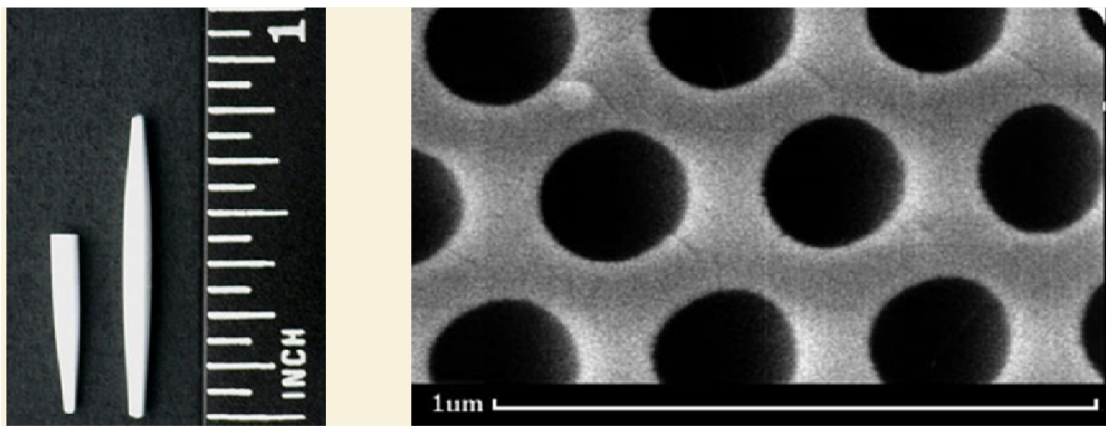


Figure 6.2 – Polycapillary lenses (left) and fiber inner section (right).

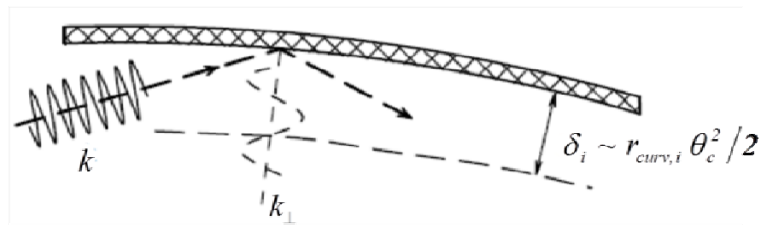


Figure 6.3 – Scheme of radiation reflection on a curved surface of a channel with a cross section diameter δ_i [18].

X rays impact on the inner surface of the single capillaries at grazing incidence and are guided until to the exit through a series of total external reflections. A high transmission efficiency is reached by keeping the incidence angle below the critical angle value.

The length and diameter of the channels is related to the critical angle by the following formula:

$$\delta_i \sim r_{curv,i} \theta_c^2 / 2 \quad (6.1)$$

where δ_i is the cross section diameter of the single channel i and $r_{curv,i}$ is the curvature radius. Hence for keeping the incidence angle below θ_c , the capillaries must have both small diameter and bending.

For this reason polycapillaries are preferred to single channel optics. The polycapillaries are obtained as an ensemble of thousands glass fibers with micrometric inner diameter (5 μm in this work).

6.1.2 High pressure rotating system

For realizing tomography, a relative rotation of the sample with respect to the acquisition system should be ensured with low eccentricity and high angular resolution. In order to avoid the displacement of the X-ray source with respect to the polycapillary optics, involving a transmissivity decay, a device for rotating the injector around its own axis has been designed in Istituto Motori [19] (figure 6.4). The system allows a control of the trip on a rotation $360^\circ - 0.1^\circ$ precision step, and working at pressure up to 20 MPa.

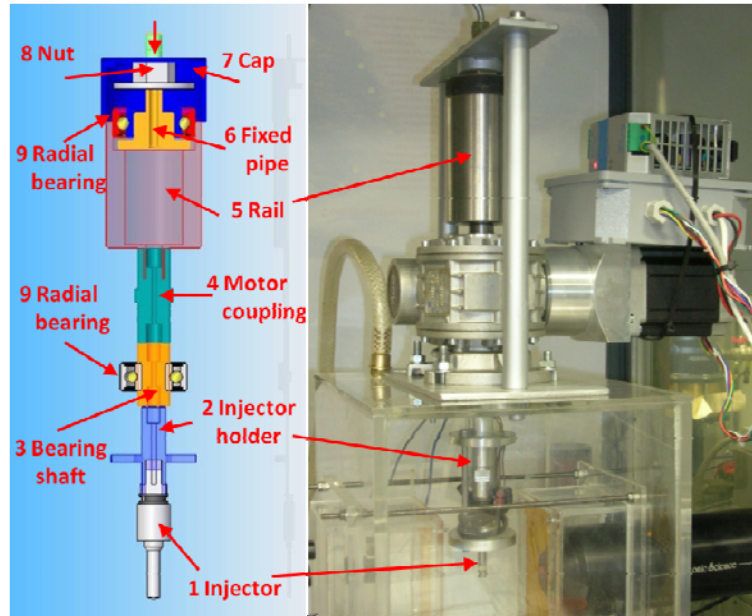


Figure 6.4 - High-pressure rotating system: schematic sketch (left) and picture (right).

A hollow shaft links the GDI injector (part 1 in figure 6.4) to a high pressure fuel tank working as rail (5). The shaft is composed of three parts: an injector holder (2), a chamber coupling through a radial bearing (3), shaped to be housed on the speed reducer shaft (4) coupled with a stepper motor. All the parts are connected by male-female threads and O-ring gaskets. The reservoir (5) works as high pressure rail accumulator to avoid pressure fluctuations during the injection phase.

The relative motion between the rotating fuel accumulator and the fixed part of the fuel pipe has been achieved through a radial bearing (9); the outer ring of bearing has been mounted to rotate together to the inner part of the rail, while the inner ring of the bearing is fixed and coupled with the fixed pipe (6). The high pressure fuel in the tank forces the pipe against the inner part of the bearing. An O-ring gasket ensures the sealing of the system at high pressure. A cap (7) is screwed on the rotating rail to fix it to the outer ring, while the nut (8) together with a washer connects mechanically the pipe (6) with the inner bearing wheel. The rotation of the system is induced by a high-

torque stepper motor controlled in direction, total angle and angular step by Arduino Uno Microprocessor. A LabView code, developed by XLab Frascati of INFN LNF, allows controlling the synchronization among injection system, CCD detector and stepper motor.

6.2 Data acquisition and post-processing

Even if the high transmissivity of polycapillary lenses allow to save the 60 % of beam flux, it is not high enough for performing time resolved measurements of fuel sprays due to the low X-ray absorption of gasoline. For this reason an acquisition time of 3 ms has been set about equal to the quasi-steady stage of injection, lasting 4 ms. The start of acquisition has been shifted 500 μ s after the start of injection, while the end has been advanced 500 μ s before the end of the injection. Thus the signal acquisition occurs during a constant injection rate stage, when the needle is completely lifted.

A series of 100 images per 1° angular rotation has been collected for the full 360° rotation, both for the injection event and the background. Hence, each acquisition is the result of the average over 100 injection events. The background acquisition is performed just after the sampling to take into account the effects of the fuel deposits on the beam profile acquisitions. This procedure allows a further reduction of signal noise.

Before the 3D reconstruction, the images have been processed by means of a code in Matlab structure (figure 6.5).

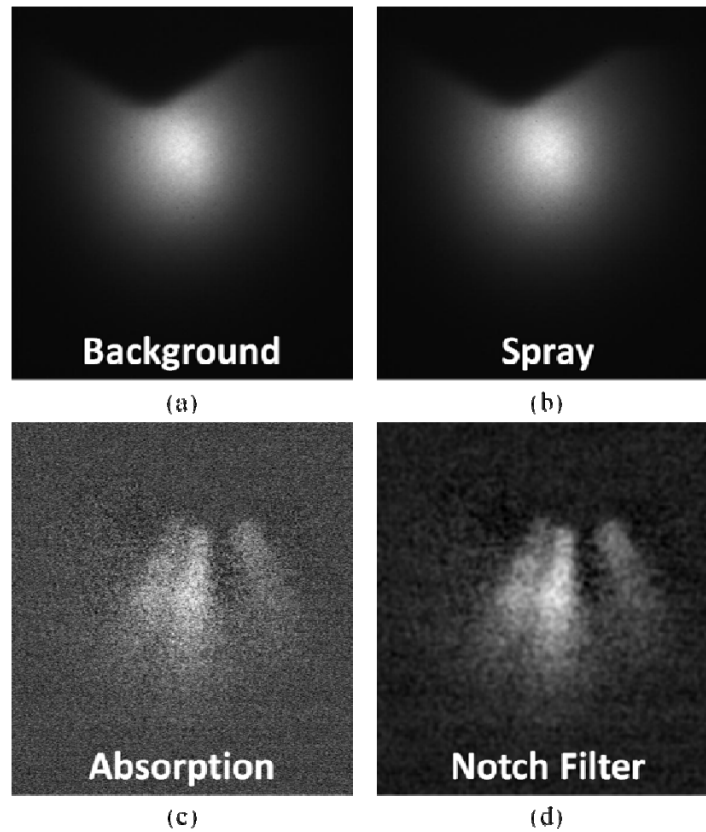


Figure 6.5 – Image post processing sequence: background (a), spray (b), absorption (c) and filtered absorption signal (d).

Firstly, a contrast enhance function has been applied for fully taking advantage of the whole bit depth. After, the absorption (figure 6.5 c) has been obtained as the ratio between the spray signal (b), corresponding to the transmitted X-ray intensity profile I , and background (a), which represents the incident X-ray beam intensity I_0 .

The absorption images are processed by means of an image processing software, Octopus, in order to obtain the tomographic reconstruction [20].

The code converts the absorption images (vertical projections) into sinograms by Fourier transform as a function of both rotation angle θ and distance along the projection direction. Finally, the sinograms are transformed into horizontal cross sections or slices by applying an inverse Fourier transform.

The slices are assembled through Amira by Visualize Imaging [21] for image rendering (figure 6.6) in order to investigate the inner structure of the sprays.

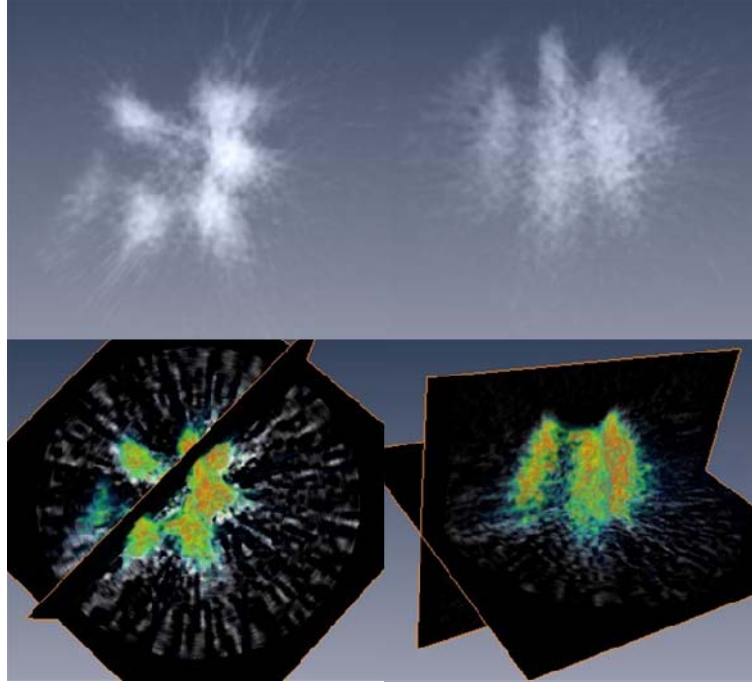


Figure 6.6 – 3D reconstruction of the six hole GDI spray (top) and their pseudocolors footprints along two orthogonal planes (bottom).

A Matlab code has been developed for quantitative analysis of the data in order to estimate the spray density distribution. A 3D map of the absorption has been obtained by merging the slices into a 3D matrix. The absorption is related to the sample mass crossed by the beam M by the formula [22]:

$$\frac{I}{I_0} = e^{-\mu_M M} \quad (6.2)$$

where μ_M is the mass absorption coefficient. Considering the single cross section, M represents the fuel mass m related to the spray cross section area A :

$$M = \frac{m \text{ [kg]}}{A \text{ [m}^2\text{]}} \quad (6.3)$$

On the other hand, Lambert Beer law can be written as:

$$\frac{I}{I_0} = e^{-\mu_l \rho l} \quad (6.4)$$

where μ_l is the linear absorption coefficient or attenuation coefficient and l is the crossed spray length. The density profile can be obtained if the absorption coefficients are revealed by comparing Eqs. (6.3) and (6.4) as:

$$\rho(x, y) = \frac{-\log \frac{I}{I_0}}{\mu_l l(x, y)} \quad (6.5)$$

As known, it is quite difficult to get quantitative measurements by means of a desktop X-ray source due to the polychromaticity of its beam because of strong photon energy dependence of the attenuation coefficient μ_l . The attenuation coefficient has been evaluated by an experimental calibration [23-24] and compared with results from literature for five samples of different known thicknesses [25]. The attenuation coefficient is a function of material related to its empirical formula. The commercial gasoline is a mixture of several hydrocarbons with variable concentration with common chemical formula C_8H_{18} . The following formula has been used for the estimation of linear absorption coefficient: $C_{418}H_{942}Ce$, which is actually the mixture of gasoline and Eolys, used to increase its absorption ability.

The results are reported in fig. 6.7. A slight fluctuation can be noted by varying the thickness; however, the theoretical value, $0.55 \text{ m}^2/\text{kg}$, is in the error bars range.

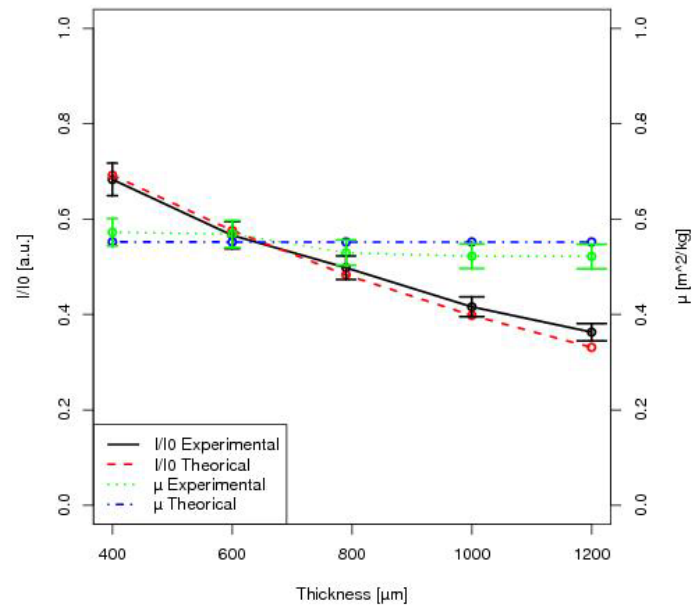


Figure 6.7 –: Radiation absorption curve (left axis) and linear absorption coefficient as function of sample thickness (right axis).

6.3 Results

A high accuracy tomographic reconstruction needs a high signal-to-noise ratio (SNR). With the aim to keep noise below an acceptable threshold, a high number of acquisitions for each projection and a high angular resolution are required. As discussed in the previous section 100 images have been acquired for each angular position and the average signal has been considered. A complete rotation of the injector over 360° around its axis has been obtained, with an angular step of 1° . The region of investigation has been limited to a 3.8 mm diameter circular area due to the small beam spot size. Figure 6.8 shows a Mie scattering acquisition at 300 μs after the SOI (left), compared with the corresponding X-ray absorption signal (right). The X-ray ROI has been outlined with a red square. The region immediately downstream the nozzle has been investigated for providing useful information about the atomization process which takes place in this area, where conventional optical diagnostic is prevented.

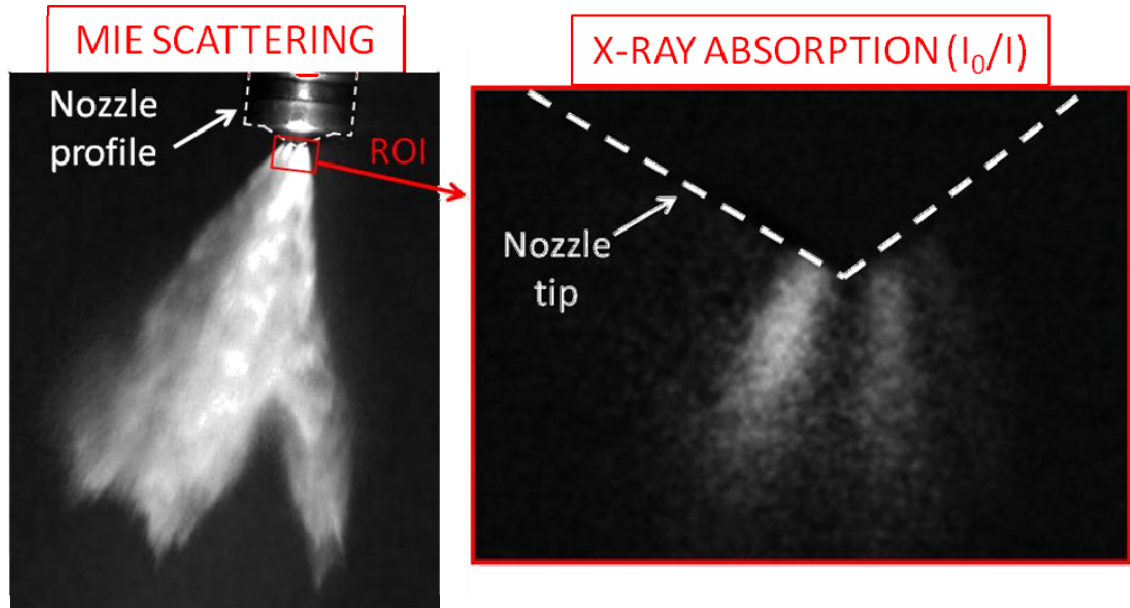


Figure 6.8 - Mie scattering acquisition at 10 MPa and 300 μ s after SOI (left) and X-ray absorption image (right).

Figure 6.9 represents the tomographic reconstruction of the six hole GDI spray at 5 MPa injection pressure; pictures referring both to the front and the lateral side views are shown. The footprint of each jet composing the spray is well resolved at the top side view of the figure 6.9. Lateral views allow a clear distinction among the different propagating jets. A large number of spots is observed around the spray, indicating the presence of parcels leaving the jets mixed to background noise. It is not possible to consider signals from isolated droplets or clusters because the image refer to average over 100 injections, hence time-resolved measurements are prevented.

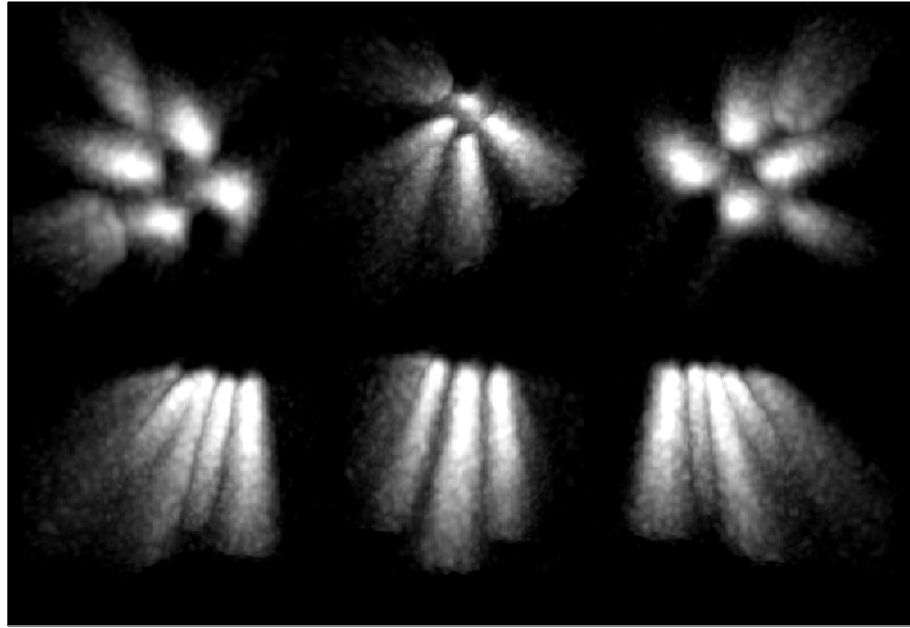


Figure 6.9 - Tomographic reconstruction of the six hole GDI spray: front (top) and lateral side views (bottom) at 5 MPa injection pressure.

The data used for the tomographic reconstructions have been further processed for providing quantitative measurements of the spray densities. The density of the sample has been obtained by the local absorption of the radiation I/I_0 , using the Lambert-Beer law. X-ray tomography is the only technique allowing to perform these measurements in the region immediately downstream the nozzle exit due to the local high densities and the starting of the liquid break-up that extinguish any visible light used to investigate. The spray density is an effective method for measuring the air to fuel ratio.

Fig. 6.10 reports the fuel density distribution in a plane orthogonal to the axis of the jet 4 (figure 4.10) at two injection pressures: 5.0 MPa (left) and 10.0 MPa (right). As discussed in the section 4.3.2, only the jet 4 propagates independent from the others and it has been set as reference for the quantitative measurements. Furthermore, the plane along the jet 4, crossing partially the 5 and 6, has been chosen in order to detect possible interaction among the jets. Considering the CCD spatial resolution ($16.67 \mu\text{m}/\text{pixel}$)

[26]), the data corresponding to distances lower than 150 μm from the nozzle have not been considered for quantitative measurements due to the low cross length through the jet.

The density profiles for all the jets and at both injection pressures show a maximum along the axis immediately at the exit of the nozzle. Maximum values of 146.5 and 150.5 kg/m^3 have been measured at 5.0 and 10.0 MPa, respectively. A fast intensity decrease occurs moving towards the radial zone. The effect of the injection pressure on the densities along the spray is not significant even if small differences appear concerning their maximum values. This is due to the limited region of interest taken into account, corresponding to 2 mm downstream the nozzle. At 10.0 MPa the momentum flux is preserved for a longer distance in both radial and axial direction and the density loss along the axis is delayed if compared with 5.0 MPa injection pressure.

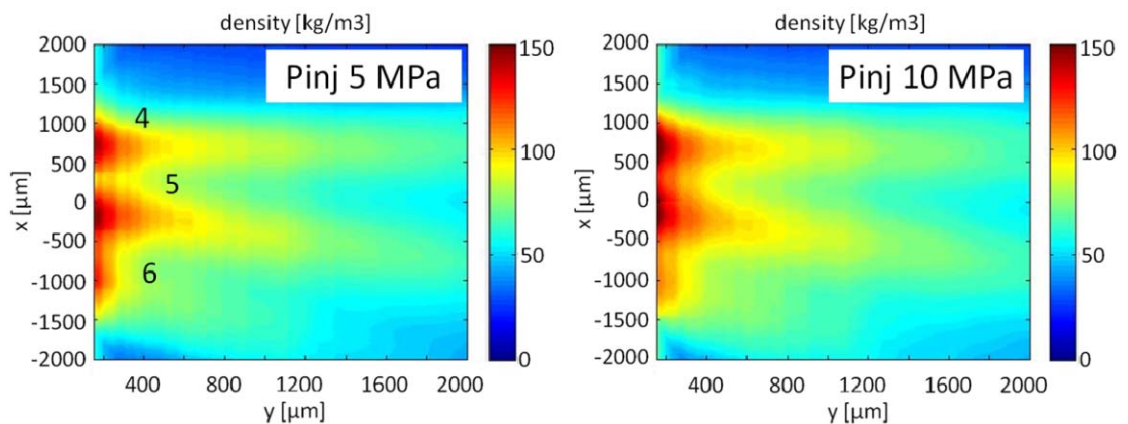


Figure 6.10 - Jet longitudinal plane distribution of fuel density.

For further investigations of the injection pressure effect, the 2D cross section distributions of X-ray absorption and fuel density for the jet 4 at 1500 μm distance from the nozzle have been shown in figure 6.11.

Looking at the effect of the injection pressure on the density, the jet shows a higher density peak at 10.0 MPa, reaching about 70 kg/m^3 . Moreover the density profile

appears flat, with a low eccentricity: as expected the higher momentum flux induced by the larger pressure reduces the influence of the surrounding air on the jets in the immediate region at the exit of the nozzle.

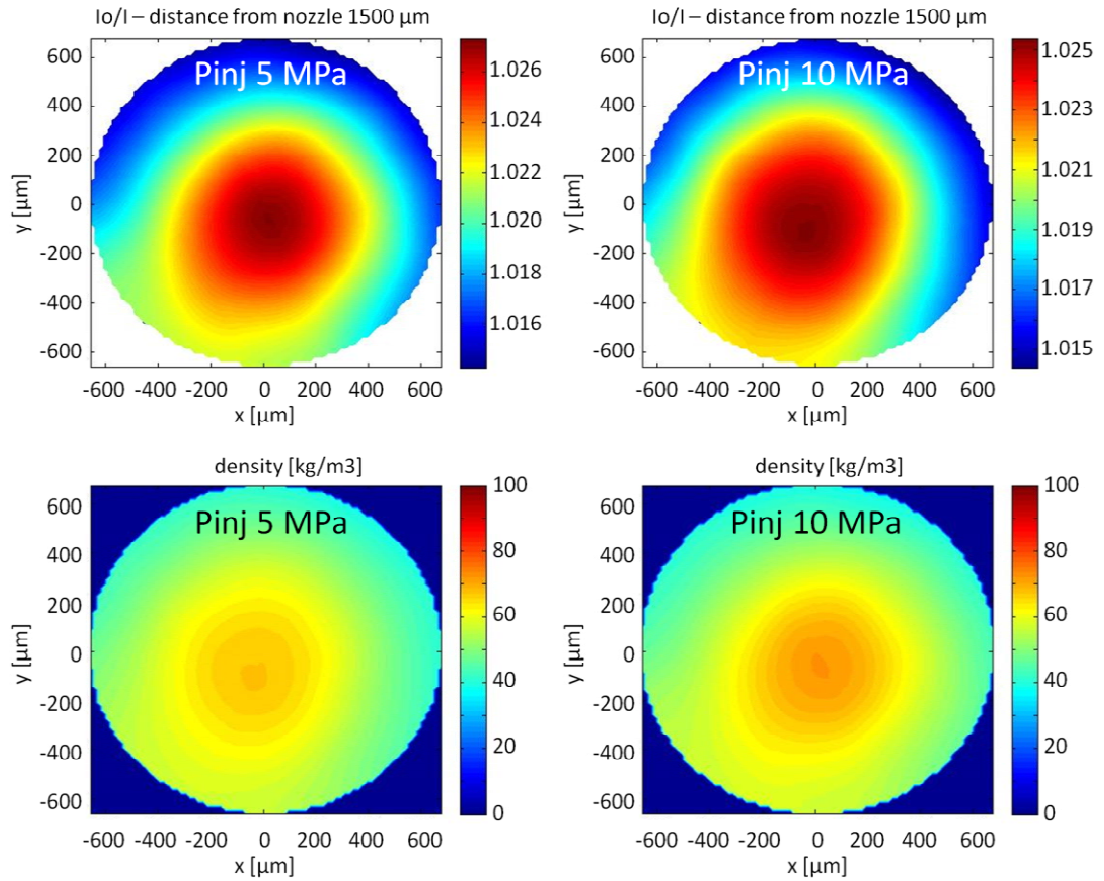


Figure 6.11 - 2D cross section distribution of X-ray absorption (top) and fuel density (bottom) for the jet 4, at 1500 μm from the nozzle.

REFERENCES

- [1] M. Linne, Imaging in the optically dense regions of a spray: a review of developing techniques, *Progress in Energy and Combustion Science*, 2013, 39: 403-440.
- [2] P.G. Aleiferis, Z.R. van Romunde, An analysis of spray development with iso-octane, n-pentane, gasoline, ethanol and n-butanol from a multi-hole injector under hot fuel conditions, *Fuel*, 2013, 105: 143–168.
- [3] L. Allocca, S. Alfuso, L. Marchitto, G. Valentino, GDI Multi-Hole Injector: Particle Size and Velocity Distribution for Single and Jet-to-Jet Evolution Analysis, *ICLASS 2009*.
- [4] Marchitto, L., Merola, S., Tornatore, C., & Valentino, G. (2014). Experimental Study on the Spray Atomization of a Multi-hole Injector for Spark Ignition Engines Fuelled by Gasoline and n-Butanol (No. 2014-01-2743). SAE Technical Paper. DOI 10.4271/2014-01-2743
- [5] M.A. Linne, M. Paciaroni, E. Berrocal, D. Sedarsky, Ballistic imaging of liquid breakup processes in dense sprays, *Proceedings of the Combustion Institute*, 2009, 32: 2147–2161.
- [6] B.R. Halls, C. Radke, T.J. Heindel, W.F. Lohry, S. Zhang, A.L. Kastengren, T.R. Meyer, Evaluation of advanced diagnostics for visualization of dense spray breakup processes. Central States Section of the Combustion Institute Spring Technical Meeting 2012: Combustion Fundamentals and Applications.
- [7] H. Gomi, K. I. Hasegawa, Measurement of the liquid phase mass in gas-liquid sprays by X-ray attenuation, *International journal of multiphase flow*, 1984, 10(6): 653-661.

-
- [8] K.S. Im, S. K. Cheong, C. F. Powell, M.D. Lai, J. Wang, Unraveling the geometry dependence of in-nozzle cavitation in high-pressure injectors, 2013, Scientific reports, 3.
- [9] A. C. Kak, M. Slaney, Principles of computerized tomographic imaging, 2001, Society for Industrial and Applied Mathematics.
- [10] D. Hampai, S.B. Dabagov, G. Cappuccio, A. Longoni, T. Frizzi, G. Cibin, Charged and neutral particles channeling phenomena, Channeling, 2008, World Scientific, S.B. Dabagov, L. Palumbo, Eds.: 775-785.
- [11] S. B. Dabagov, Channeling of neutral particles in micro- and nanocapillaries, Physics – Uspekhi, 2003, 46(10): 1053-1075.
- [12] C. A. MacDonald, Focusing polycapillary optics and their applications, X-Ray Optics and Instrumentation, 2010, 867049.
- [13] M.A. Kumakhov, F. F. Komarov, Physics Reports, 1990, 191-5: 289-350.
- [14] Marchitto, L., Hampai, D., Dabagov, S. B., Allocca, L., Alfuso, S., Polese, C., & Liedl, A. (2015). GDI spray structure analysis by polycapillary X-ray μ -tomography. International Journal of Multiphase Flow, 70, 15-21.
DOI <http://dx.doi.org/10.1016/j.ijmultiphaseflow.2014.11.015>
- [15] <http://www.photonic-science.com/products/XRAY-cameras-detectors.html>
- [16] Dabagov, S. B. (2003). Wave theory of x-ray scattering in capillary structures. X-Ray Spectrometry, 32(3), 179-185. DOI DOI: 10.1002/xrs.593
- [17] Compton, A. H. (1923). CXVII. The total reflection of X-rays. The London, Edinburgh, and Dublin Philosophical Magazine and Journal of Science, 45(270), 1121-1131. DOI 10.1080/14786442308634208

-
- [18] Dabagov, S. B. (2003). Channeling of neutral particles in micro-and nanocapillaries. *Physics-Uspekhi*, 46(10), 1053.
DOI 10.1070/PU2003v046n10ABEH001639
- [19] Allocca, L., Dabagov, S., Hampai, D., Marchitto, L., & Alfuso, S. (2013). *Tomography of a GDI Spray by PolyCO Based X-Ray Technique* (No. 2013-24-0040). SAE Technical Paper. DOI 10.4271/2013-24-0040
- [20] <http://www.insidematters.eu/en/software/octopus>
- [21] <http://www.fei.com/software/amira-3d-for-life-sciences/>
- [22] Attwood, D. (1999). *Soft x-rays and extreme ultraviolet radiation: principles and applications*. Cambridge university press. ISBN 9780521029971
- [23] Linne, M. (2012). Analysis of X-ray radiography in atomizing sprays. *Experiments in fluids*, 53(3), 655-671. DOI 10.1007/s00348-012-1312-6
- [24] Liu, X., Im, K. S., Wang, Y., Wang, J., Tate, M. W., Ercan, A., ... & Gruner, S. M. (2009). Four dimensional visualization of highly transient fuel sprays by microsecond quantitative x-ray tomography. *Applied Physics Letters*, 94(8), 084101.
<http://dx.doi.org/10.1063/1.3048563>
- [25] B.L. Henke, E.M. Gullikson, and J.C. Davis. X-ray interactions: photoabsorption, scattering, transmission, and reflection at E=50-30000 eV, Z=1-92, 1993, *Atomic Data and Nuclear Data Tables* Vol. 54 (2): 181-342.
- [26] Hampai, D., Marchitto, L., Dabagov, S. B., Allocca, L., Alfuso, S., & Innocenti, L. (2013). Desktop X-ray tomography for low contrast samples. *Nuclear Instruments and Methods in Physics Research Section B: Beam Interactions with Materials and Atoms*, 309, 264-267.

Chapter 7

GDI engine: combustion process investigation

Direct-Injection (DI) in Spark-Ignition (SI) engines, coupled with downsizing, variable valve timing and turbocharging, represents the most suitable technology to improve fuel economy and reduce exhaust emissions in the automotive field [1-5].

GDI engines meet the requirements of pollutant emission regulations and fuel consumption reduction, with market demand of performance, driveability and cost. The advantages of Direct-Injection over Port fuel Injection (PFI) have been widely demonstrated in terms of fuel economy, transient response, air-fuel ratio control and reduced emissions [6-10].

However, the combustion process in the engine depends on several complex phenomena and a complete understanding of them is far to be reached. Specifically, intake air charge motion, spray atomization and air-fuel mixture formation represent the key points for combustion processes development and for this reason they need to be deeply investigated for reaching an effective DISI engine optimization [6-8, 11-12].

Optical diagnostics, as digital imaging, chemiluminescence, particle image velocimetry (PIV), laser induced fluorescence (LIF), etc., can provide details and fundamental information for characterizing the phenomena that take place in a DISI engine [13-19].

The fuel spray development and its interaction with the surrounding air and the influence of injection parameters on the break-process have been deeply analysed in the previous chapters, allowing to determine an optimum injection strategy for the reference optically accessible engine.

This chapter presents the results of an optical analysis of combustion process in a DISI engine through high resolution UV-visible flame imaging and natural emission spectroscopy. Optical data have been correlated with thermodynamic analysis and exhaust emission measurements.

7.1 Experimental set-up

7.1.1 Optically accessible engine

Combined thermodynamic and optical measurements have been performed on a single cylinder optically accessible SI engine (Figure 7.1). The engine has been equipped with four-valve pent-roof head with centrally located spark plug of a commercial FIAT FIRE 1.4 l engine. The combustion chamber is wall-guided with the injector placed on the side between the two intake valves.

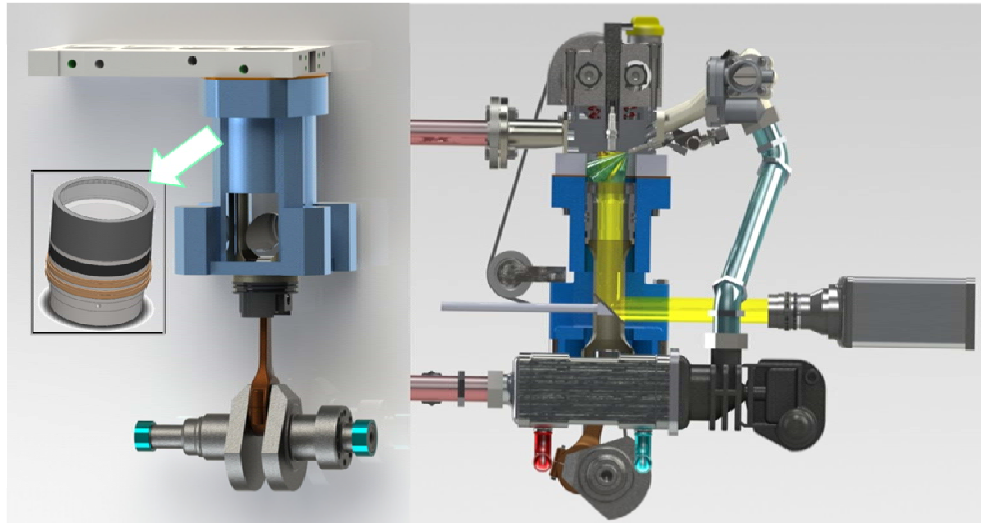


Figure 7.1 - Optically accessible GDI engine [20].

The main engine characteristics are provided in table 7.1.

Table 7.1 - Engine characteristics

Displacement volume	399 cm ³
Stroke	81.3 mm
Bore	79 mm
Connecting rod	143 mm
Compression ratio	10:1
Number of valves	4
Optical access diameter	68.5 mm
Opening exhaust valves	153 CAD ATDC
Closing exhaust valves	360 CAD ATDC
Opening intake valves	357 CAD ATDC
Closing intake valves	144 CAD BTDC

Optical accessibility has been ensured by an 18 mm-thick fused-silica window fixed on the piston crown featuring a Bowditch design (Figure 7.2), with a 45 degree UV-enhanced mirror fitted within the hollow piston. The piston was realized in Silafont-92

Aluminium alloy (AlSi18CuNiMg). Slotted graphite piston rings provide oil-less lubrication with uninterrupted bronze-Teflon rings used for sealing.

A dynamometer (230 Nm maximum torque; 49.7kW power) has been used to motor the engine. The engine speed has been set by regulating the operation of the electrical motor with a feedback control loop capable of switching between motor generator regimes. The engine control and synchronization of signal sources and measurement systems (e.g. optical detector, in-cylinder pressure sensor, etc.) have been performed through the crank angle encoder and ETU.

The crank angle encoder generates TTL pulses with adjustable resolution. This system contains a precision marker disk with a trigger and 760 angle marks, which are scanned by a transmission photoelectric cell. The angle mark resolution is 0.2 crank angle degree.

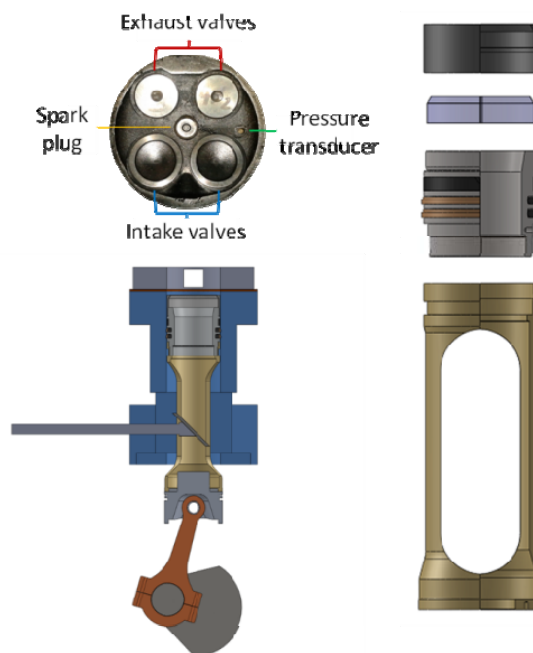


Figure 7.2 – Sketch of the optically accessible single cylinder with combustion chamber bottom field of view and details of the Bowditch piston.

The engine has been equipped with a GDI injection system (sec 3.1.1) controlled through a programmable electronic control unit. A Labview code has been used for managing the main engine parameters while a custom software (PowerPan ver. 2.1 developed by Powertech Engineering) has allowed the real time control and acquisition of the of in-cylinder pressure, intake manifold pressure, AFR, spark and injection timing and optical data acquisition signals.

Exhaust gas concentrations have been measured through a gas analyzer (AVL Dicom 4000) using the non-dispersive infrared measurement principle for carbon monoxide (CO) and unburned hydrocarbons (HC), and the electrochemical method for nitrogen oxides (NO_x) emissions. Accuracy was within ± 3 % and the resolution of readings for the first component was 0.01% and 1 ppm for the other two species. Soot and particulate have been detected by a spectroscopic technique due to the low sensitivity of the smokemeter and opacimeter with respect to the limited emission of the optical engine in lean combustion conditions.

7.1.2 Optical diagnostics set-up

UV-visible digital imaging has been applied to characterize the flame propagation in the combustion chamber and to evaluate the effects of fuel injection strategies on flame morphology. An intensified CCD (ICCD) camera has ensured a good signal to noise ratio even for flames with reduced luminosity. This has been possible as a consequence of the high quantum efficiency of the intensified detector in the UV spectral range (from 250 nm to 400 nm). Since the exothermic reactions typical of the first stages of the combustion process and of flame front outline are characterized by radiative emission in the UV wavelength range, the ICCD camera is particularly well suited for flame kernel optical investigations.

An ICCD is a CCD equipped with an image intensifier mounted in front of the CCD which allows to enhance the photons collection in the UV wavelengths range.

Even if the ICCD doesn't allow to perform cycle-resolved imaging, it has been preferred to a CMOS camera because of its higher signal to noise ratio allowing to characterize even low luminous intensity flames such as the case of lean combustion.

This is a consequence of the high quantum efficiency of the intensified detector in the UV spectral range (from 250 nm to 400 nm). Since the exothermal reactions typical of the first stages of the combustion process and of flame front outline are characterized by radiative emission in that UV wavelength range, the ICCD camera is particularly well suited for flame kernel optical investigations. Moreover the ICCD flame area resulted larger than CMOS cycle resolved one as shown in figure 7.3.

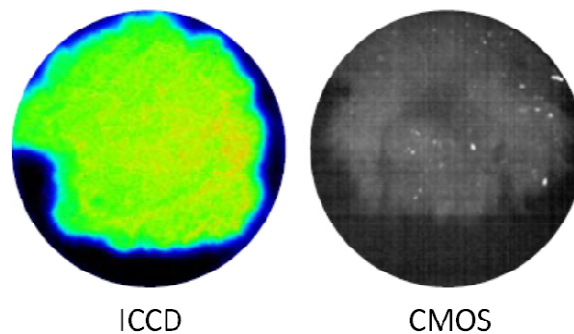


Figure 7.3 - Comparison between ICCD and CMOS acquisition of flame at 22 CAD ASOS with the engine operated at 2000 rpm, WOT, stoichiometric AFR and 15 CAD BTDC spark timing.

During the UV-visible visualization, the focus lens has been directly coupled with the ICCD. No filters have been used, in order to cover the whole range light emission. The intensified camera has been employed in full-chip configuration. A spatial resolution of 94 $\mu\text{m}/\text{pixel}$ has been obtained. The ICCD camera has acquired image both in sequential and repetitive mode. In the first case, one image per cycle has been detected

with a fixed duration ($41.6 \mu\text{s} \sim 0.5 \text{ CAD}$) and increasing the delay ($83.3 \mu\text{s}/\text{cycle} \sim 1.0 \text{ CAD}/\text{cycle}$) from the trigger that has corresponded to spark occurrence. In repetitive acquisition mode one image per cycle has been recorded with a fixed duration ($41.6 \mu\text{s} \sim 0.5 \text{ CAD}$) and fixed delay ($1250 \mu\text{s} \sim 15 \text{ CAD}$) from the trigger.

Spectroscopic measurements based on UV-visible natural emission have been performed to follow the evolution of radiative chemical species involved in the combustion process from the spark ignition until the late combustion phase. During the spectroscopic investigations, the radiative emission from the combustion chamber has been focused by a 78 mm focal length, f/3.8 UV Nikon focus lens onto the 250 μm micrometer controlled entrance slit of a spectrometer with 150 mm focal length and 300 groove/mm grating (central wavelength 350 nm). From the grating, the radiations have been detected by an intensified CCD camera (array size of 1024×1024 pixels with a pixel size of $13 \times 13 \mu\text{m}$, 16-bit pixel digitization and 1 MHz sustained repetition rate).

Spectroscopic investigations have been carried out in the central region of the combustion chamber. The binning of 720 spectra has been considered. The ICCD camera has operated in sequential acquisition mode, thus spectra have been detected with fixed gate width ($41.6 \mu\text{s} \sim 0.5 \text{ CAD}$) but variable delay ($83.3 \mu\text{s}/\text{cycle} \sim 1.0 \text{ CAD}/\text{cycle}$) from the trigger. The emission spectra have been corrected for the wavelength dependent sensitivity of the optical devices. Wavelength calibration has been performed using a Hg lamp.

Spectroscopic data post-processing has allowed to evaluate the time evolution of chemical species featured by the combustion process in all operative conditions. It should be noted that all the detected species through emission spectroscopy are in

excited electronic states; for this reason the notation “*” that identifies the excited species will be omitted.

For each individual-cycle spectrum, OH emission has been evaluated at 309 nm relative to the local background, which has been estimated by linear interpolation between the nearest intensity minima on either side of the band containing the feature of interest. Soot precursors evolution have been assessed at 470 nm considering the tail of blackbody carbon emission.

7.1.3 Image acquisition and post-processing

In order to obtain quantitative information from the combustion visualization, macroscopic parameters related to flame morphology have been evaluated via binarization of each flame image[21-23].

An ad-hoc image processing methodology has been performed for each visualization technique by Vision Assistant 2011 of National Instruments. After the extraction of the intensity plane to obtain 256-grey scale image, a circular mask has been fixed in order to cut the spurious light from reflections at the boundaries of the circular window of the piston crown. Then the contrast and brightness of the images have been adjusted through look-up table (LUT) transformation based on a power function:

$$G(pixel) = pixel^{1/x} \quad (7.1)$$

where $x = 1.5$ has been set. The resulting images have been binarized by automatic thresholding segmenting the image into two classes, particle area (foreground) and background considering the image histogram. Compared to manual thresholding, this methodology does not require setting minimum and maximum image intensities by the user. Despite of the classic Otsu’s method in which the optimal threshold minimizes the

intra-class variance (ICV), in this work the “inter-class variance” (iCV) method has been applied, thus reducing computational times. The iCV method is based on the concept that minimizing intra-class variance is equivalent to maximizing inter-class variance; thus the optimum threshold T_{opt} can be formulated as:

$$T_{opt} = \arg \max \left[P(T) \cdot (1 - P(T)) \cdot (m_f(T) - m_b(T))^2 \right] \quad (7.2)$$

where m_f and m_b are the mean values of the foreground and background, respectively:

$$m_f(T) = \sum_{g=0}^T g \cdot p(g) \quad (7.3)$$

$$m_b(T) = \sum_{g=T+1}^G g \cdot p(g) \quad (7.4)$$

$p(g)$ is the probability mass function (*pmf*) of the image; g (from 0 to G) is the weight of the mean; G is the maximum luminance value in the image (255 for 8-bit image).

The cumulative probability function P is defined as:

$$P(g) = \sum_{i=0}^g p(i) \quad (7.5)$$

The foreground (object) is defined as the set of pixels with luminance values less than T , while the background pixels have luminance value above this threshold.

After thresholding, morphological transformations have been performed to fill enflamed holes and remove small extra-flame objects and FFT low-pass truncate filter (5%) has been applied to binarized image. Then the flame area, Waddel disk and Heywood Circularity Factor have been evaluated [24-25]. Flame area has been estimated as the “projected” in-cylinder enflamed area obtained by summing up the pixels of binarized

images. The Waddel disk diameter is the diameter of a disk with the same area as the foreground. The Heywood Circularity Factor has been the perimeter divided by the circumference of a circle with the same area. The closer the shape of a foreground is to a disk, the closer the Heywood circularity factor is to 1.

7.2 Operative conditions and results

Combustion tests have been conducted in the optically accessible engine through conventional methodologies and optical diagnostics based on UV-visible digital imaging and spectroscopy. The experiments have been performed at two different start of injection settings (SOI): 300 and 260 CAD BTDC. Two relative air-fuel ratios have been set: close to stoichiometric (i.e. $\lambda \sim 1$) and lean (i.e. $\lambda \sim 1.15$) operation. Intake air temperature has been around 300 K and ambient pressure at 1 atm; coolant and lubricant temperature has been maintained at 330 K using a thermal conditioning unit. A fixed value for engine speed has been set at 2000 rpm, chosen as representative for mid-road load automotive use. All cases that have been investigated feature wide open throttle (WOT).

7.2.1 In-cylinder pressure and exhaust emission analysis

Figure 7.4 reports the effect of spark timing and injection phasing on IMEP evaluated as percentage variation from the reference case of SOI 300 CAD BTDC and spark timing (ST) 15 CAD BTDC.

ST 15 CAD BTDC has been estimated as the MBT for delayed injection timing and a small decrease in IMEP was measured when changing the SOI from 300 to 260 CAD BTDC. For this reason, a more detailed analysis of thermodynamic data has been

performed. In particular, two AFR have been considered in order to work in lean-burn and stoichiometric conditions; tests details are reported in Table 7.2.

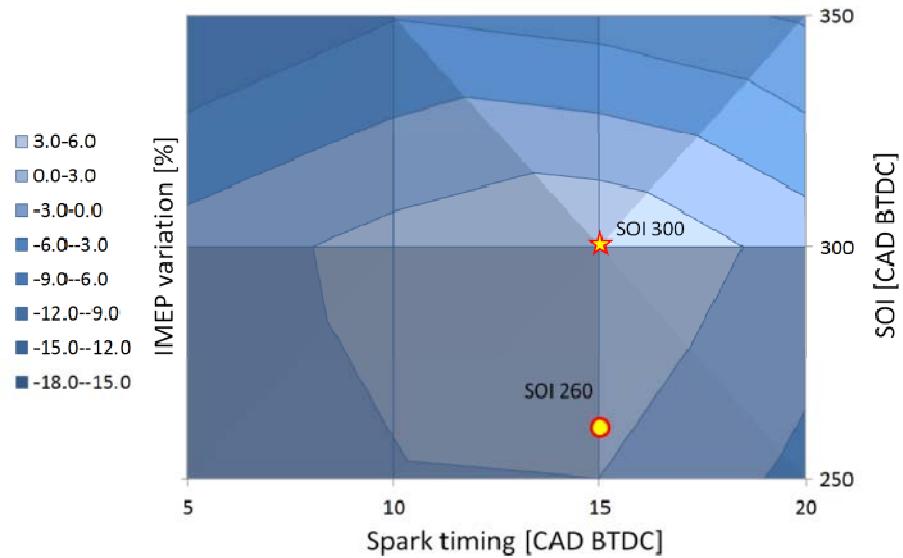


Figure 7.4 - Effect of spark timing and injection phasing on IMEP evaluated as percentage variation from the reference case of SOI 300 CAD BTDC and ST_15CAD BTDC.

Figure 7.5 shows IMEP and peak pressure evaluated as the average of 200 consecutive engine cycle at the test conditions of Table 7.2. The standard deviation for each test is reported in the plot as error bar.

Table 7.2. Test conditions

Test label	DOI [CAD]	$\lambda \pm 1\%$
260_L	33	1.15
300_L	33	1.15
260_ST	38	1.00
300_ST	38	1.00

No significant difference has been found concerning the IMEP by changing the injection timing, while a decrease is evident by increasing the AFR. The peak pressure is a better indicator for evaluating the influence of the injection phasing: an increase in maximum cycle pressure can be noted at the most delayed SOI.

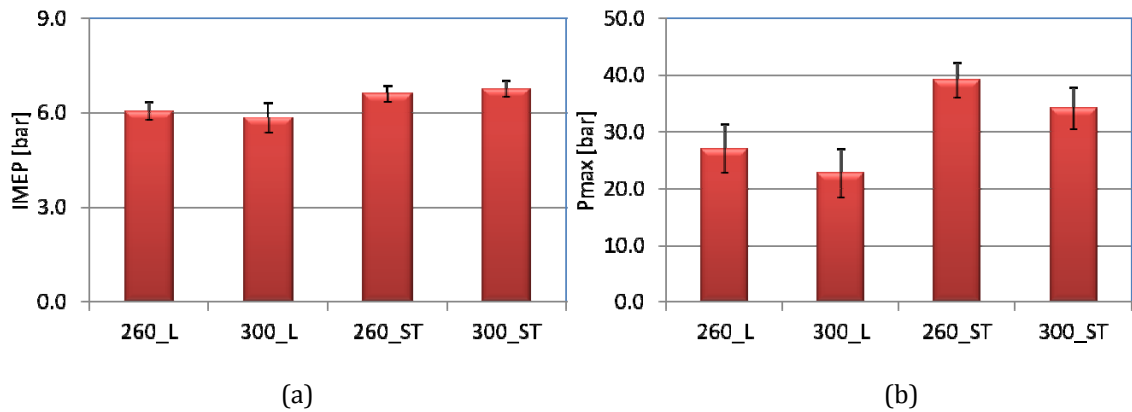


Figure 7.5 - (a) IMEP and (b) peak pressure values evaluated as averaged on 200 consecutive engine cycles for conditions of Table 7.2. Standard deviations related to each test are reported as error bars.

Fuel charge distribution does not significantly affect the HC emissions at the exhaust (Figure 7.6 a) indicating a stable combustion even at higher AFR. A slight HC increase can be observed at late injection timing, indicating a worst air-fuel mixing. Moreover, due to the higher pressure peak, the local temperature increase inducing higher NO_x emissions too, as shown in figure 7.6 b). Finally CO emissions (figure 7-7) are close to zero at all investigated conditions indicating an almost complete combustion even with lean mixture.

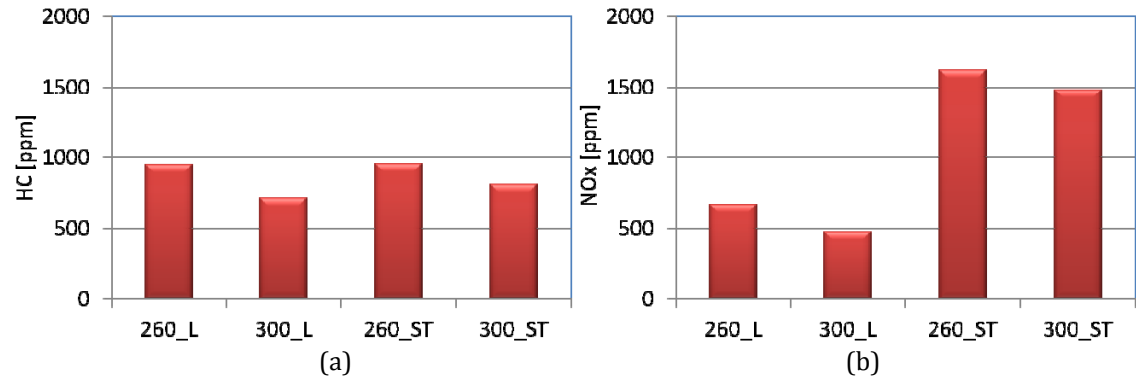


Figure 7.6 - (a) HC and (b) NO_x emissions measured at undiluted exhaust.

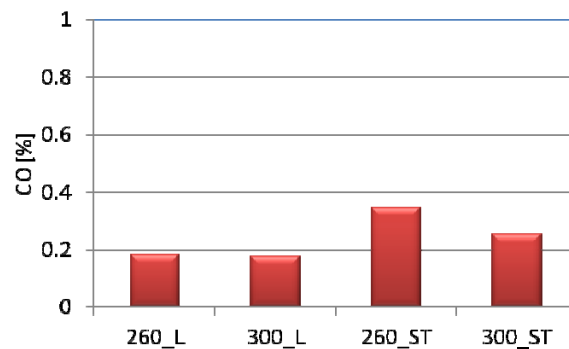


Figure 7.7 - CO emission measured at undiluted exhaust.

A more significant result was observed for the particulate emission (figure 7.8). Exhaust opacity is maximum for the late injection strategy and stoichiometric AFR. This further emphasizes the complex interactions that result in changes of both performance and emissions when changing injection strategies. Taking into account the new stringent regulations related to particulate matter emissions from GDI engines that cannot be reduced by three way catalytic converters (as is the case for HC and NO_x) investigations on carbonaceous structures and soot formation during the combustion process have been performed through UV-visible flame emission spectroscopy.

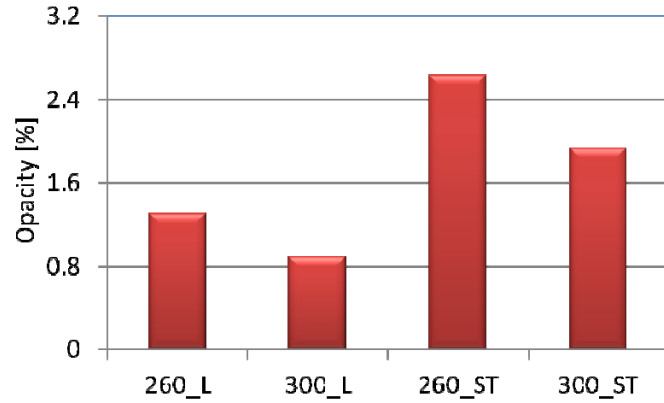


Figure 7.8 Opacity measured at undiluted exhaust.

7.2.2 UV-Visible imaging and spectroscopy

UV-visible visualization has been performed to follow the combustion process from ignition to the complete flame propagation, using for all the fuel injection strategies of Table 7.2. Figure 7.9 presents a selection of images detected at different CADs after start of spark (SOS) fixing the SOI at 300 CAD BTDC. Similar results have been obtained for the delayed injection phasing.

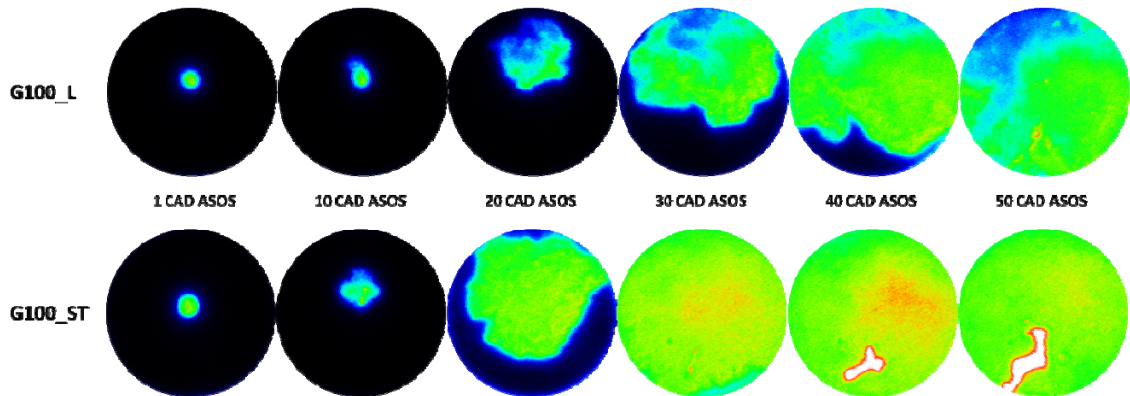


Figure 7.9 - Selection of UV-visible flame emission images detected for lean (top) and stoichiometric condition(down) (SOI_300 CAD BTDC).

For all the selected settings, the flame kernel is resolvable around 5 CAD after the spark discharge, due to the very high luminosity of spark induced plasma. This is basically

characterized by the radiative emissions of oxygen, nitrogen and carbon content species [26-28].

The balance between the different radiative species is related to the local fuel concentrations [29- 30].

As shown in figure 7.10, for the selected fuel injection strategies the most intense emission band is due to the de-excitation of CN through $B^2\Sigma^+ \rightarrow X^2\Sigma^+$ diagonal transitions ($\Delta v = 0$) [31-32]. This is well resolved in the 380–390 nm spectral range with the highest peak at 388 nm. Weak band systems due to the $\Delta v = \pm 1$ transitions around 357 and 420 nm have been difficult to detect due to the overlapping with other bands such as those due to NH and N_2 [33]. Regarding NH radicals, low intensity band system related to $A^3\Pi \rightarrow X^3\Sigma^-$ transition was observed in the spectral range 320- 360 nm [32].

The identification of other nitrogen content species has been more complex due to the instability of the excited states. In the spectra of Figure 7.10, N_2^+ system has been detected through the emission of $B^2\Sigma^+ \rightarrow X^2\Sigma^+$ transitions [33, 34]. This has been featured by weak bands at 391 nm (0,0), 357 nm (1,0) and 428 nm (0,1). De-excitation and recombination of N_2^+ has promoted reactions for N_2 formation [35-37].

N_2 presents weak close bands around 340 and 410 nm that are very hard to distinguish from OH, NH and CN bands [38]. OH has been detected through $A^2\Sigma \rightarrow X^2\Pi$ (0, 0) band (R and P branches around 307 and 309 nm, respectively) [39]. During the spark ignition, OH radicals have been formed by high electronic temperature reactions between H atoms from the fuel and O atoms produced by the discharge [40]. It should be noted that OH band due to $A^2\Sigma \rightarrow X^2\Pi$ (1, 0) and centred at 282 nm is related to high temperature gas conditions and for this reason it is not detectable [41]. Depending

on the operative conditions, OH emission is associated with NO $A^2\Sigma^+ \rightarrow X^2\Pi$ weak bands in the range 240-260 nm, named gamma bands [32, 33, 42]. Excited NO is formed by reactions between nitrogen and oxygen atoms produced by high temperature plasma [43].

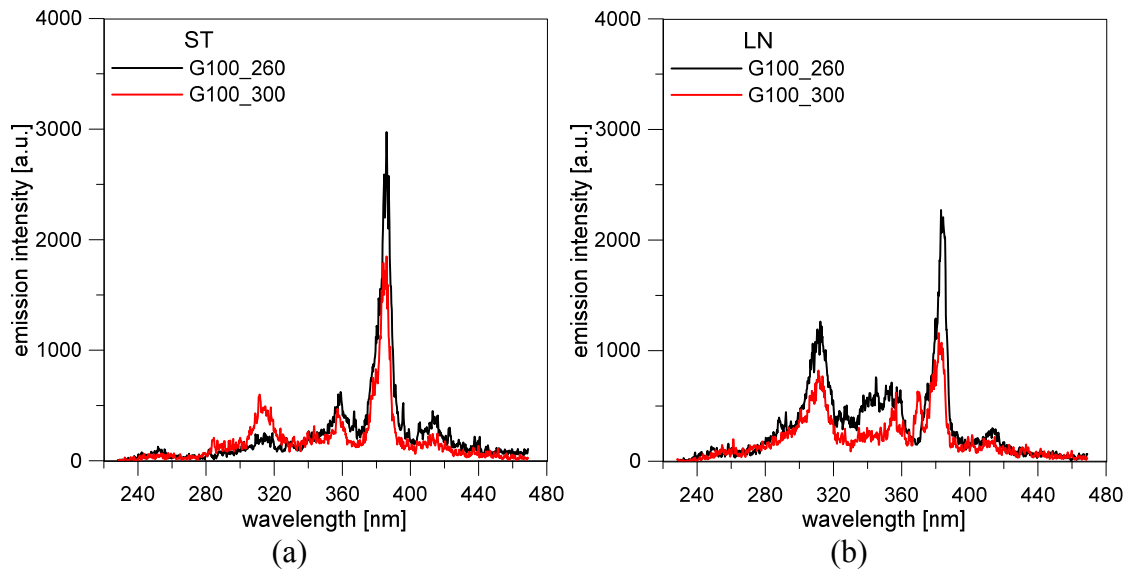


Figure 7.10. UV-visible emission spectra detected at 1 CAD ASOS at different injection timing, in (a) stoichiometric and (b) lean conditions.

As shown in figure 7.9, after the spark, the flame evolves from kernel phase (10 CAD ASOS) towards the combustion chamber walls with a small asymmetry in the flame outline. A distortion from the circular shape is evident for all the conditions around 20 CAD ASOS. The flame evolves with different velocity towards the intake and exhaust valves due to the combined effects of local temperature and air-fuel ratio gradients. Moreover, as shown in Figure 7.11, the enflamed area (normalized to the optical limit) in these early combustion stages results larger for most delayed injection timing, in agreement with in-cylinder pressure results showing higher pressure peak at SOI_260 CAD BTDC. As expected, a decrease in flame speed is detected in lean condition.

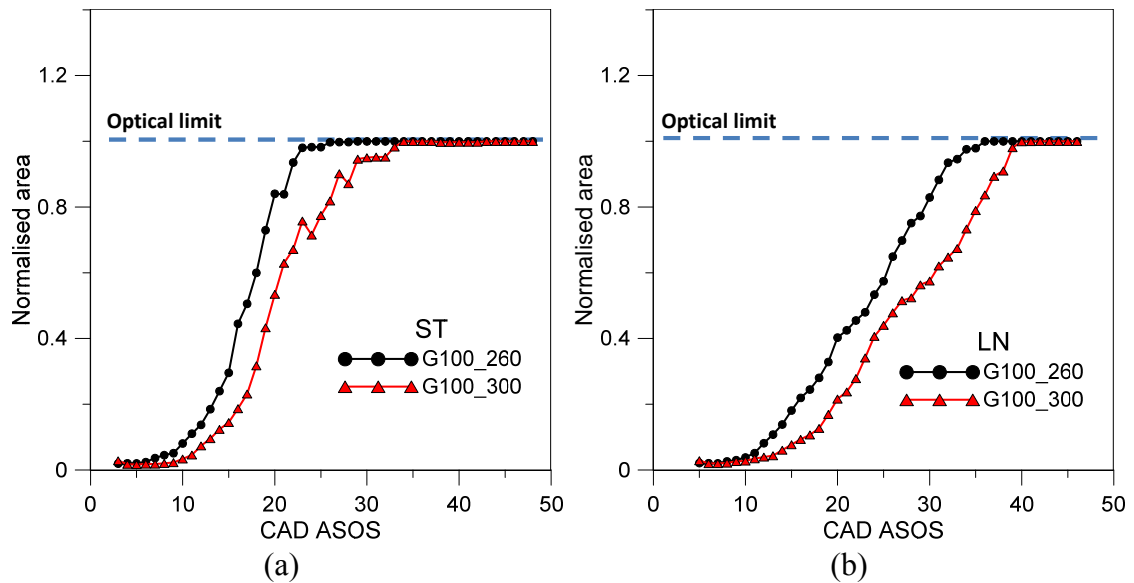


Figure 7.11 - Flame area evolution for different injection timings at (a) stoichiometric and (b) lean conditions.

The outcome of changes in operative conditions on flame shape is quantified through Heywood Factor defined as the ratio between the flame surface perimeter and the perimeter of a circle having the same area; the results are shown in figure 7.12. Even if the distorted flame features higher surface to volume ratios, this does not translate into faster combustion development; the reason for such behaviour is that both distortion (as an overall parameter) as well as the scale of local flame structures play a role in the convective and chemical phenomena that result in a certain reaction rate. For both injection strategies the higher equivalence ratio determined higher Heywood factors. This results seems to be discordant with respect to flame area evolution results. In fact a Heywood factor higher than 1 implies a flame distortion, hence an increase in flame speed is expected since the flame surface/volume ratio grows.

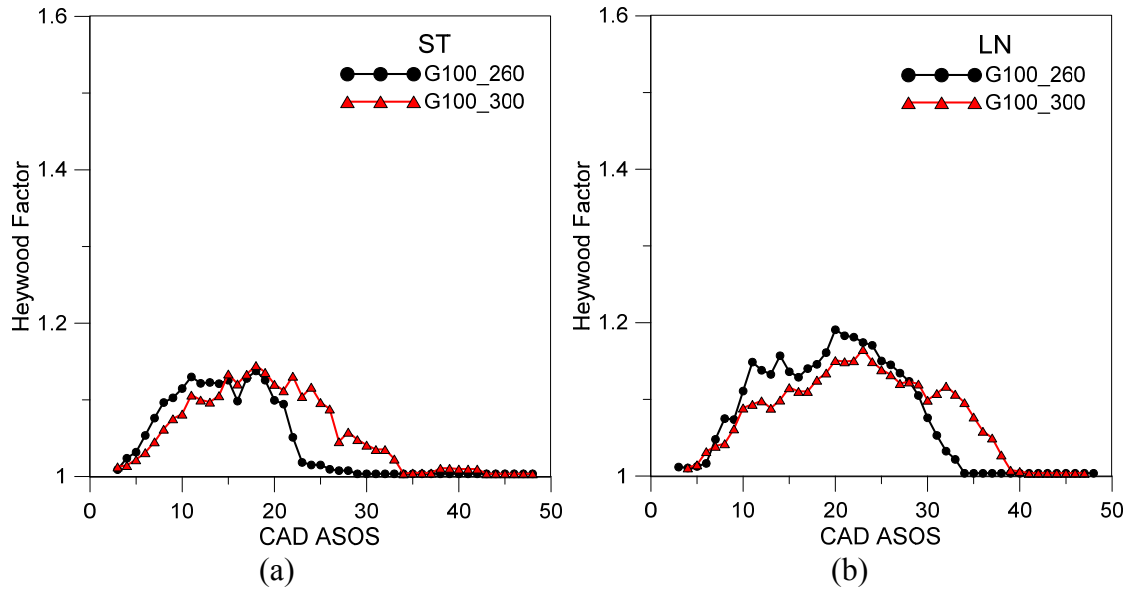


Figure 7.12 - Heywood factor evolution for both injection timings at (a) stoichiometric and (b) lean conditions.

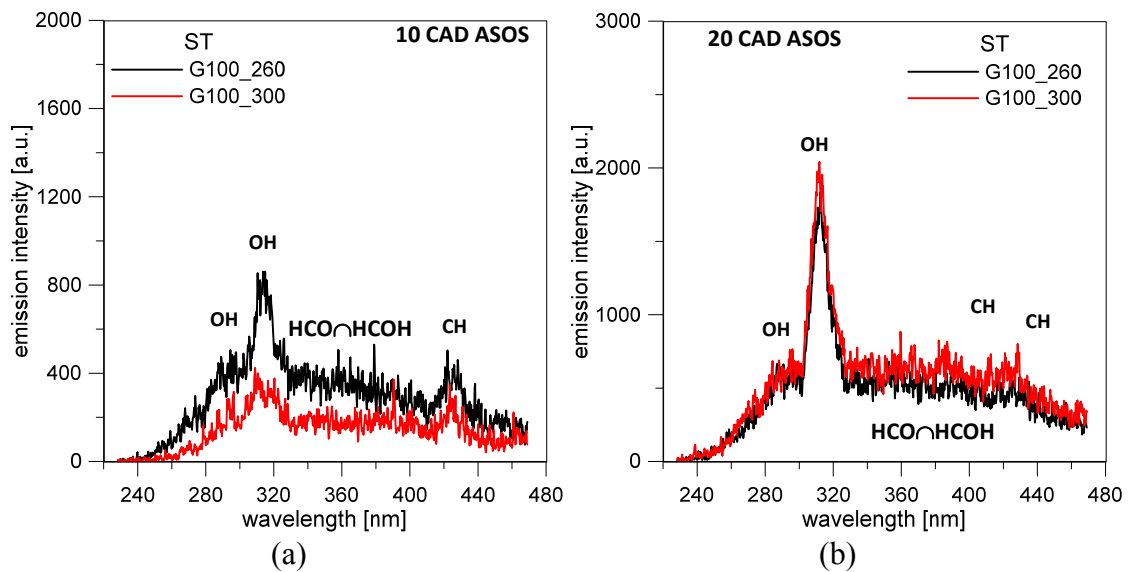


Figure 7.13 - UV-visible emission spectra detected at (a) 10 CAD ASOS and (b) 20 CAD ASOS at different injection timings at stoichiometric conditions.

Concerning the chemical species that featured the phase of combustion process related flame development up to the optical limit, Figures 7.13-7.14 show typical flame emission spectra measured from 10 to 30 CAD ASOS in stoichiometric conditions. As expected, flame kernel detected at 10 CAD ASOS is basically featured by OH and CH

[44]. The result was expected due to role of OH as a key species for the initiation of combustion, being responsible for breaking C–H bonds in hydrocarbon fuels. OH radiative emission at 282 nm due to (1,0) $A^2\Pi \rightarrow X^2\Pi$ transition appears together with the 309 nm band. CH emission consists of three band systems centred at 430 nm, 390 nm and 314 nm. The last one has been merged in high intensity OH band and it has not been resolvable. CH band systems are associated to transition with the same $X^2\Pi$ ground state and different excited states ($A^2\Delta$ for 431 nm, $B^2\Sigma^-$ for 390 nm and $C^2\Sigma^+$ for 314 nm) that correspond to an increasing flame temperature [45, 46]. As a consequence, the 390 nm band is barely detected only at 20 CAD ASOS. Until this phase, OH and CH bands are superimposed on two broad overlapped band systems. The first one is due to formaldehyde $A^1A_2-X^1A_1$ transitions and interests the spectral range from 340 to 520 nm with its highest peak around 390 nm [47, 48]. The second wide band system corresponds to HCO Vaidya system. Even if the system ranges from 250 nm to 410 nm, higher heads occur in the 335-375 nm range [41, 49].

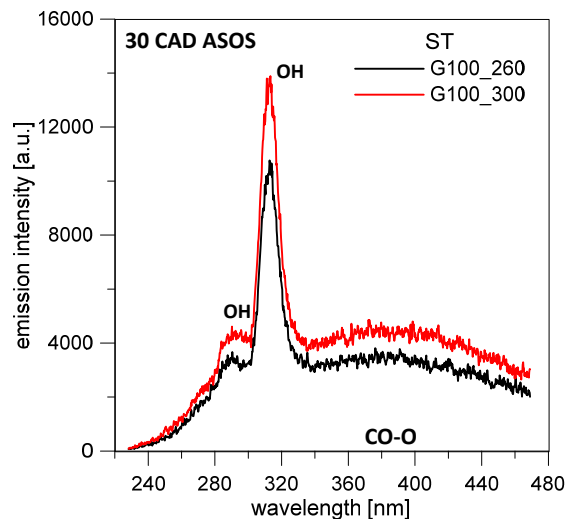


Figure 7.14 - UV-visible emission spectra detected at 30 CAD ASOS at different injection timings for stoichiometric condition.

During the combustion process, CH, HCO and formaldehyde evolve through radiative reactions characterized by HCO and CO intermediate products. These quickly interact with oxygen compounds to form CO₂ and H₂O [50]. At 30 CAD ASOS (Figure 7.14) CO₂ emissions are detected for all the spectra through a chemiluminescence signal extended from approximately 300 nm to 500 nm with a peak around 400 nm [41, 51].

Chemiluminescence is related to CO oxidation [52]:



From 25-30 CAD ASOS, all emission spectra evolve until the late combustion only in intensity without significant changes in the spectral behaviour. However, around 40 CAD ASOS a weak continuous signal, increasing with the wavelength, is observed. This is due to the emission of soot precursors formed during the oxidation of fuel deposits in the combustion chamber [53, 54, 55]. The soot precursors signal is well defined at 50 CAD ASOS as shown in figure 7.15 a. Even if a strong reduction is recorded soot emission is still significant even at 70 CAD ASOS (Figure 7.15 b).

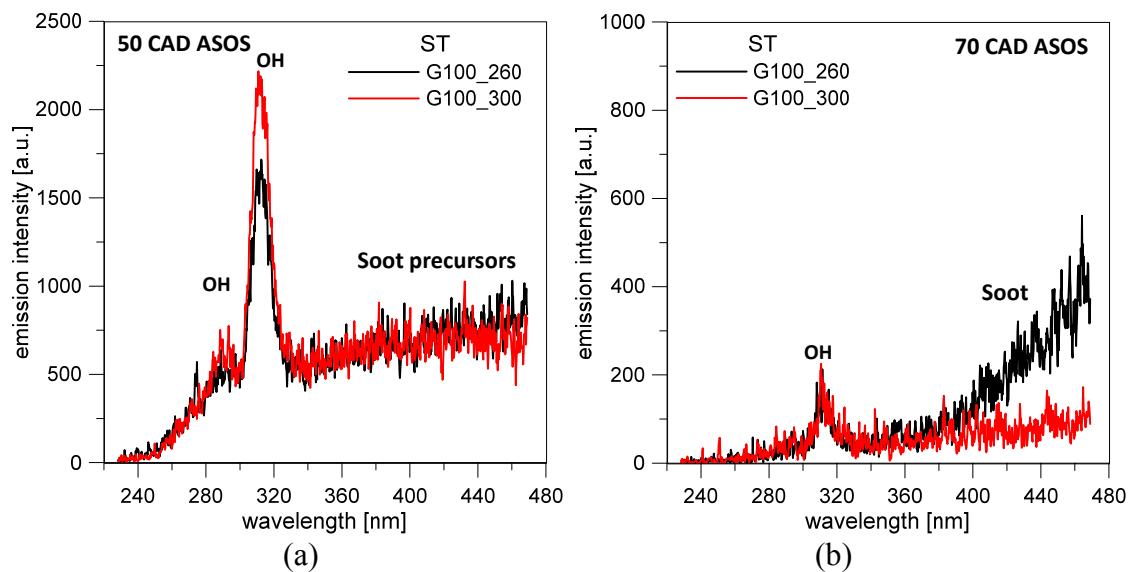


Figure 7.15 - UV-visible emission spectra detected at (a) 50 CAD ASOS and (b) 70 CAD ASOS at different injection timings for stoichiometric condition.

Spectroscopic investigations have allowed to follow soot and OH evolutions in the whole combustion process, through the signal detected in the central region of combustion chamber. Results are reported in Figures 7.16 and 7.17.

The understanding of OH evolution in the combustion process is fundamental due to the complexity of predictive numerical evaluation caused by the double action of this radical in the soot oxidation [56] and NO formation [57-58]. In agreement with in-cylinder pressure and exhaust emission measurements, the most delayed injection strategy induces an increase in OH emission peak, resulting in higher NO_x emissions at the exhaust. Regarding the soot precursor, no significant difference has been found in intensity peak, however a delay in soot oxidation is recorded at SOI₂₆₀ in agreement with higher opacity level at the exhaust. A strong decrease of both OH and soot precursor emission intensity has been observed at the more dilute condition.

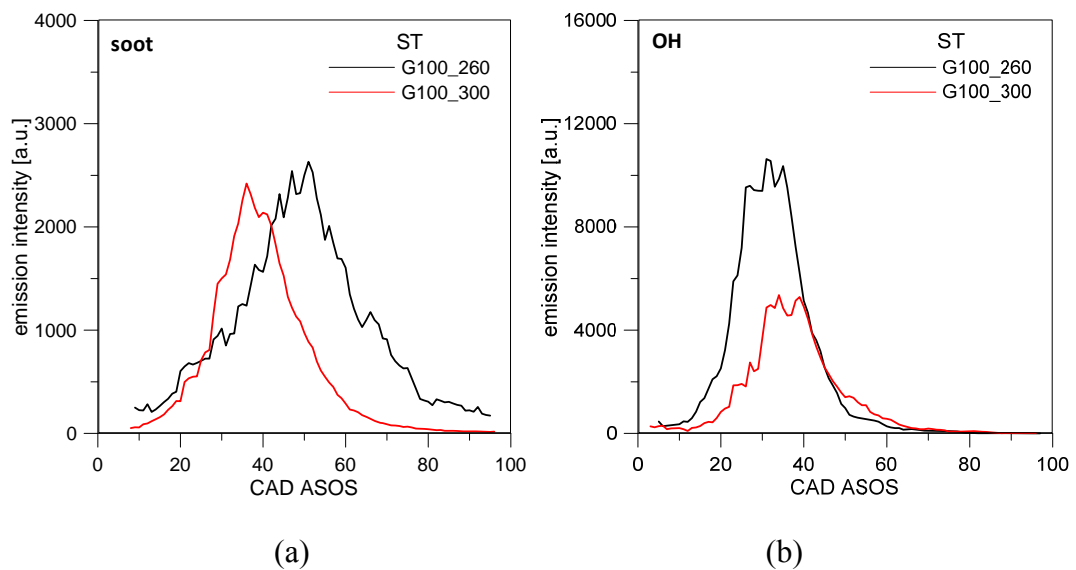


Figure 7.16 - (a) Soot and (b) OH evolutions detected at different injection timings for stoichiometric condition.

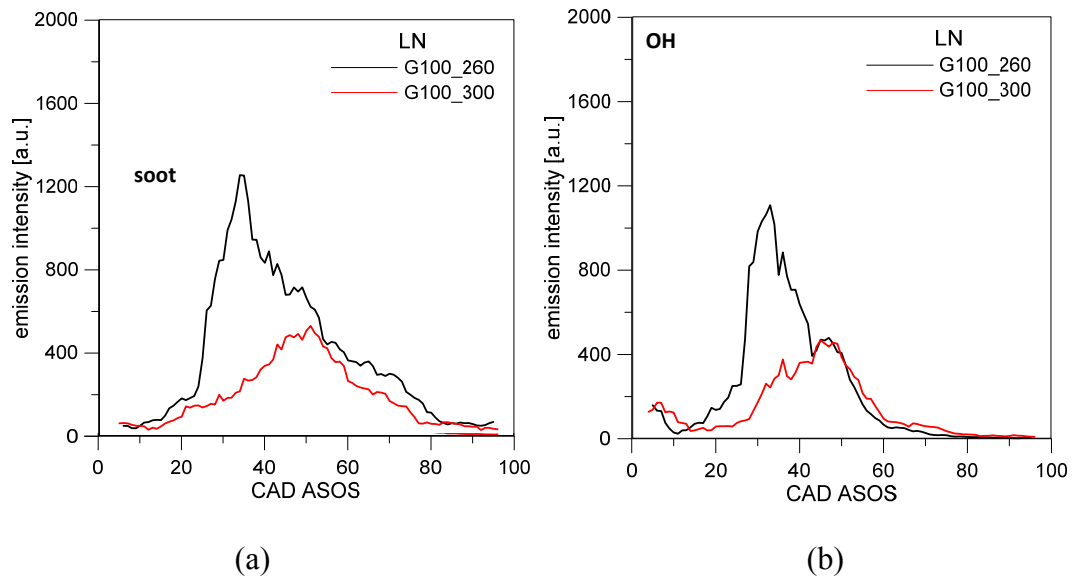


Figure 7.17 - (a) Soot and (b) OH evolutions detected at different injection timings for lean burn condition.

In order to further detail the effects of air-fuel charge on combustion process stability, flame morphology has been analyzed for all selected operative conditions. Specifically, cycle-to-cycle variation of macroscopic parameters have been studied in the early combustion stage.

In figure 7.18, enflamed areas, normalized with respect to the optical limit, have been correlated to peak pressure and 15 CAD ASOS (TDC) pressure for 100 consecutive engine cycles for each operative condition. Greater spreading of data has been observed for lower air-fuel ratio.

To estimate the sensitivity of the flame visualization technique with respect to the thermodynamic analysis in the early combustion stage, data related to the average of 100 consecutive engine cycles are reported in figure 7.19. In particular, macroscopic flame parameters (normalized area and Waddel disk diameter) in figure 7.19 a-b are more sensitive to operative conditions than the pressure signal, showing the same trend of peak pressure (Figure 7.19 c).

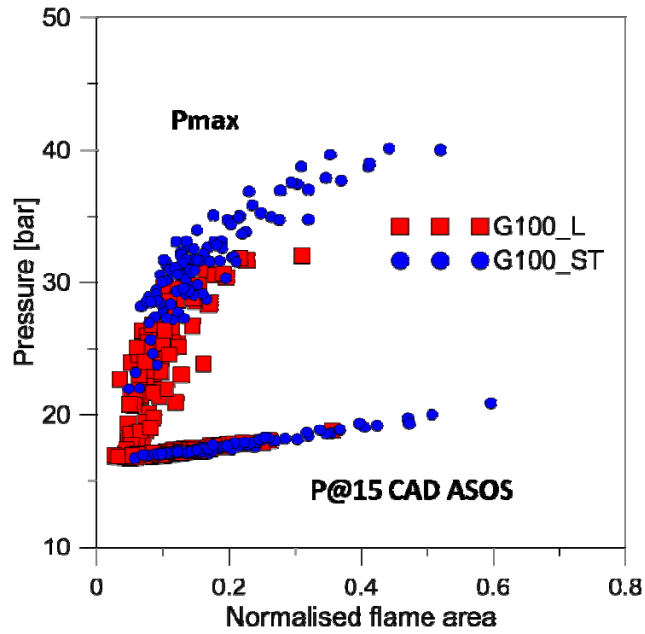


Figure 7.18 - Comparison between normalized area with peak pressure and 15 CAD ASOS (TDC) pressure for 100 consecutive engine cycles at different air-fuel ratios fixing the injection timing at 300 CAD BTDC.

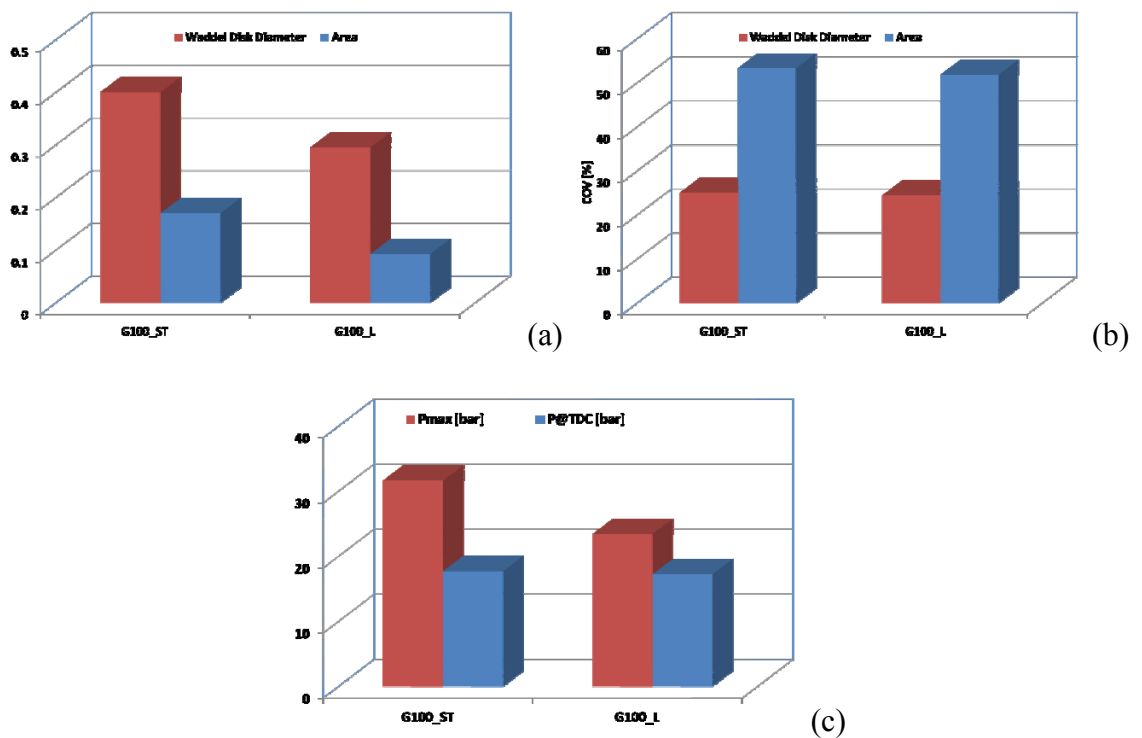


Figure 7.19 - (a) Normalized area, Waddel disk and (b) related COV, (c) peak pressure and pressure @15 CAD ASOS (=TDC). All data are referred to the average of 100 consecutive engine cycles for both air-fuel ratios (SOI_300 CAD BTDC).

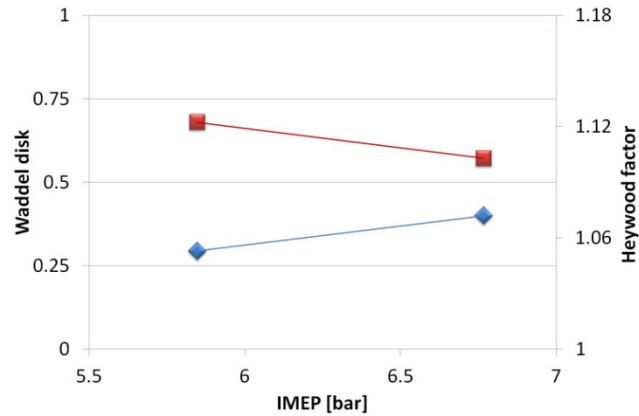


Figure 7.20 - Comparison between normalized Waddel disk @15 CAD ASOS (=TDC) and Heywood Factor versus IMEP. All data are related to the average of 100 consecutive engine cycles for both air-fuel ratios (SOI_300 CAD BTDC).

Pressure measured at the same CAD (approximately at the end of the initial combustion phase) of image acquisition is almost constant. Regarding fuelling effect on flame shape, results in Figure 7.20 show an opposite linear trend of average Heywood factor with IMEP than Waddel disk. This demonstrates that by increasing effective pressure, flame propagates with a more regular shape.

REFERENCES

- [1] Lake, T., Stokes, J., Murphy, R., Osborne, R. et al., "Turbocharging Concepts for Downsized DI Gasoline Engines," SAE Technical Paper 2004-01-0036, 2004, doi:10.4271/2004-01-0036.
- [2] Bandel, W., Fraidl, G., Kapus, P., Sikinger, H. et al., "The Turbocharged GDI Engine: Boosted Synergies for High Fuel Economy Plus Ultra-low Emission," SAE Technical Paper 2006-01-1266, 2006, doi:10.4271/2006-01-1266.
- [3] Jiang, L., Vanier, J., Yilmaz, H., and Stefanopoulou, A., "Parameterization and Simulation for a Turbocharged Spark Ignition Direct Injection Engine with Variable Valve Timing," SAE Technical Paper 2009-01-0680, 2009, doi:10.4271/2009-01-0680.
- [4] Fraser, N., Blaxill, H., Lumsden, G., and Bassett, M., "Challenges for Increased Efficiency through Gasoline Engine Downsizing," *SAE Int. J. Engines* 2(1):991-1008, 2009, doi:10.4271/2009-01-1053.
- [5] Boretti, A., "Use of Variable Valve Actuation to Control the Load in a Direct Injection, Turbocharged, Spark-Ignition Engine," SAE Technical Paper 2010-01-2225, 2010, doi:10.4271/2010-01-2225.
- [6] Kume, T., Iwamoto, Y., Iida, K., Murakami, M. et al., "Combustion Control Technologies for Direct Injection SI Engine," SAE Technical Paper 960600, 1996, doi:10.4271/960600.
- [7] Takagi, Y. (1998). A new era in spark-ignition engines featuring high-pressure direct injection. In Symposium (International) on Combustion, 27(2) 2055-2068.
- [8] Zhao F., Lai M.-C., Harrington D.L. (1999) Automotive spark-ignited direct-injection gasoline engines, *Progress in Energy and Combustion Science*, 25(5), 437-562.

-
- [9] Han, Z., Reitz, R., Yang, J., and Anderson, R., "Effects of Injection Timing on Air-Fuel Mixing in a Direct-Injection Spark-Ignition Engine," SAE Technical Paper 970625, 1997, doi:10.4271/970625.
- [10] Alkidas, A. C. (2007). Combustion advancements in gasoline engines. *Energy Conversion and Management*, 48(11), 2751-2761.
- [11] Piock, W., Hoffmann, G., Berndorfer, A., Salemi, P. et al., "Strategies Towards Meeting Future Particulate Matter Emission Requirements in Homogeneous Gasoline Direct Injection Engines," *SAE Int. J. Engines*4(1):1455-1468, 2011, doi:10.4271/2011-01-1212.
- [12] Jiang, B., Pan, X., Liu, F., Wang, C., & Feng, X. (2013). Experimental Investigation on Fuel Spray Optimization in Gasoline Direct Injection Engine. In *Proceedings of the FISITA 2012 World Automotive Congress* (pp. 45-53). Springer, Berlin - Heidelberg.
- [13] Hentschel, W. (2000). Optical diagnostics for combustion process development of direct-injection gasoline engines. *Proceedings of the combustion institute*,28(1), 1119-1135.
- [14] Drake, M. C., & Haworth, D. C. (2007). Advanced gasoline engine development using optical diagnostics and numerical modeling. *Proceedings of the Combustion Institute*, 31(1), 99-124.
- [15] Sick, V., Drake, M. C., & Fansler, T. D. (2010). High-speed imaging for direct-injection gasoline engine research and development. *Experiments in fluids*,49(4), 937-947.

-
- [16] Kim, S., Yan, Y., Nouri, J. M., & Arcoumanis, C. (2013). Effects of intake flow and coolant temperature on the spatial fuel distribution in a direct-injection gasoline engine by PLIF technique. *Fuel*, 106, 737-748.
- [17] Sick, V. (2014). Optical diagnostics for direct-injection gasoline engine research and development. *Advanced direct injection combustion engine technologies and development*, 1, 260-286.
- [18] Chen, R., Nishida, K., & Kataoka, H. (2014). Characterization of the ignition and combustion processes of spray injected by a hole-type nozzle for a direct-injection spark ignition engine. *Proceedings of the Institution of Mechanical Engineers, Part D: Journal of Automobile Engineering*, 0954407013508279.
- [19] Terzija, N., Karagiannopoulos, S., Begg, S., Wright, P., Ozanyan, K., & McCann, H. (2014). Tomographic imaging of the liquid and vapour fuel distributions in a single-cylinder direct-injection gasoline engine. *International Journal of Engine Research*, 1468087414544178.
- [20] Valentini S. Personal communication
- [21] Russ JC. *The Image Processing Handbook*
Ch7. 3rd Edition, (CRC Press), 1999.
- [22] Parker, J. R. (2010). *Algorithms for image processing and computer vision*. John Wiley & Sons.
- [23] Chen Y.-C. Measurements of flame-front curvature based on Fourier transformation. (2007) *Combustion Theory and Modelling* Vol. 11 (3), 333-349. DOI:10.1080/13647830500348042.
- [24] Klinger T. (2003) *Image Processing with LabVIEW and IMAQ Vision*. Ed Prentice Hall Professional.

-
- [25] Nalluri, V. R., Schirg, P., Gao, X., Viridis, A., Imanidis, G., and Kuentz, M. (2010). Different modes of dynamic image analysis in monitoring of pharmaceutical dry milling process. *International journal of pharmaceutics*, 391(1), 107-114.
- [26] Laux, C. O., Spence, T. G., Kruger, C. H., Zare, R. N. (2003). Optical diagnostics of atmospheric pressure air plasmas. *Plasma Sources Science and Technology*, 12(2), 125.
- [27] Raizer, Y. P., Allen, J. E. (1991). *Gas discharge physics* (Vol. 1). Berlin: Springer-Verlag.
- [28] Griem, H. R. (2005). *Principles of plasma spectroscopy*. Proceedings of the Physical Society, 1.
- [29] Kawahara, N., Tomita, E., Takemoto, S., Ikeda, Y. (2009). Fuel concentration measurement of premixed mixture using spark-induced breakdown spectroscopy. *Spectrochimica Acta Part B: Atomic Spectroscopy*, 64(10), 1085-1092.
- [30] Fansler, T. D., Stojkovic, B., Drake, M. C., Rosalik, M. E. (2002). Local fuel concentration measurements in internal combustion engines using spark-emission spectroscopy. *Applied Physics B*, 75(4-5), 577-590.
- [31] Nicholls, R. W. (1956). The Interpretation of Intensity Distributions in the CN Violet, C₂ Swan, OH Violet and O₂ Schumann-Runge Band Systems by use of their r-Centroids and Franck-Condon Factors. *Proceedings of the Physical Society. Section A*, 69(10), 741.
- [32] Wallace, L. "Band-Head Wavelengths of C₂, CH, CN, CO, NH, NO, O₂, OH, and their Ions." *Astrophysical Journal Supplement*, vol. 7, p.165-172 (1962)
- [33] Luque J. and Crosley D.R., "LIFBASE: Database and spectral simulation (version 1.5)", SRI International Report MP 99-009 (1999)

-
- [34] Nassar, H., Pellerin, S., Musiol, K., Martinie, O., Pellerin, N., & Cormier, J. M. (2004). N₂⁺/N₂ ratio and temperature measurements based on the first negative N₂⁺ and second positive N₂ overlapped molecular emission spectra. *Journal of Physics D: Applied Physics*, 37(14), 1904.
- [35] Klynning L., Pagès P. The band spectrum of N₂⁺. *Phys Scripta*, 25 (1982), pp. 543–560
- [36] Dick K.A., Benesh W., Crosswhite H.M., Tilford S.G., Gottscho R.A., Field R.W. High resolution spectra of bands in the first negative group of ionized molecular nitrogen. *J Molec Spectrosc*, 69 (1978), pp. 95–108
- [37] Flagan R. C. and Appleton J. P. "Excitation mechanisms of the nitrogen first positive and first negative radiation at high temperature", *J. Chem. Phys.*, vol. 56, pp.1163-1173 (1972)
- [38] Zare R.N, Larsson E.O, Berg R.A. Franck-Condon factors for electronic band systems of molecular nitrogen, *Journal of Molecular Spectroscopy*, Vol. 15, Issue 2, pp.117-139 (1965)
- [39] Crosley D.R., Lengel R.K (1975) "Relative transition probabilities and the electronic transition moment in the A-X system of OH" *Journal of Quantitative Spectroscopy and Radiative Transfer*, 15(7–8), 579-591.
- [40] Pilla, G., Galley, D., Lacoste, D. A., Lacas, F., Veynante, D., Laux, C. O. (2006). Stabilization of a turbulent premixed flame using a nanosecond repetitively pulsed plasma. *Plasma Science, IEEE Transactions on*, 34(6), 2471-2477.
- [41] Gaydon, A. G. (1957). *The spectroscopy of flames* (p. 82). London: Chapman and Hall.

-
- [42] Piper, L. G., & Cowles, L. M. (1986). Einstein coefficients and transition moment variation for the NO ($A\ 2\Sigma^+ - X\ 2\Pi$) transition. *The Journal of chemical physics*, 85(5), 2419-2422.
- [43] Kossyi, I. A., Kostinsky, A. Y., Matveyev, A. A., & Silakov, V. P. (1992). Kinetic scheme of the non-equilibrium discharge in nitrogen-oxygen mixtures. *Plasma Sources Science and Technology*, 1(3), 207-220
- [44] Gaydon, A. G. (1957). *The spectroscopy of flames* (p. 82). London: Chapman and Hall.
- [45] Garland, N. L., & Crosley, D. R. (1985). Relative transition probability measurements in the AX and BX systems of CH. *Journal of Quantitative Spectroscopy and Radiative Transfer*, 33(6), 591-595.
- [46] Kojima, J., Ikeda, Y., & Nakajima, T. (2000). Spatially resolved measurement of OH*, CH*, and C2* chemiluminescence in the reaction zone of laminar methane/air premixed flames. In *Symposium (International) on Combustion* (Vol. 28, No. 2, pp. 1757-1764). Elsevier Science.
- [47] Brand, J. C. D. (1956). 184. The electronic spectrum of formaldehyde. *J. Chem. Soc.*, 858-872.
- [48] Peyerimhoff S.D., Buenker R.J., Kammer W.E., Hsu H., Calculation of the electronic spectrum of formaldehyde, *Chemical Physics Letters*, Volume 8, Issue 1, January 1971, Pages 129-135, ISSN 0009-2614, [http://dx.doi.org/10.1016/0009-2614\(71\)80596-1](http://dx.doi.org/10.1016/0009-2614(71)80596-1).
- [49] Fontijn, A. (1966). Mechanism of Chemiluminescence of Atomic-Oxygen—Hydrocarbon Reactions. Formation of the Vaidya Hydrocarbon Flame Band Emitter. *The Journal of Chemical Physics*, 44(4), 1702-1707.

-
- [50] Mclean I.C., Smith D.B. And Taylor S.C. (1994) “The use of carbon monoxide/hydrogen burning velocities to examine the rate of the CO + OH reaction” Twenty-Fifth Symposium (International) on Combustio. Ed. The Combustion Institute, pp. 749-757
- [51] Samaniego J.M., Egolfopoulos F.N., and Bowman C.T., “CO₂* chemiluminescence in premixed flames”, *Combustion Science and Technology*, vol. 109, pp. 183–203, 1995.
- [52] Clyne M.A.A. and Thrush B.A., “Mechanism of chemiluminescent combination reactions involving oxygen atoms”, *Proceedings of the Royal Society of London. Series A, Mathematical and Physical Sciences.*, vol. 269, no. 1338, pp. 404–418, 1962
- [53] Merola, S. S., Marchitto, L., Tornatore, C., Valentino, G., & Irimescu, A. (2013). UV-visible Optical Characterization of the Early Combustion Stage in a DISI Engine Fuelled with Butanol-Gasoline Blend (No. 2013-01-2638). SAE Technical Paper. DOI 10.4271/2013-01-2638
- [54] Hayashida, K., Amagai, K., Satoh, K., Arai, M. (2006). Experimental analysis of soot formation in sooting diffusion flame by using laser-induced emissions. *Journal of engineering for gas turbines and power*, 128(2), 241-246. <http://dx.doi.org/10.1016/j.energy.2013.05.056>.
- [55] Merola S.S., Valentino G., Tornatore C., Marchitto L. In-cylinder spectroscopic measurements of knocking combustion in a SI engine fuelled with butanol–gasoline blend, *Energy*, Volume 62, 1 December 2013, Pages 150-161, ISSN 0360-5442 <http://dx.doi.org/10.1016/j.energy.2013.05.056>.
- [56] Neoh, K. G., Howard, J. B., Sarofim, A. F. (1981). Soot oxidation in flames. In *Particulate Carbon* (pp. 261-282). Springer US.

[57] Pitsch, H., Barths, H., and Peters, N., "Three-Dimensional Modeling of NO_x and Soot Formation in DI-Diesel Engines Using Detailed Chemistry Based on the Interactive Flamelet Approach," SAE Technical Paper 962057, 1996, doi:10.4271/962057

[58] Wüning, J. A., and Wüning J. G., "Flameless oxidation to reduce thermal NO-formation" Progress in energy and combustion science, 23(1), 81-94 (1997).

Conclusion

The present dissertation has investigated the influence of injection parameters on air/fuel mixture and combustion processes in a DISI engine, through advanced diagnostics. It is possible to distinguish three parts of the work: the spray macroscopic parameters characterization, the spray break-up investigation and the study of the effects of injection timing and duration on the combustion process.

In the first stage, the influence of injection pressure and duration on the fuel mass rate and the spray morphology has been analysed. A fuel injection rate meter based on the Bosch Tube principle has provided useful information about the time resolved behaviour of the delivered mass highlighting both transient, such as needle lift and nozzle closing operation, and quasi steady stages of the injection event.

2D Mie-scattering imaging and Particle Image Velocimetry technique have been used for characterizing the liquid spray morphology in terms of tip penetration, cone angle and velocity vector distribution.

Even if the injection parameters affect the overall spray geometry, the characterization of the inner structure of the spray is fundamental for featuring the atomization phenomena which influence the fuel - air interaction. Therefore, Phase Doppler Anemometry (PDA) and Laser Doppler Velocimetry (LDV) have been applied for providing information about the velocity and size of droplets.

Trials have been performed at different injection pressures and distances from the nozzle, along two different axes: the first one corresponding to the jet axis, the second one on the jet edge.

Especially at the higher injection pressure, accurate tests have been possible only at a certain distance from the nozzle, where the spray is more dilute and the laser beam can cross the jet core. For this reason X-ray absorption measurements have been performed in order to investigate high-dense regions of fuel sprays, immediately downstream of the nozzle, providing quantitative measurements of the fuel. X-rays penetrate the dense part of fuel spray because of its weak interaction with the hydrocarbon chain due to their low atomic number. X-ray radiography and tomography have been used to investigate the spray core and reconstruct the 3D inner structure.

The information about the spray development has been used to optimize the injection strategies of an optically accessible DISI engine operating at mid load condition, at a fixed speed of 2000 rpm.

UV-visible imaging has been performed on the engine for investigating the influence of the injection duration and timing on the flame front propagation, while natural emission spectroscopy has been applied to characterize the formation and the evolution of the main compounds featuring the spark ignition and combustion processes. Exhaust emission measurements (Soot, HC, CO and NO_x) have been correlated with pressure related data and optical results.

The air-fuel mixture analysis has allowed to emphasize the effect of the injection pressure on the spray development. First, a higher injection pressure induces an increase in fuel mass rate, allowing to reduce the injection time leaving more time to the fuel for mixing with surrounding air. Even if an effect on the injection delay was expected, no significant difference has been found by switching the injection pressure from 5 to 10 MPa. Spray morphology measurements have highlighted an increase of spray propagation as given by the estimation of the tip penetration length. This behaviour has

been confirmed by Particle Image Velocimetry. The 10 MPa spray provides higher droplets velocity, with a peak of about 115 m/s over the 90 m/s reached at 5 MPa. In the early stage of injection, the spray has been compact and the droplets mean velocity profiles along the jet axis have been characterized by a linear decreasing trend up to the jet edge. At later time, two different spray regions have been distinguished: the first one with a constant slope decreasing trend, in which the droplets break-up has occurred; the second zone characterized by a slight linear increasing trend, due to coalescence phenomena among the droplets, caused by the impact among the first droplets composing the spray that are braked by air and the next ones travelling at higher velocity. The velocity profiles show a rise of the decreasing velocity region length for 10 MPa, indicating a longer break-up region: as expected, the higher injection pressure enhance the interaction between the spray and the air. This result has been confirmed by Phase Doppler anemometry measurements, which have highlighted both a better break-up and larger droplets velocity at the higher injection pressure. Axial velocities on the jet axis have reached the highest value of 105 m/s at 5 mm from the nozzle and 10 MPa of injection pressure. Looking at droplets size, no significant difference has been found in the jet core region: lower droplets diameter has been detected at 10 MPa in comparison with 5MPa injection pressure, the measurements have provided values in the range between 7.5 and 9 μm .

X-ray tomography measurements have been preformed for investigating the air-fuel interaction in the region immediately downstream the nozzle. The fuel density has shown a peak at the nozzle exit and a quick reduction along the spray propagation. Typical Gaussian-shape distributions of the intensities have been found on the jet cross sections, revealing regions of the jet more dense in the core with respect to the

boundary. Slight asymmetries along the longitudinal direction indicated an interaction between the jet plumes downstream. A little bit higher density has been recorded at 10 MPa. Moreover the density seemed to decay with a slight slower trend. Probably, the size of the region of interest was not large enough to completely highlight the injection pressure effect on the fuel mass distribution.

The results of spray development measurements have clearly demonstrated the advantages of increasing the injection pressure to improve the spray break-up. For this reason, all the injection strategies for combustion process investigation have been set at 10 MPa, while the effect of Air-to-Fuel ratio and injection timing has been analysed. The tests have been performed in the optically accessible DISI engine, through high resolution UV-visible flame imaging and natural emission spectroscopy. For all the settings, the optical data have been correlated with those obtained through thermodynamic analysis and exhaust emission measurements. IMEP decrease has been recorded by increasing the AFR while no significant difference has been found changing the injection timing. The peak pressure is resulted a better indicator for evaluating the influence of the injection phasing, emphasizing an increase in maximum cycle pressure at the most delayed injection timing. Looking at the exhaust emissions, slight higher HC values have been recorded at late injection timing, indicating a worst air-fuel mixing. An increase in NO_x emissions has been found at lower AFR strategies: due to the higher pressure peak, the local temperature increases inducing higher NO_x emissions. Looking at the soot formation, exhaust opacity has achieved a maximum for the late injection strategy and stoichiometric AFR. This result is in agreement with larger flame propagation speed found through the UV-Visible imaging. In particular, the maximum speed has been recorded at the most delayed injection time in stoichiometric

condition. UV-visible spectroscopy has allowed to deep investigate the pollutant formation in the combustion chamber. Particularly, OH and soot precursor signal have been analysed and related to the NO_x and soot exhaust emissions, respectively. In agreement with in-cylinder pressure and exhaust emission measurements, the most delayed injection strategy induced an increase in OH emission peak, resulting in higher NO_x emissions at the exhaust. Regarding the soot precursor, no significant difference has been found in intensity peak, however a delay in soot oxidation is recorded at the most delayed injection time in agreement with higher opacity level at the exhaust. A strong decrease of both OH and soot precursor emission intensity has been observed at the more dilute condition.

Acknowledgment

I'd like to thank all those who have supported me and have contributed to the accomplishment of this dissertation. First of all, I would like to thank Prof. Fabio Bozza; it has been an honour for me to have him as supervisor. Special thanks are due to Dr. Luigi Allocca and Eng. Gerardo Valentino who first introduced me to the Engine research.

I'm grateful to Dr. Merola for having "turned on the light" when it was necessary: I'd like to thank her for both technical suggestion and her energy, without which this work would not be possible.

Thanks to Cinzia who knows as to be close even at ten thousands kilometers distance.

I'd like to thank Sultan, Dariush and all XLab-Frascati group, because it is quite difficult find excellent researcher as they are but it is much more difficult find true friends.

Thanks to Salvatore for his sincere friendships and his precious teachings.

Special thanks go to Alfredo Mazzei for both his support in the experimental set-up preparation and his special coffees.

I'd like to thank all my colleagues, particularly Stefano Iannuzzi, Adrian Irimescu and Stefano Valentini, Ugo, Francesco and Gabriele for the infinite discussion at the end of the day.

Finally I thank my family who always supports and stands me, and Elvira, who is so crazy to decide sharing her life with me.